ELECTRON FIELD EMISSION FROM BORON NITRIDE THIN FILMS

by

Pedro Arón Encarnación

A dissertation submitted in partial fulfillment
of the requirements for the degree of
Doctor of Philosophy
(Physics)
in The University of Michigan
2008

Doctoral Committee:

Professor Roy Clarke, Chair
Professor David W. Gidley
Professor Brian E. Gilchrist
Professor Bradford G. Orr
Associate Professor Çağlıyan Kurdak

Para Kirsten, Diego, Giovanni, y Benito
son mi corazón
sin el cual no puedo vivir

ACKNOWLEDGEMENTS

We live in a time and place where individual achievement and accomplishment are highly valued and singularly praised. The mere existence of the body of work which this dissertation represents is an enduring testament to the fact that, in a very real sense, there is no such thing. For what is most often celebrated as individual achievement is typically the end result of a long string of contributions by a whole host of partners - some unwillingly, most unwittingly. Without any one of them, these words would not exist.

I'll probably never know by name all of those who gave of themselves, to bring to fruition the completion of this work. I'll never be able to repay them all. I will do my best, however, to acknowledge here and in writing as many of them as I can.

First, I'd like to recognize my research advisor, Professor Roy Clarke, as the model of encouragement, unflappable support, and commitment to his students that any dissertation advisor would do well to emulate. I have been privileged to both benefit and learn from his devotion to the advancement of both those he works with as well as those who work for him. For all he has done over so many years to promote my success, I am forever grateful.

Thanks to Professors Gidley and Kurdak for persevering in support of the completion of my degree. Professor Gilchrist's collaborative support in our research was essential in making it all possible. I'm particularly grateful to Professor Orr, for stepping in and stepping up on such short notice in my dissertation defense. I am obliged to my entire dissertation committee for all of the constructive criticism, expertise, and personal encouragement they willingly shared with me.

For the personal and professional support from department professionals such as Cynthia D'Agostino and Charles Sutton, Kimberly Smith, Helmut Schick, John Vidolich, Ramón Torres-Isea, and Duane Lute, without whom I would never have made it, many thanks are due.

For the essential camaraderie, companionship, and solidarity of a plethora of fellow graduate students, such as Jevne Micheau-Cunningham, Mitaire Ojaruega, Leith Dwyer-Allen, Katherine Herrick, and Adrian Cavalieri, Richard Vallery, Delia Cabrera Fernández, Greg DeMaggio, Bita Ghaffari, Terry Dull, among many others, I am forever beholden.

A particular debt of gratitude is owed to the unique opportunity and support I was privileged to receive from my current employer, The Aerospace Corporation, without which I would not have been able to finish. Special thanks to Dr. Wanda Austin, Dr. Manuel De Ponte, Karolyn Young, Bernard Chau, Thomas Darone, Dr. John Stacy, Lisi Jackson, David Meshel, and everyone else there for all they

contributed to making this happen.

The list of those brothers and sisters at Knox Presbyterian Church in Ann Arbor and Reston Presbyterian Church in Virginia who touched the life of my family throughout my long career as a graduate student is extensive: Mike and Tama Frison; Craig and Gail Swenson; Jim Woolliscroft; Larry and Julie McCammon; Jim and Jean Willoughby; Chuck and Julie Wolf; Phil and Kristin Wong; Steve and Mary Wiland; Rachel Golin; Rachel and Steve Wampler; Peggy, Kyle, and Kimberly Ryder; Dan Tjarks; Rick, Wendy, Mark, and Carey Wallace; Karl Schmidt; Steve and Diane Telian; Fred and Gwyneth Bailey; Bob and Eileen Lynn; Kent and Jennifer Donovan; Maclovio James Lopez; Kent and Claire Pruss; Tom and Laura Crane; Doug and Jill Barnhart; Issa and Susie Isaac; Dave Kirkpatrick; Sean Kelly; Jeff and Lisa Liou; Tim and Julie Kanzelmeyer; Tony and Nikki Martell; Jonathan and Barb Martin; Rob Prater; Becky Ridenour; James and Barbora Paternoster; Cedric Lundy; Ray, Sharon, Justin, Jaleah, and Kara McDowell; Brad and Marnie Segura; Jim, Chris, Anna, and Jeff Smith; Rich and Julie Straight; Bill and Julie Schwind; Jack and Lisa Peterson; Flo Allen; Kathy Griess; Jennifer Jensen; Tom, Julie, Sarah, Allyson, and Nathan Dages; Randy and Suna Mattson; Eddy, Evelyn, Christina, and Jonathan Wudijono; Steve and Rita Ranier; Stu and Ruth Ann Irwin; Todd and Teri Peckarsky; Gary and Melda Boyd; Betty and Steve Rockwell; . There are a host of others who are not named here, but to whom I am no less indebted. Everyone here provided either material, emotional, and or spiritual support during the leanest of the years. We would not have made it through without it. Their willingness share our burdens with us is a testimony to the transformative power of The Good News of The Reign of God.

To Don and Gail Harris, who drove eight hours in one day to tow us back home from exit 3 of the Pennsylvania turnpike when our car blew up - thank you for being Jesus to us that day in that way. It kept us all going. It will never be forgotten.

So much gratitude goes to Michael Kobold, a fellow graduate student and lifelong friend who has traveled with me along this road since we set out on it together, and has provided incalculable intellectual support and motivation throughout, but particularly at the very end. I look forward to our continued friendship and mutual support.

To all of my long-suffering family members: James and Betty; Heather and Giovanni; D'Anne and Andy; Jaime and Don; Metha and Adylene; Gaudiosa, Ted, Priscilla, and April Nelle; Mami y Papi; Brenda, Erik and Jazzy; Ruthie, Jason, Michael, and Eva; Titi Tabita; Wil, Mel, Matthew, Mark and Luke; Taña and Phil. I owe so much of who I am and what I could bring to this pursuit to all of you.

As is usual, the best is left for last. The best are my wife and children, who have truly suffered long with me, providing me the love and encouragement I needed all along. It is you who make this all worthwhile.

"Ahora, hijo móo, a más de esto, sé amonestado. No hay fin de hacer muchos libros; y el mucho estudio es fatiga de la carne." - Ecl. xii.12

"Jehová es mi fortaleza y mi cántico, y ha sido mi salvación. Este es mi Dios, y lo alabaré; Dios de mi padre, y lo enalteceré." - Exo. xv.2

TABLE OF CONTENTS

LIST OF TABLES

Table

LIST OF FIGURES

Figure

CHAPTER I

INTRODUCTION

Electron field emission has become a subject of considerable research activity in recent years, fueled in part by the ever-continuing improvements in a wide variety of applications, such as microwave amplifiers, electron microscopes, flash x-ray photography, flat panel plasma displays, and ion propulsion drives, among others, all of which rely on electron sources for their operation. Where in the past, traditional sources of electrons typically based on the mechanism of thermionic emission were satisfactory for many applications, miniaturization and the need for higher energy resolution renders this option for electron supply inadequate. The pressure to reduce power consumption as well as operating temperature, which are often demands accompanying the reduction in device size, bolsters the attractiveness of field emission over thermionic emission as a mechanism for electron supply.

1.1 Historical Perspective

Paradoxically, this interest in field emitters and vacuum microelectronics has additionally been stimulated by the development of solid-state technologies. Strong semiconductor markets have supported the development of technologies that can be

applied to field emitters and vacuum devices, and have created demands for other components, such as displays, that are difficult to make from silicon. Field emission refers to the quantum mechanical tunneling phenomenon in which electrons escape from a solid surface into a vacuum. In contrast to the commonly used thermionic emission from hot filaments, field emission occurs at room temperature from unheated "cold" cathodes under the influence of an electric field. Field emission offers several attractive characteristics, including instantaneous response to field variation, resistance to temperature fluctuation and radiation, and a nonlinear, exponential current-voltage relationship in which a small change in voltage can induce a large change of emission current. Typically, field emission requires a very large electric field, more than 10 V/μm to obtain a reasonable current. A traditional way to obtain this high field was to use a very sharp needle, the tip curvature of which was on the order of a few hundred nanometers, achieved by the wet etching of the emitter. Even so, high voltages on the order of a few thousand volts were necessary to draw a meaningful current. The development of micro- and nano-fabrication technology has changed the situation dramatically. It has allowed for the fabrication of an electrode in very close vicinity of an emitting cathode (*e.g.*, a few micrometers), significantly lowering the operating voltage. In recent years, researchers have increasingly been turning their attentions to the search for materials that will serve as better field emitter cathodes, motivated mainly by a desire for improved emission characteristics (*i.e.*, lower emission field), increased robustness, and increasing amenability to modern manufacturing needs and demands. Diamond and carbon nanotubes have

attracted the most interest lately. The ability to deposit diamond in thin film form at low pressures by chemical vapor deposition and its demonstrated low emission threshold fields of 3-40 V/μm for current densities of around 10 mA/cm^2 continue to fuel this interest [11, 12]. Likewise, *quasi*-one-dimensional carbon nanotubes, which are nanometers in diameter (1-30nm) and micrometers in length (1-20 μm), are also low-field emitters [13]. Emission currents as high as 1 μA from single nanotubes and current densities as high as 4 A/cm^2 from multiple nanotubes have been observed [14, 15]. Both of these materials show promise for certain applications, but their basis in carbon and consequent susceptibility to oxidation renders them unusable for applications such as ion propulsion [16].

Boron nitride (BN) is a wide band gap material with physical properties analogous to those of diamond in its cubic phase (cBN), and similarly analogous to graphite in its hexagonal phase (hBN). BN can also form nanostructures, analogous to carbon nanostructures, such as nanotubes and nano-cones [17, 18]. Unlike diamond, it can be produced in semiconducting form when doped with impurities such as Si, Be, and Mg. Both n-type and p-type materials have been demonstrated in the bulk phase [19, 20]. Additionally, unlike its carbon-based analog, boron nitride is chemically inert, highly insulating in its intrinsic (undoped) form, and stable up to high temperatures.

BN has a high thermal conductivity, dielectric breakdown strength, and exhibits one of the largest band gaps of the III-V Nitrides (see Table 1.1). These properties make it an attractive material for use in high power and/or high temperature electronic and optical devices. The physical similarities in band gap type (indirect), resis-

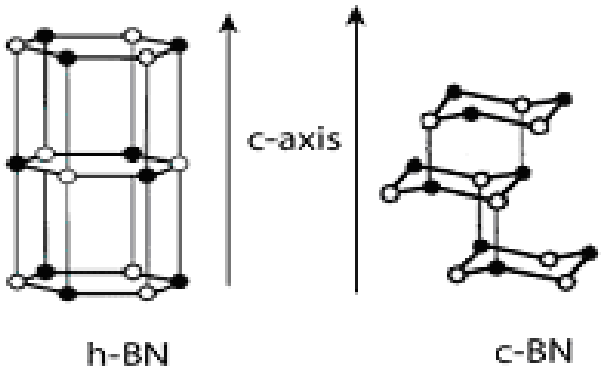

Figure 1.1: Crystal structure of hexagonal and cubic boron nitride.

tivity, and density between BN and its carbon-based crystal analogs further encourage the exploration of the potential of boron nitride thin films as, among other things, a field emitter. BN thin-film research may also benefit a broader set of applications including radiation detectors of thermal neutrons and high-temperature/high-power sensors and even switching, control, and power conversion circuits.

	Band Gap eV	Breakdown Field ($\times 10^9$ V/m)	Dielectric Constant ϵ_o	Hardness $Mohs$	Resistivity $\rho(\Omega$-cm)
Diamond	5.5	2.0	5.5	10	$\sim 10^{17}$
cBN	6.4	1.0	7.1	9.5	$\sim 10^{16}$

Table 1.1: Comparison of selected properties of diamond and cubic boron nitride. Values have been obtained from review articles [1, 2, 3, 4] and Landolt-Bornstein [5]

1.2 Motivation

There are several space-based applications that could greatly benefit or be enabled from an electron emitter technology that offers the advantages of low-power consumption, no consumable requirements, robustness, and high reliability. Charge control is a problem that actually affects all systems in space. Relevant space applications of interest include electrodynamic (ED) tether propulsion, electric propulsion (EP), and spacecraft charge control. As alluded to earlier, field electron emission is also of particular interest to the specific application of ion propulsion of space vehicles and systems. Due to the higher mobility of electrons versus ions, together with unique design and environmental factors associated with space-based systems, spacecraft have a tendency to accumulate negative charge in a plasma environment. The collection of negative charge lowers the ground reference, which can damage on-board electronics and degrade sensor measurement and functionality. In order to prevent charge buildup, electrons must be emitted back into the local plasma - an application for which field emitters are ideal.

Current electron emission technologies include thermionic emitters or plasma contactors. Thermionic emitters require high power to energize electrons from the surface. Plasma contactors require a consumable gas source to charge and emit from the spacecraft. Cold-cathode electron field emission is an appealing alternative since it is low power and does not require a consumable. Examples of this technology include Spindt-type cathodes with gated micron scale molybdenum tips [21] and gated carbon nanotube structures [22]. In cold-cathode emitters, emission is effected via

the quantum mechanical tunneling of electrons, instigated by a bias voltage applied between the anode and the emitting surface, generating a strong electric field at the emitter surface. Field strengths are enhanced via the geometry of the emitting surface, allowing emission at lower overall anode-to-surface voltages. The need for such fine structures, however, increases the environmental susceptibility of most cold cathode technologies. Spindt-type cathodes with Mo tips are known to degrade in an oxygen environment [23], an environment typical for some ion propulsion applications.

In space applications, field emitter arrays (FEAs), arrays of electron emitter tips designed to exploit field enhancement in field emission, will generally need to:

(a) emit on the order of 0.001 - 0.1 A/cm^2

(b) operate in the 10^{-5} to 10^{-6} torr pressure range (and be resilient to exposure to 10^{-3} torr pressures from spacecraft out-gassing and thruster firings)

(c) require bias potentials of 50 - 100 V or less, and

(d) have sufficient life for multi-year space operations.

More recent investigations suggest that each of these requirements can be achieved [24]. What remains is to bring together the specific set of FEA or other cold-cathode material and fabrication technologies to validate and qualify the technology for operation in the space environment, then develop specific subsystems for particular applications.

The space environment is much more benign than many applications proposed for FEA cathode operation, e.g., the RF tube environment where the requisite high current densities necessitate high extraction grid potentials, such that the emitters are driven hard in a hostile, energetic environment of back-streaming ions. However, this is not to suggest that space provides a perfect platform for FEA operation. Ambient pressures as high as 5 x 10^{-7} torr, which are above ultra-high vacuum (UHV) pressure, are found at the lowest altitudes of interest. Atomic oxygen is a major constituent of the ionosphere from 200 km to 500 km altitudes [25] and can be highly reactive with exposed spacecraft surfaces. The FEA may also have to deal with xenon ions, the products of hydrazine and other thruster fuels, as well as various effluents that outgas from a spacecraft, which are capable of briefly raising the local pressure to as high as 10^{-5} torr. In geosynchronous and polar orbits total dose radiation effects must also be considered, although the inherent advantage of field emission arrays with respect to radiation susceptibility is well established, for example in applications such as RF amplifiers and oscillators. These devices are based on the motion of electrons in vacuum, and are consequently capable of a higher fidelity frequency response than solid state devices in which the electron drift velocity is slower. In addition to higher speed, vacuum microelectronic devices are capable of being significantly more radiation hard, because as a response medium for electrons the vacuum is not susceptible to the effects on intrinsic carriers of the interaction of radiation with solid state matter.

It is in such environments that field emitters will be required to operate in a

highly reliable, stable, and repeatable manner for up to the length of the satellite's useful life, which can be as long as 5 - 10 years. In some applications the field emitter cathode will be turned off and subsequently restarted many times over, and each time it must start up in repeatable manner. This field emitter material must also survive the ground based testing of its host spacecraft without operational degradation, which includes shock and vibration loading, thermal vacuum testing (in chambers not particularly clean for semiconductor devices), and radio frequency interference. It must of course survive integration and launch. Field emitter technology can play a crucial role in meeting the operational requirements of the space environment.

1.3 Outline of Dissertation

This dissertation presents the results of a systematic study of the electron field emission of boron nitride thin films. The research presented in this work establishes nanostructured thin film Boron Nitride (BN) as a robust and chemically inert material with a low work function capable of sustainable electron emission in a space plasma environment. Chapter II provides the details of the preparation of samples studied in these experiments. The samples under study have been synthesized using the reduced-bias ion-assisted sputtering technique, which enables the growth of 100% cubic phase up to 2μm in thickness [26]. For thin film deposition, a custom designed UHV chamber, with an *in-situ* reflection high-energy electron diffraction system (RHEED), is utilized for analysis of the structure of the film surface without removal of the film from the growth environment.

Chapter III describes the morphological characterization of the BN films under

study here. RHEED has been used to characterize the surface morphology of the deposited films, providing such information as the orientation of the crystal, or of a selected grain of a mosaic crystal, the crystal structure and the morphology of the sample surface. *Ex-situ*, Fourier Transform Infrared Spectroscopy (FTIR), implemented in transmission mode, provided volumetric phase and composition information of the boron nitride films, with the high intensity peaks of the FTIR spectra identifying either the *cubic* BN zone center TO phonon absorption, typical of the tetrahedral sp^3 bonding of the cubic zinc-blende structure, or the corresponding E_{1u} and A_{2u} TO phonon absorption characteristic of the sp^2 bonding of the hexagonal phase of BN, being observed. A Nicolet Magna 550 Series II spectrometer was employed in the acquisition of the FTIR data. Atomic Force Microscopy (AFM) data of the BN thin films were also obtained outside the growth environment. The AFM data obtained on the *c*BN samples studied revealed a nanotextured surface morphology which characterizes the *c*BN films grown using the previously described reduced-bias sputtering technique. The identified aspect ratio characteristic of these surface nanostructured asperities reveal a self-assembling surface morphology which naturally lends itself to the field enhancement desireable for field emission applications.

After the material and morphological characterization of the samples, they were subjected to a series of systematic electron field emission measurements, the details of which are laid out in Chapter IV. First, the development of field emission theory is presented, including a discussion on particular aspects of field emission from semiconductors. A description of the field emission measurement system is presented, in

which a custom-designed UHV chamber was employed, and a planar diode configuration was utilized for the experiments. The films were measured in an electrically isolated closed circuit, with only one active device used for both voltage sourcing and current measurement. The measurements were taken under a variety of conditions to a) establish the threshold emission properties of BN films *in vacuo*, b) characterize the emission under a variety of gas environments, established by the exposure of the BN films to various gases at varying pressures for varying lengths of time, namely xenon, oxygen, water vapor, and air, chosen specifically to simulate the space environment in the vicinity of an ion propulsion system. Computer-based virtual instrumentation control was integrated with GPIB programmable source, measurement, and guage controllers. The experiments were performed in order to gain insight into the durability, repeatability, and recovery characteristics of the electron emission from the BN films under these conditions. Results indicate an attractively low emission threshold on the order of 2-25 V/μm for our thin films. Furthermore, our films display basically unaffected emission characteristics under exposure to Xe and Air environments at pressures on the order of 10^{-5} torr. Electron emission is supressed under oxygen exposure at 10^{-5} torr, but is shown to recover to pre-exposure level approximately 30 minutes after exposure. Subject to water vapor at comparable pressure, BN displays a slight enhancement in the level of emission.

The morphological characterization data of the samples in Chapter III and the field emission measurement data from Chapter IV inform the data reduction and analysis of the field emission, developed in Chapter V. A model for the asperities

identified in the AFM measurements of Chapter III is adopted, and used in the calculation of an effective work function for our films, using generalized Fowler-Nordheim theory and measured data. A comparison is made with *ab initio* values available in the literature and the discrepancies are discussed. In addition, statistical factors are addressed which are inherent in the emission measurement of nanotextured films composed of a self-assembled asperities, not yet accounted for in the generalized theory. The statistical implications of a distribution of asperity radii are examined, and a rudimentary model is proffered to address the impact of the diffusion of adsorbates on the surface. The combined effects of feature geometry and adsorbates on measurement noise are discussed.

Finally, we summarize our conclusions and discuss in Chapter VI ideas for future study of electron emission from BN thin films.

CHAPTER II

SAMPLE PREPARATION

2.1 BN Thin Film Deposition

Sputtering is a Physical Vapor Deposition (PVD) based method that is very versatile for the preparation and processing of thin films, as the technique may be adapted for deposition as well as etching of thin films. It is used extensively in the semiconductor manufacturing environment [6]. A very simplified description of the sputtering process is provided herein (for more details refer to [27]) . The basic configuration of a sputter deposition set-up is a target (cathode), a substrate (anode) and a power supply for biasing the electrodes placed within a growth chamber. A DC or RF bias may be utilized. A gaseous plasma source (usually Argon gas) is introduced into the space between the electrodes, and a plasma discharge is created. Under certain optimum conditions of gas flow, chamber pressure and electrode bias conditions, a sustainable plasma is generated. The positive ions are accelerated towards the target (cathode), and a fraction of these ions undergo inelastic collisions with the surface atoms (see Figure 2.1). The maximum energy transfer occurring in

these situations can be described by an energy transfer function given by:

$$\frac{E_t}{E_i} = \frac{4m_i m_t}{(m_i + m_t)^2} \tag{2.1}$$

where E_t, E_i, m_i, and m_t are the energy transferred to the surface atom, energy of the incident ion, mass of incident ion and mass of target atom respectively. If the energy transferred in such a collision exceeds the energy required to break the surface bonds of a target atom, the atom may be ejected (or sputtered) from the surface. Based on the orientation of the substrate with respect to the target, as well as chamber operating pressures, some of these sputtered atoms may land on the surface of the substrate where they may condense and form part of a growing film. The sputter yield, which is the number of sputtered target species per incident ion, is used to quantify the efficiency of this process. Sputter yield is a complex function of ion energy, surface binding energy of the target species, energy transfer function and other parameters.

Another outcome of the interaction between an ion and the target could be the release of one or more secondary electrons, some of which are accelerated due to the potential difference between the electrodes and may gain sufficient energy to ionize the gas atoms thereby sustaining the plasma discharge to ensure the continuity of the sputtering process.

Typically, gaseous species are used as plasma sources as they are easiest to ionize. Additionally, rare gases are used because they are inert species that do not chemically interact with the target and other surfaces in the chamber. Argon gas is typically used for sputtering applications.

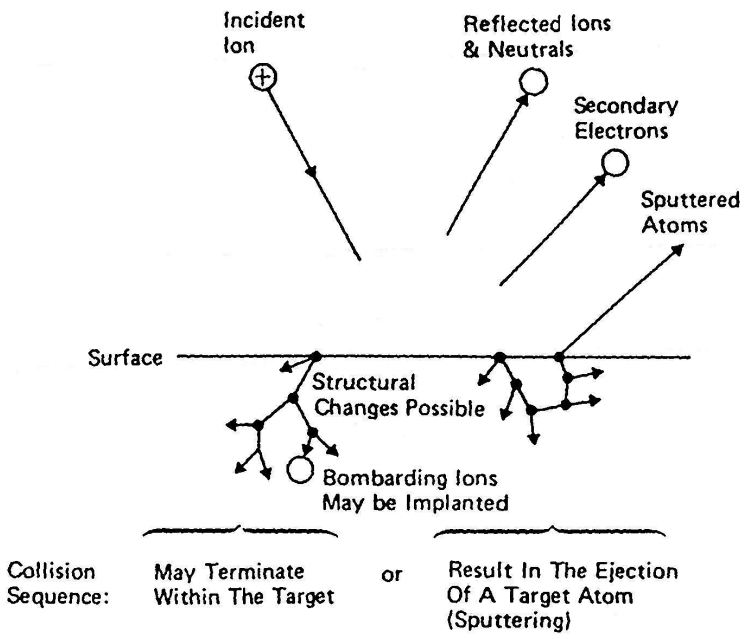

Figure 2.1: Schematic of the sputtering ion interaction with the surface of the source material target during the sputtering process. The sputtering ion used in our system is Argon.

DC biasing was first used for sputtering applications, however, it could not be used for sputtering from insulating targets due to charge buildup on the target surface and the subsequent extinction of the plasma. A high frequency (RF) biasing scheme was found to circumvent this problem. RF magnetron sources typically operate at a frequency of 13.56 MHz.

Magnetron sputtering utilizes a magnetic field located close to the sputtering target. This enables the localization of secondary electrons close to the target surface, thereby increasing the efficiency of the gas ionization process and also enabling the reduction in the operating pressure of the deposition system. This leads to a higher quality film being deposited on the substrate as the sputtered species undergo fewer energy dissipating collisions en route to the substrate (see Figure 2.2).

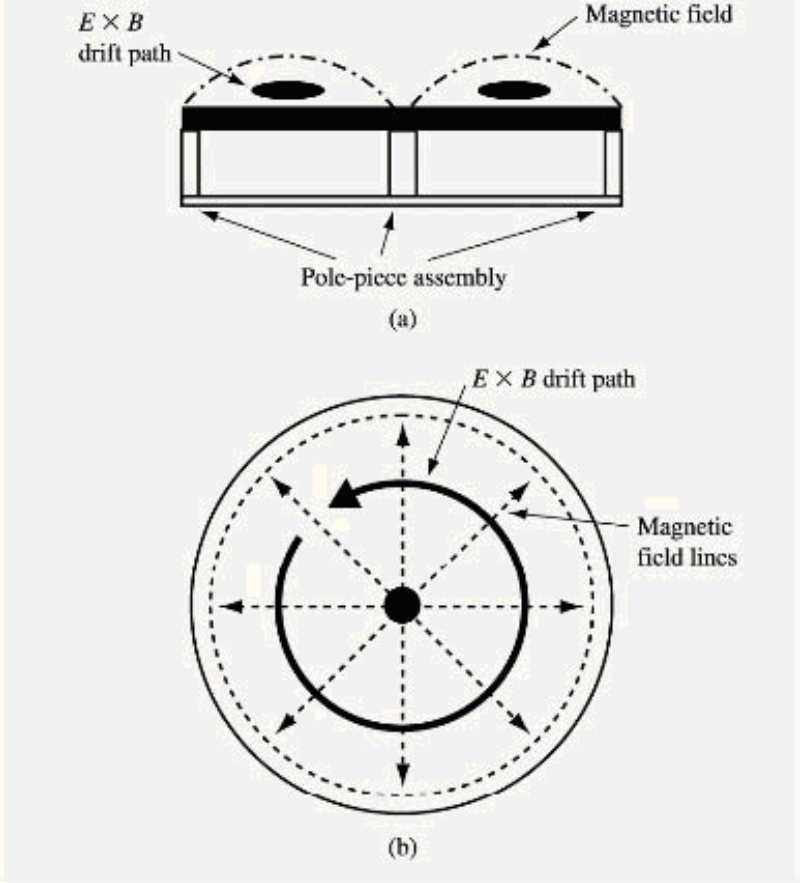

Figure 2.2: Depiction of the side (a) and top (b) views of the electron trajectory above a planar cylindrical magnetron cathode (from [6]).

Plasmas can also be generated using Electron Cyclotron Resonance (ECR) plasma sources. This method can be used to create a high density plasma at low pressures (typically lower than $\sim 1 \times 10^{-3}$ torr). A simplified description of the operating principles behind this method is presented (a detailed account is found in [28]). Electrons present in an ECR Discharge volume oscillate about the existing magnetic field lines at a frequency given by:

$$\omega_{ce} = \frac{eB}{m_e} \tag{2.2}$$

where ω_{ce}, e, B, and m_e are the electron cyclotron frequency, electron charge, mag-

netic field magnitude and electron mass respectively. If microwave radiation of frequency $\omega = \omega_{ce}$ is effectively coupled into the discharge volume, the microwave power is absorbed primarily by the discharge electrons which consequently are accelerated and undergo inelastic and elastic collisions with neutral gas atoms present in the discharge, resulting in the ionization of some of those neutrals and consequently sustaining the plasma discharge. An opening is present to provide the ions access to the substrate. Sustained ignition of the plasma is strongly dependent on conditions such as discharge crucible gas pressure, gas flow rates and gas type. The microwave frequency of operation of ECR sources is typically 2.45 GHz. The much higher frequency of the ECR source compared to that of the RF sputtering source is advantageous in reducing electromagnetic coupling when the two sources are operated simultaneously in close proximity to each other. Growth of cubic boron nitride has been successfully implemented on Silicon (100) substrates utilizing an Ion Assisted Magnetron Sputtering technique [29]. A schematic of the growth chamber setup is provided in Figure 2.3.

2.2 BN Thin Film Deposition System

Substrates are introduced into the system individually (Fig. 2.3), through a turbo-pumped load-lock chamber, which typically reaches pressures of $\sim 1 \times 10^{-7}$ torr before the substrate is transferred to the adjacent UHV growth chamber. The growth chamber is cryo-pumped and can achieve a base pressure of 9×10^{-10} torr after bake-out. The UHV environment allows for the thermal desorption of any silicon substrate oxide prior to growth, and also ensures a clean environment for film deposition. The

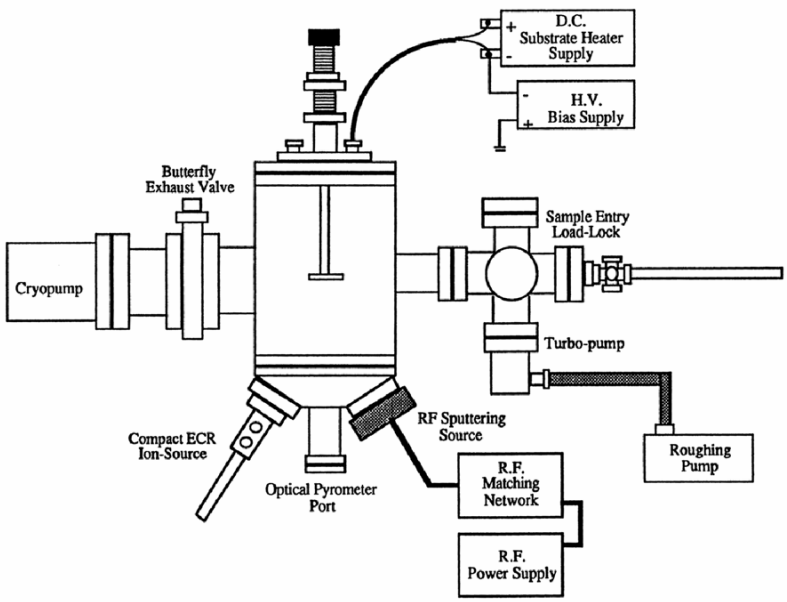

Figure 2.3: Schematic of the UHV system for ion-assisted thin film deposition of boron nitride.

elimination of water vapor from the inside of the chamber surface is particularly important in this respect. The reactive sputtering of a hexagonal BN target of 99.99% purity, performed using a UHV 2-inch planar RF magnetron source mounted in a source-up configuration on the base flange assembly, supplies source material for the growth of the cubic thin films. RF power at 13.56 MHz is supplied to the sputtering source. A high-field Neodymium Iron Boride magnet provides additional electron confinement to enable source operation at pressures down to $\sim 8 \times 10^{-4}$ torr in an Argon/Nitrogen gas environment. For these studies an Astex^{TM} Compact ECR Ion Plasma source was also mounted on another port of the base flange, at an optimal angle and distance from the substrate to immerse it in the Nitrogen plasma it generates, while being well removed from the plasma confinement region. This additional source of Nitrogen ions to the growth environment helps to maintain the proper stoichiometry of boron and nitrogen for optimum *c*BN formation. During

growth the substrate is heated up to 1000 °C, and a negative DC potential of up to ∼100 V is applied to the substrate to optimize the incident energy of the ions. The substrate bias was reduced to ∼-56 V after crossing the cubic phase nucleation transition, a technique which has been shown to yield a higher degree of order within the film surface [30].

2.2.1 BN Sample Growth Parameters

Boron nitride films were grown on p-type (Boron doped) Silicon (100) substrates, of resistivity ρ = 2 - 10 Ω-cm. The growth chamber base pressure was 9×10^{-10} torr prior to the introduction of the Argon sputtering gas and the Nitrogen gas for the ion source, both at flow rates of 10 sccm. The pumping speed was controlled to sustain a growth pressure of 1 $m$torr. The RF sputtering gun power was stabilized at 500 Watts forward power, with a maximum 3 Watts reflected power. The substrate was heated to up to ∼1000 °C using a custom heater stage with a boron nitride coated resistive heating element, against which the substrate was mounted[1]. The temperature was monitored using optical pyrometry through a viewport on the base flange of the growth chamber, optimized for measurement of the silicon substrate temperature, and using an emissivity value of 0.7 at a wavelength of $1.0 \pm 0.1\,\mu$m [31]. The stage was heated using a Sorensen$^{\text{TM}}$ power supply set at 65 V and 4.4 Amps. The power supply for the ECR plasma source, which uses a travelling wave tube to generate the microwaves used to ignite and sustain the Nitrogen ion source, was set at ∼100 Watts forward power, and impedence matched using a tuning short with a reflected

[1]Direct heating can also be used to heat the silicon substrate by passing a DC current through the Si substrate itself. The samples for this study were grown using the boron nitride coated resistive heater.

	SN110	SN124	SN124b	SN133	SN134
Growth Temp. ($^\circ$C)	∼940	∼1000	∼1000	∼1000	∼1000
Growth Pressure ($m$torr)	1.0	1.0	1.0	1.0	1.0
Initial Substrate Bias (V)	∼85	∼96	∼96	∼96	∼96
Initial Substrate Bias Time (h)	7.0	3.0	3.0	3.0	3.0
Reduced Substrate Bias (V)	NA	∼56	∼56	∼66	∼56
Reduced Substrate Bias Time (h)	NA	2.5	2.5	8.5	7.5
N_2 Gas Flow (sccm)	10.0	10.0	10.0	10.0	10.0
Ar Gas Flow (sccm)	10.0	10.0	10.0	10.0	10.0
Sputtering Gun Power (W)	500	500	500	500	500
ECR Power (W)	100	100	100	100	100

Table 2.1: Growth parameters for cubic boron nitride films, including samples analyzed for field emission

power minimum setting of 6 Watts. The ECR plasma confinement electromagnet power supply current was set to ∼20 Amps. The films were grown at a substrate bias of ∼96 V for 3 hours, until the cubic phase of boron nitride was achieved, as determined by *in situ* Reflection high energy electron diffraction (RHEED), as described in Chapter III. Subsequently, the growth was continued at a substrate bias reduced to ∼-56 V. Film thicknesses for cBN films used were ∼2000 Å. Table 2.1 lists the parameters for the films used in the subsequent study documented in this dissertation.

An investigation into the microstructure of *as grown* cubic boron nitride films using Transmission Electron Microscopy was performed by Kidner [29]. Based on the High Resolution TEM Micrograph (Fig. 2.4) of a cross section of a cubic boron nitride film, three distinct regions were observed in the film structure. A very thin amorphous layer ($\sim 4\,nm$) was observed at the silicon interface. Above that, a

textured layer was observed having a thickness of $\sim 30\,nm$. From the fringe spacing, it was determined to be turbostratic hexagonal Boron Nitride with its c-axis oriented parallel to the plane of the substrate. Turbostratic refers to a crystalline structure where the basal planes have slipped and rotated relative to each other, causing the spacing between planes to be greater than in the bulk. It is above this buffer layer that the nucleation of the cubic phase occurs.

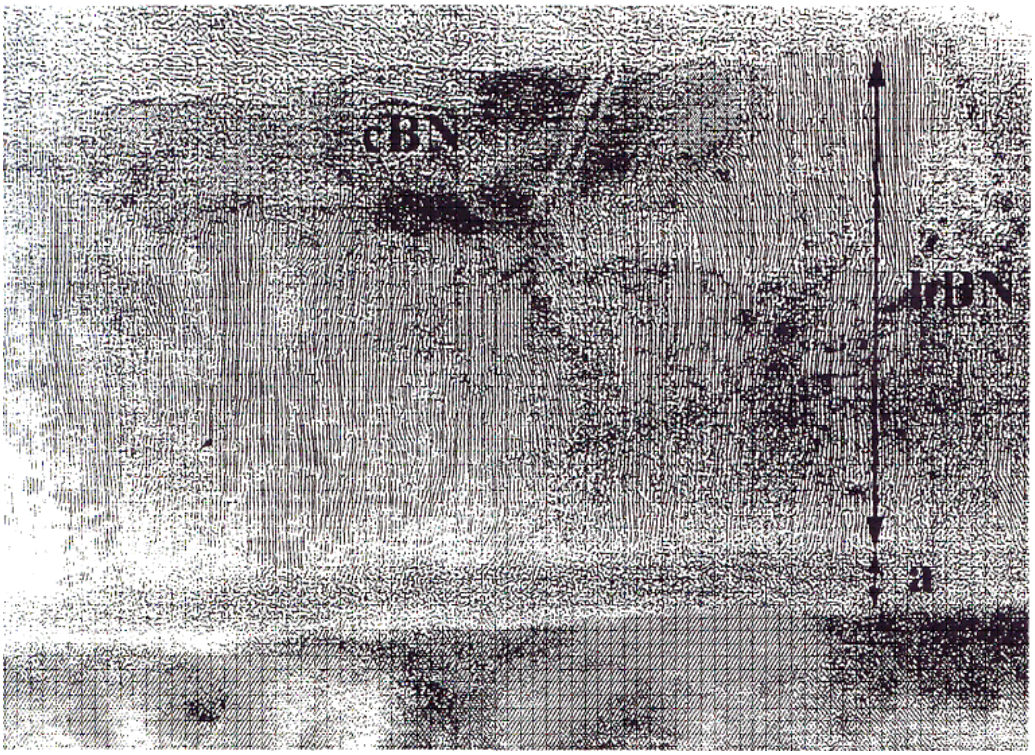

Figure 2.4: Cross sectional High Resolution TEM Image of Boron Nitride sample grown by Ion Assisted Magnetron Sputtering technique. The "a" at the bottom right of the image identifies the amorphous boron nitride layer [7].

2.3 Summary

We have presented the reduced bias thin film growth technique, used with the ion-assisted RF sputtering process, as the method for the fabrication of the *c*BN

films that were the subject of the field electron emission research presented in this dissertation. The samples were grown in an Argon/Nitrogen gas environment, at a growth pressure of 5 mtorr on p-type Silicon (100) substrates, of resistivity $\rho = 2$ - 10 Ω-cm, subject to a substrate bias of ∼100 V for 3 hours, until the cubic phase of boron nitride was achieved. Subsequently, the substrate bias was reduced to ∼-56 V, and growth continued for an additional 8 hours, yielding cBN film thicknesses of ∼2000 Å. *As grown* cubic boron nitride films display three distinct regions in the film structure: a very thin amorphous layer of BN $\sim 4\,nm$ in thickness, a turbostratic hexagonal Boron Nitride layer ($\sim 30\,nm$ thick), above which the cubic phase nucleates.

CHAPTER III

BORON NITRIDE MATERIAL AND MORPHOLOGICAL CHARACTERIZATION

3.1 Introduction

Here we present the techniques employed for the material and morphological characterization of the BN films subsequently subjected to field emission studies. Those techniques include Reflection High Energy Electron Diffraction, Fourier Transform Infrared Spectroscopy, and Atomic Force Microscopy.

3.2 RHEED

Reflection high energy electron diffraction (RHEED) has a history dating back over 60 years to when electrons were first characterized as having a wave-like nature. It is the constructive and destructive interference of this characteristic of elastically diffracted high energy electrons (at $\sim$10 to 100 keV, with beam intensity $\sim 1mA$, or 10^{13} electrons per second) incident on a thin crystal, in conjunction with the intrinsic periodic nature of the crystal lattice that makes RHEED patterns so useful in the structural characterization of thin film crystals. The beam is diffracted from the film at angles of grazing incidence ($\sim$0.05 rad, or $\sim 3^{\circ}$), and thus penetrates the surface of

a crystal to less than $1\,nm$ ($\sim$10Å), where penetration is defined as a fall off of 1/e in intensity of the elastically diffracted beam. Under certain conditions of diffraction, this penetration is confined to the top one or two monolayers of the crystal, making the technique particularly qualified for the characterization of thin film surfaces and their structure. The kinds of information typically obtained from RHEED pertain to:

(a) Quality of the surface, in terms of roughness, from pattern recognition

(b) Orientation of the crystal, or a grain of crystal (crystallite), again from pattern recognition

(c) Crystal structure and morphology of the surface, from quantitative analysis of diffraction angles and intensities in the RHEED pattern

3.2.1 RHEED Theory

RHEED images are created on a phosphor screen, as the electron beam is incident along a high symmetry direction of the crystal surface, creating diffraction maxima at positions on the phosphor that satisfy the Laue diffraction condition,

$$(\vec{\mathbf{k}} - \vec{\mathbf{k}}') \cdot \vec{\mathbf{a}} = m \cdot 2\pi \tag{3.1}$$

where $\vec{\mathbf{k}}$ is the momentum of the incident electron, $\vec{\mathbf{k}}'$ is the momentum of the diffracted electron, and m is an integer and $\vec{\mathbf{a}}$ is any superposition of real-space basis vectors ($\vec{\mathbf{a}} = \mathrm{c}_1\vec{\mathbf{a}}_1 + \mathrm{c}_2\vec{\mathbf{a}}_2 + \mathrm{c}_3\vec{\mathbf{a}}_3$; c_1, c_2, $\mathrm{c}_3 \in \mathbb{Z}$) for the crystal lattice. This condition is fulfilled if ($\vec{\mathbf{k}}$ - $\vec{\mathbf{k}}'$) = $\vec{\mathbf{G}}$, where $\vec{\mathbf{G}}$ is any superposition of the corresponding reciprocal lattice basis vectors.

For a bulk crystal, bright diffraction spots are observed when the change in momentum of the electron, ($\vec{\mathbf{k}}$ - $\vec{\mathbf{k}}'$), is a reciprocal net vector $\vec{\mathbf{G}}$. RHEED uses the same basic diffraction principle, but also includes two additional significant factors:

1. the real-space lattice of a perfectly flat surface is *two*-dimensional, and

2. for *elastically*-scattered electrons, $|\vec{\mathbf{k}}| = |\vec{\mathbf{k}}'|$.

A two-dimensional surface lattice has real-space lattice vectors only in the surface plane because the abrupt break in symmetry in the normal direction is equivalent to an infinite out-of-plane crystal period. The corresponding reciprocal-space lattice then is an array of rods positioned at the reciprocal net points, extending in the normal direction. Essentially the reciprocal space representation of a 2-dimensional surface is a series of Bragg rods[1] normal to the surface, as detailed in Figure 3.1. The RHEED image may be construed to result from the intersection of these Bragg Rods with the Ewald sphere, diagrammed in Figure 3.2. The Ewald sphere is a geometric construct which is used to graphically represent the relationship in reciprocal space between the momentum of the incident electrons, the diffraction angle for the given incident beam, and the reciprocal lattice of the diffracting crystal in satisfying the momentum conservation requirement (Equation 3.1). Figure 3.3 displays an integrated 3-dimensional perspective of the RHEED beam interaction with a film surface. A detailed description of the RHEED technique is available in a review by Arrott [32].

[1] also referred to as "Crystal Truncation rods".

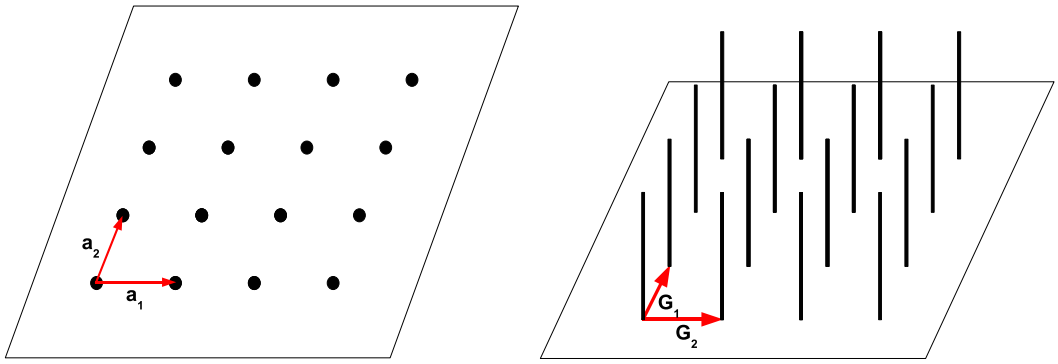

(a) (b)

Figure 3.1: A sample surface lattice. The rods in reciprocal space are rows of reciprocal lattice points separated by an infinitesimally small $\Delta\vec{\mathbf{k}}_3$, resulting from the infinite out-of-plane period on the real-space surface. (a) represents real space lattice with vectors ($\vec{\mathbf{a}}_1$, $\vec{\mathbf{a}}_2$). (b) represents reciprocal space lattice with corresponding vectors ($\vec{\mathbf{G}}_1$, $\vec{\mathbf{G}}_2$)

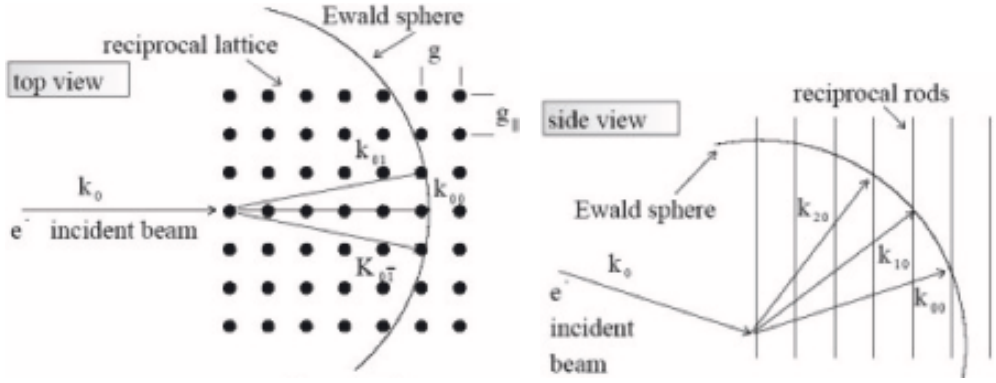

(a) (b)

Figure 3.2: Reciprocal lattice intersection with the Ewald sphere for a square lattice. (a) shows the top view of the reciprocal lattice intersection with the Ewald sphere; (b) shows the side view.

3.2.2 RHEED Measurement System

The RHEED data of the films grown for this study are generated using a Vieetech™ 30 *k*eV electron gun and a phosphor screen. A CCD detection and analysis system (k-

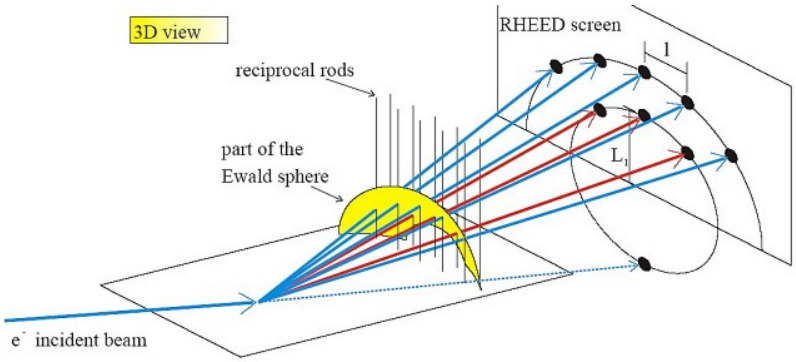

Figure 3.3: A 3-dimensional rendition of RHEED diffraction pattern imaging.

Space Associates, Model KSA 300) is used for diffraction pattern image acquisition and analysis. The electron gun and phosphor screen, primary equipment components in RHEED, are mounted on the growth vacuum chamber, and oriented relative to the film and to one another so as to permit the high energy electron beam to be incident on the film surface at a glancing angle ($\sim 3^{\circ}$), as the phosphor screen captures the diffraction pattern, as sketched in Figure 3.4.

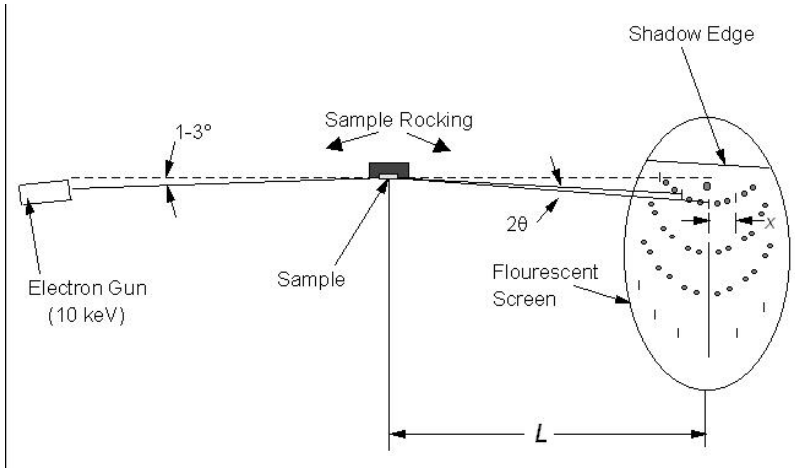

Figure 3.4: Schematic of RHEED diffraction pattern imaging.

3.2.3 RHEED Data

Relevant to RHEED investigation of the boron nitride thin films grown for our study, Taylor has demonstrated the notable difference between the RHEED diffraction images of the pre-cBN-nucleation hBN/tBN film and those captured post-cBN nucleation as anticipated, based on the difference in crystal structure [33]. RHEED images of pre-cBN-nucleation thin films reveal a two ring pattern. From measurements of the ring radii and comparison with crystallographic data of hBN, these rings are attributed to scattering off the (0002) and $(10\bar{1}2)$ planes. In the case of cBN, a three ring pattern is observed which can be indexed to the predicted (111), (220) and (311) crystallographic reflections.

This RHEED data acquisition technique provides a convenient way to monitor the nucleation of the cubic phase in the film growth process *in situ*, facilitating the shift to the reduced bias growth phase of the deposition process where the transition from hexagonal structure to cubic structure occurs.

From RHEED images obtained one can glean a substantial amount of information regarding the surface crystallinity, morphology and texture. If the surface is of high crystalline quality (eg. Bare clean Si (100) surface, as in Figure 3.5), one observes spots and Kikuchi lines in the RHEED image [34]. Kikuchi lines represent specific directions, or channels, in a high quality crystal where electrons can propagate, gradually giving up their energy in inelastic collisions. In contrast, for RHEED images of polycrystalline films like BN one observes the ring-like patterns, with indications of the presence of the various crystal phases as well as evidence of texture for each

phase (Figure 3.6). Generally speaking, angular spread (or rings) in the diffraction pattern corresponds to *in-plane* variations of the crystal, which are typical of a polycrystalline thin film surface. The radial width of diffraction maxima in the vertical direction generally correspond to *out-of-plane* variations in the crystal structure of the surface. Note that the appearance of rings or arcs in the RHEED diffraction patterns indicate that the surface morphology is composed of polycrystalline grains of BN. The grains may be randomly oriented (giving a completely uniform ring) or there may be preferential orientation as in a textured surface. In that case the diffraction pattern consists of arcs the circumferential length of which is a measure of the in-plane misorientation.

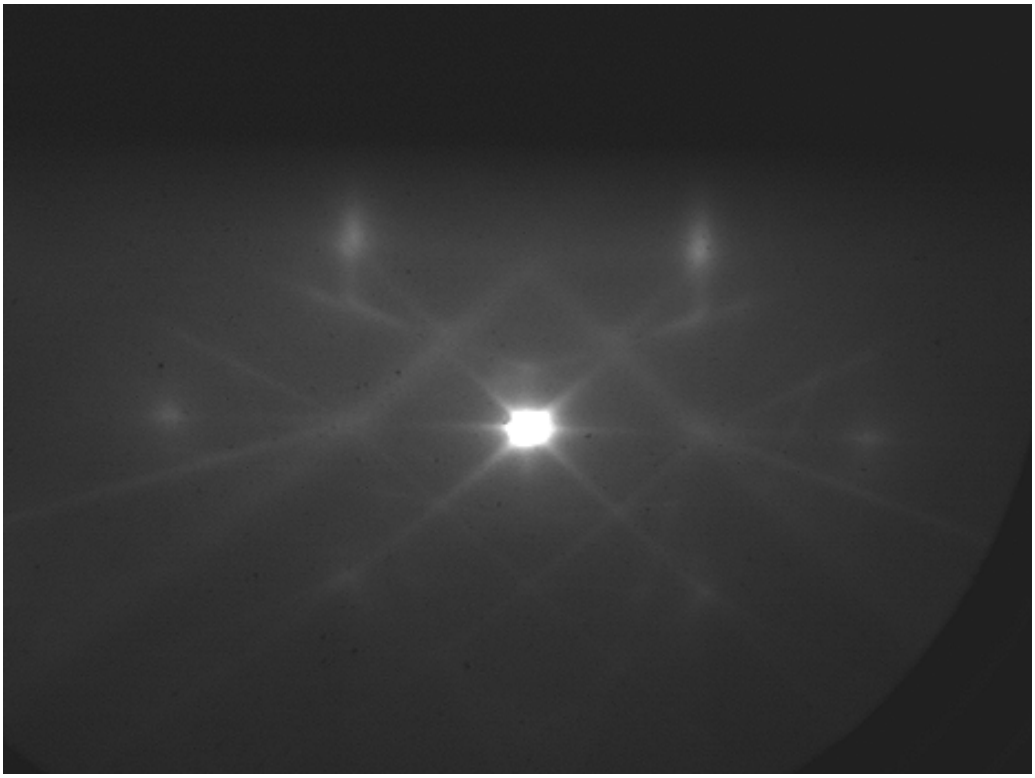

Figure 3.5: RHEED image of bare Si (100) substrate, with characteristic Kikuchi lines visible.

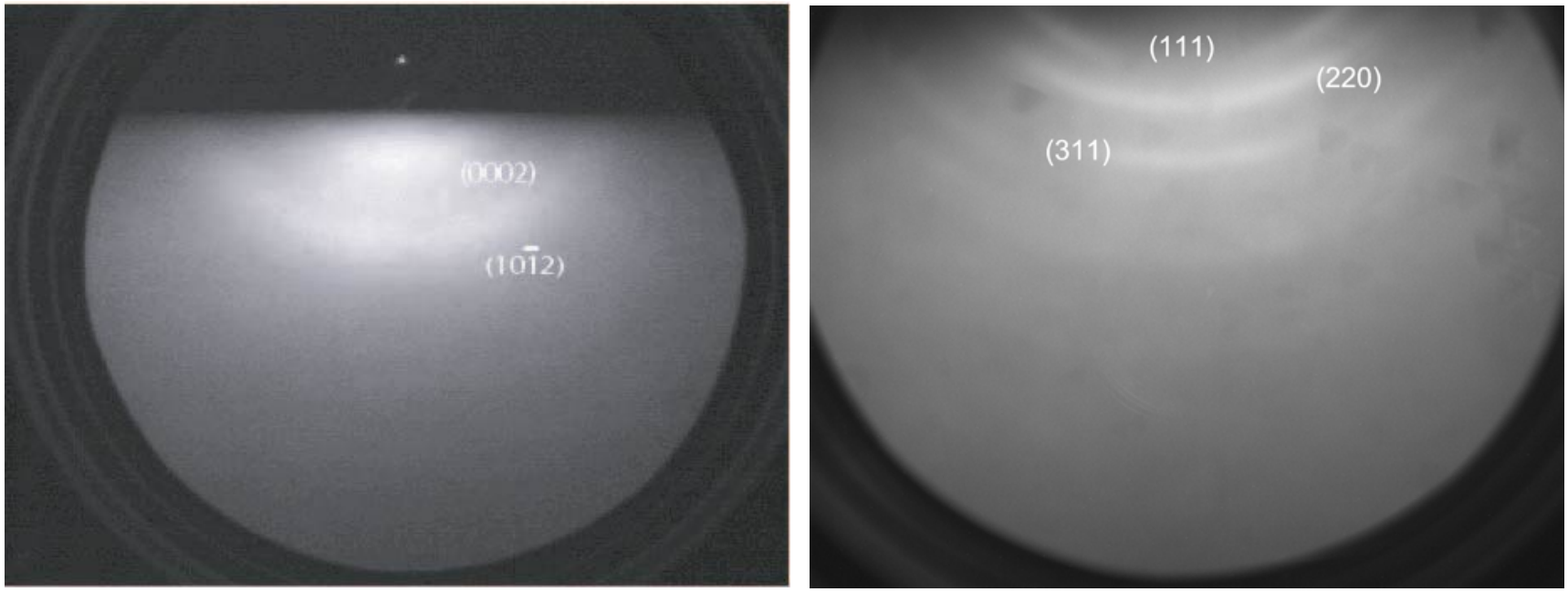

(a) (b)

Figure 3.6: RHEED patterns generated by boron nitride film surfaces. (a) is a RHEED image of hexagonal (turbostratic) boron nitride film on Si (100) substrate. (b) is a RHEED image of cubic boron nitride film on Si (100) substrate.

3.3 FTIR

3.3.1 FTIR Theory

Fourier Transform Infrared Spectroscopy (FTIR) is a very useful structural characterization method for the boron nitride system in that it can help identify the different phases of boron nitride present in the films, enabling a qualitative assessment of the crystallinity of each individual phase present, as well as a quantitative assessment of the percentage composition of all phases comprising the film [35]. The technique, which uses interferometry as opposed to a conventional dispersive spectrometer, can be used in either reflectance or transmission mode to characterize the surface and film cross-section respectively.

Molecules typically possess characteristic vibrational modes in the infra-red region of the spectrum. A subset of these vibrational modes are infra-red active i.e. there is a change in the electric dipole moment during a vibrational cycle. This constraint constitutes a "selection rule" for infrared modes [36, 37]. If the molecule possesses an infra-red active mode, it will absorb energies at specific eigenfrequencies unique to particular vibration modes. This will be manifest in the interferogram signal exiting the sample, and after a Fourier transform of that detector signal, the absorption spectrum of the material may be extracted.

3.3.2 FTIR Measurement System

Interferometric spectroscopy (as depicted in Figure 3.7) is utilized to obtain FTIR data. Radiation emitted from a broadband infrared source consisting of a hot filament is incident on a beam splitter. The transmitted beam is incident on a movable mirror

and after reflection combines with the reflected beam. This results in constructive or destructive interference at the beamsplitter. Each frequency of radiation will present a unique signal at the beamsplitter, and thus a broadband source will present a signal that is a superposition of all the individual frequencies, which is then made incident on the sample. The spectral limits of the setup range from 400 $cm^{-1}$to 4000 cm^{-1}, where (cm^{-1}) represents *wavenumber*, a unit of frequency defined simply as the inverse of the wavelength λ corresponding to a given frequency $\nu = c/\lambda$, where c is the speed of light in air, and having the units of inverse wavelength.

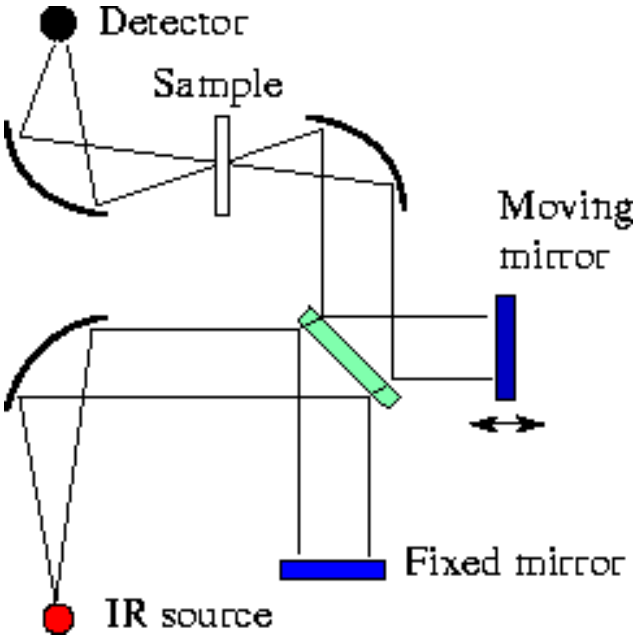

Figure 3.7: A schematic rendition of FTIR Michelson Interferometry.

For the boron nitride films grown for this research, FTIR was performed using a Nicolet Magna IR^{TM} Series II spectrometer in transmission mode (Figure 3.8), providing bulk compositional data. The spectrometer was configured for mid-IR operation, and used a deuterated tri-glycerine sulphate detector in combination with a KBr beam splitter. Samples were mounted on a 2-Circle rotation stage so that mea-

surements may be performed at off-normal incidence to extinguish systematic resonance artifacts in the data. To remove water and carbon dioxide absorption from the spectra the spectrometer is purged continuously with dry nitrogen. Measurements were typically taken approximately one-half hour after a sample was locked into the sample measurement chamber, as an additional precaution against water and carbon dioxide absorption.

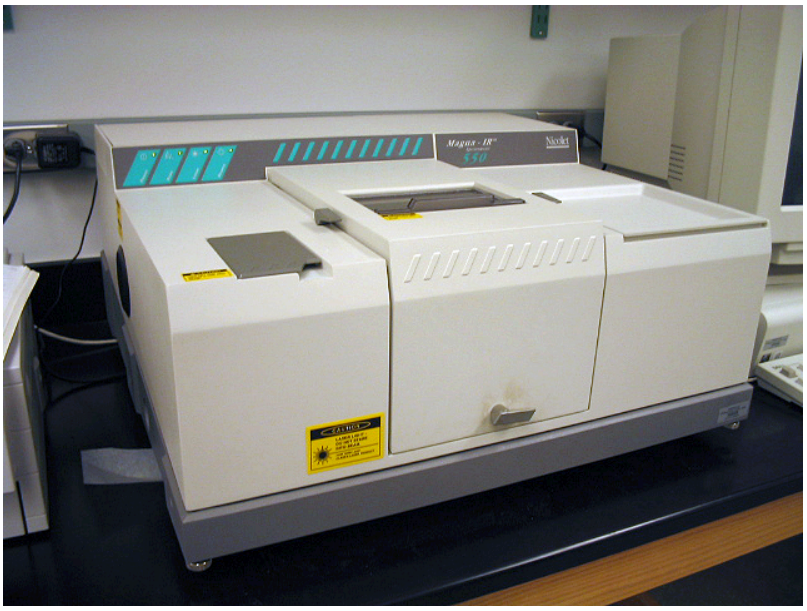

Figure 3.8: Nicolet Magna IR Series II Fourier Transform Infrared Spectrometer.

3.3.3 FTIR Data

For the boron nitride system, hexagonal BN is observed to have infrared active transverse optic phonon modes at ∼783 $cm^{-1}$and ∼1367 cm^{-1} [38]. The 1367 cm^{-1}mode (E_{1u} mode) corresponds to *in-plane* B-N bond stretching while the 780 cm^{-1}mode (A_{2u} mode) corresponds to *out-of-plane* B-N-B bond bending (Fig. 3.9). Typically, variations in sample quality and growth conditions will result in a range of values for the locations of the phonon peaks (770 cm^{-1}– 810 $cm^{-1}$for the A_{2u} mode and

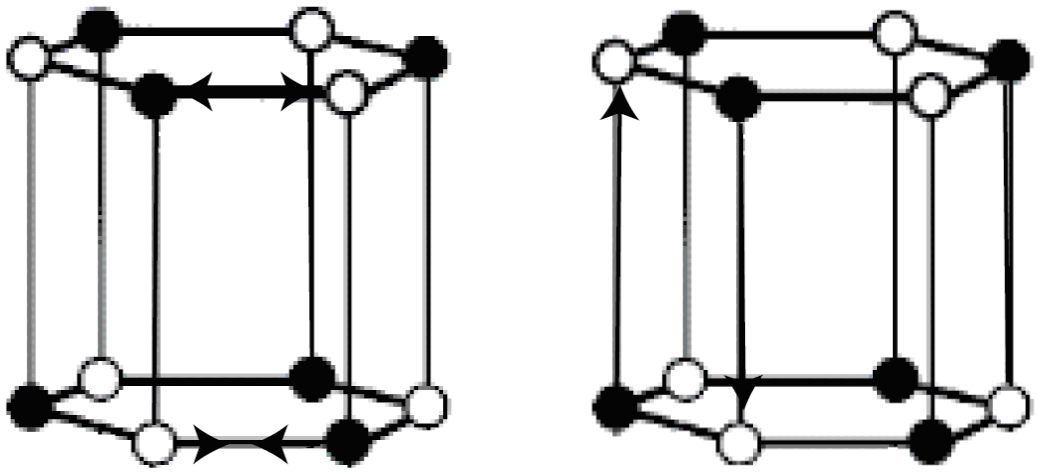

(a) (b)

Figure 3.9: Molecular vibrational eigenvectors corresponding to infrared active modes in hexagonal boron nitride. (a) depicts the E_{1u} mode at 1367 cm^{-1}. (b) depicts the A_{2u} mode at 780 cm^{-1}.

1360 cm^{-1}– 1400 $cm^{-1}$for the E_{1u} mode). For cubic BN, an IR-active transverse optic phonon peak is observed at ∼1065 cm^{-1} [39]. The typical range observed for this phonon peak is 1050 cm^{-1}– 1100 cm^{-1}; the exact frequency depends on parameters such as strain, grain size, temperature, etc. Typical FTIR spectra for hBN films, as well as for the cBN thin film samples, depicting the corresponding signature absorption peaks, are presented in Figures 3.10 and 3.11 for comparison. Besides information related to phase identification, one can also estimate the content of cubic phase from FTIR data. Typically the approach used to estimate the percent cubic phase is based on the relative heights of the cBN 1065 cm^{-1}peak and the hBN 1383 cm^{-1}peak using the relation shown in Equation 3.2 [35]. The samples used for FE measurements, grown under the same conditions, repeatedly showed greater than

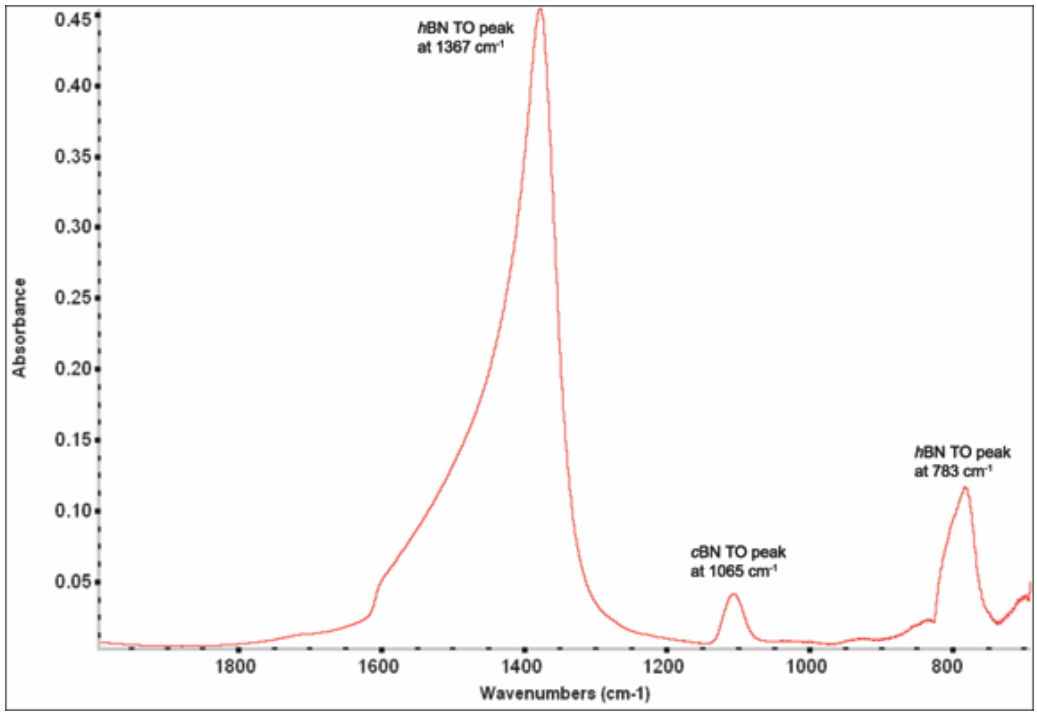

Figure 3.10: Fourier Transform infrared absorbance spectrum for a predominantly hexagonal boron nitride film on Si(100) substrate.

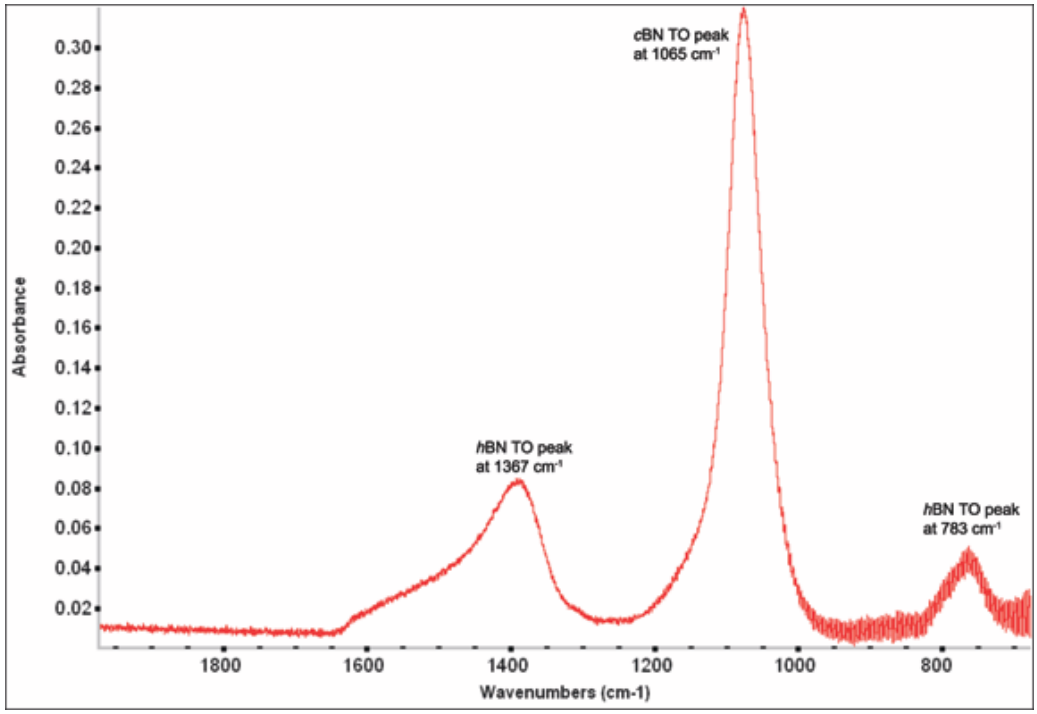

Figure 3.11: Fourier Transform infrared absorbance spectrum for a predominantly cubic boron nitride film on Si(100) substrate.

75% cubic phase.

$$\%\ cBN\ volume\ fraction = \frac{\mathrm{I}(1065)}{\mathrm{I}(1065) + \mathrm{I}(1367)} \times 100\%\ [35] \tag{3.2}$$

Deviations of the peak maxima wavenumbers from the bulk wavenumbers is indicative of strain present in the film [40]. Also, the magnitude of the full width at half maximum (FWHM) of the peaks is indicative of structural order in the film, with a larger FWHM implying greater disorder due to the presence of a wider distribution of local bonding environments [41]. The procedure followed to obtain an FTIR spectrum of a BN film is as follows: first, a spectrum is taken of a bare Silicon substrate wafer that has been cleaned by dipping in a 10% HF acid solution. The spectra of the sample is taken next, and a background subtraction is performed by taking the difference of the two spectra. In this manner, the spectrum of the boron nitride film alone is obtained. Typically 1000 scans were averaged to obtain the final spectrum. The scan resolution was typically 0.06 cm^{-1}.

3.4 AFM

3.4.1 AFM Measurement System

The atomic force microscope (AFM), one of about two dozen types of scanned-proximity probe microscopes, works by measuring height with a probe or "tip" placed very close (within nanometers) to the sample. The small probe-sample separation (on the order of the instrument's resolution) makes it possible to take measurements over a small area.

The instrument is essentially an extremely high resolution profilometer. A silicon

nitride or silicon tip is scanned across the surface of a sample at a constant force, the position of the tip on the sample surface being controlled by three piezoelectric ceramics. These piezoelectrics are controlled by a microcomputer which monitors the position of the tip via the signal from a photodiode which receives reflected laser light from the top of the tip support. Two dimensional scans allow the construction of images of the sample surface, rather than just line profiles. The instrument is capable of imaging areas as large as 125 μm^2 and as small as a few tens of nanometers square. The maximum spatial resolution is such that the atomic surface of the structure may be revealed.

To acquire an image the microscope raster-scans the tip over the sample while registering the change in height of the tip. This monitoring takes place as the changing position of a laser beam reflecting off of the probe is detected through a position-sensitive laser detector, as depicted in Figure 3.12. Consequently, the atomic force microscope measures topography with an atomic force probe. Specifically, AFM operates by measuring attractive (van der Waals) or repulsive forces between a tip and the sample [42]. In its repulsive "contact" mode, the instrument lightly touches a tip at the end of a leaf spring or "cantilever" to the sample. As a raster-scan drags the tip over the sample, the laser detection apparatus measures the vertical deflection of the cantilever, which indicates the local height at that location on the sample. Thus, in contact mode the AFM measures hard-sphere repulsion forces between the tip and sample. The resulting image resembles an image on a television screen in that both consist of many rows or lines of information placed one above the other.

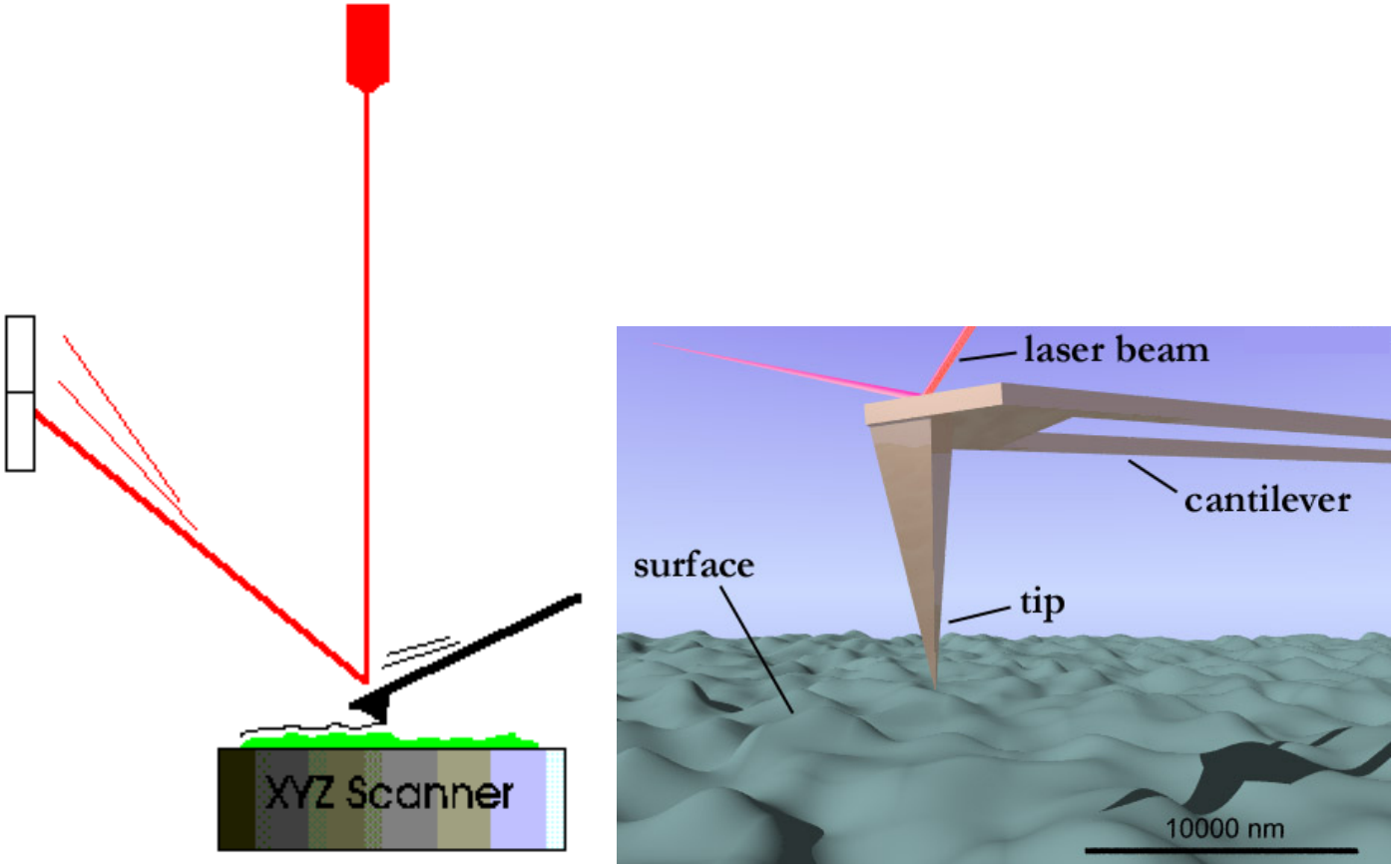

(a) (b)

Figure 3.12: Illustrations of Atomic Force Microscopy, using an optical cantilever.

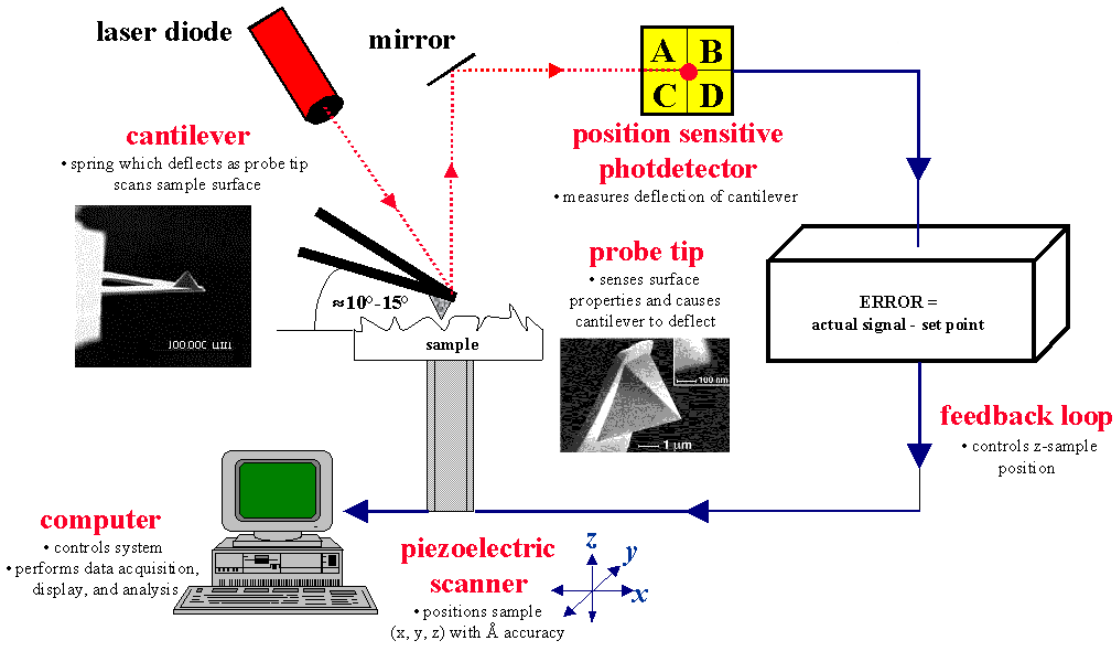

Figure 3.13: A sketch of the Atomic Force Microscopy setup.

Figure 3.13 displays the configuration of the general components of the instrument used for these measurements.

In contact AFM, the tip is in perpetual contact with the sample. The tip is attached to the end of a cantilever with a low spring constant, lower than the effective spring constant holding the atoms of most solid samples together. As the scanner gently traces the tip across the sample (or translates the sample under the tip), the contact force causes the cantilever to bend and the Z-feedback loop works to maintain a constant cantilever deflection. An intermediate scan option is the "tapping mode" in which the tip is under resonance and intermittently contacts the surface. The frequency and phase of the motion of the cantilever is used to gain even more sensitive information on the surface topography.

3.4.2 AFM Data

A Digital Instruments Nanoscope III^{TM} Multimode Scanning Probe Microscope, in combination with the Atomic Force probe, called a piezoelectric transducer (PZT) (Figure 3.14), was used in contact mode for our measurements. The cantilever is a microfabricated Si tip integrated into a triangular support, with a force constant of between 0.03 and 0.06 N/m. Samples were scanned with a J-tube PZT with 9.5×9.5 μm^2 scan range in the film plane, and 5.4 μm scan range in the direction normal to the sample surface. The scan rate was 4 lines/second. Only standard planefit (surface-leveling) correction was applied to the images. The image size was 512×512 pixels, resulting in an acquisition time of 3 minutes. All images were checked for rotational and scaling variability to insure that the observed features were not artifacts of the triangular geometry of the cantilever.

AFM images (Figure 3.15) were analyzed using the Nanoscope SPM software. The average feature height, $\langle \mathrm{c} \rangle$, was calculated to be $79\,n$m, with a mean *RMS* roughness of $19\,n$m. The grain size mean, $\langle \mathrm{gs} \rangle$, was $155\,n$m^2, with a standard deviation σ_{gs} of $84\,n$m^2, yielding a mean feature radius $\langle \mathrm{b} \rangle \simeq 7\,n$m. Statistics were calculated from an area of $853\,n\mathrm{m} \times 866\,n\mathrm{m}$ ($= 0.74$ μm^2), with the average number of grains measured at 294.

AFM images also provided a qualitative insight into the geometry of the surface features, which appear conical with a blunted apex, closer to the shape of a prolate ellipsoid of revolution bisected at its semi-minor axis with the plane normal oriented parallel to its semi-major axis, and with its apex furthest from the substrate surface.

Figure 3.14: Digital Instruments Nanoscope III^{TM} Multimode Scanning Probe Microscope, in combination with the Atomic Force probe.

3.5 Summary

We have presented the data from three characterization techniques which reveal the morphology and composition of the boron nitride thin film samples prepared for this field emission study.

From the RHEED data of the films under study, we were able to identify the crystal structure at the surface to be qualitatively *c*BN. The data shows the sample to be a polycrystalline film rather than a single crystal, composed of partially oriented crystallites of *c*BN with a distribution of different crystal plane normals oriented relatively parallel to the Si substrate surface normal as indicated by the (111), (220), and (311) crystallographic reflections in the RHEED data. The distribution of *in-*

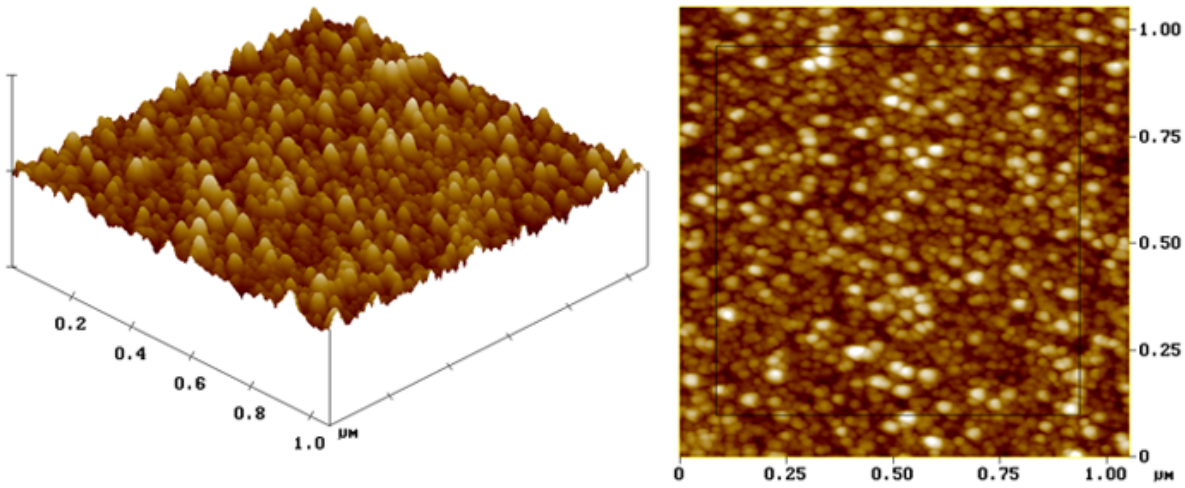

Figure 3.15: AFM Image of cubic boron nitride film on Si(100) substrate, with an areal density of 397.63 emission sites per square micrometer [8].

plane relative orientation of these crystallites is evidenced by the azimuthal spread in the RHEED images. The radial spread in the diffraction maxima indicate the out-of-plane variation of the crystallite orientation, contributing to surface roughness.

The FTIR data showed our films to be overwhelmingly *c*BN in constitution, with a volume fraction greater than 75%. Although this data does not directly determine the phase constitution at the film surface, since it is taken in transmission mode, it reasonably establishes a lower limit of surface *c*BN fraction, independent of data from any of the complementary techniques.

The AFM images provide data which is analyzed to give surface roughness and feature size information for the films used in our field emission experiments. We measured $\langle \mathrm{c} \rangle = 79\ nm$, with a mean *RMS* roughness of 19 nm. $\langle \mathrm{gs} \rangle = 155\ nm^2$, with $\sigma_{\mathrm{gs}} = 84\ nm^2$, yielding $\langle \mathrm{b} \rangle \simeq 7\ nm$. Data was calculated over an area of 0.74 $\mu \mathrm{m}^2$, containing on average 294 grains.

CHAPTER IV

FIELD EMISSION MEASUREMENTS

4.1 Field Emission Theory

Field electron emission occurs when an electric field, F, applied external to the surface of a cathode deforms the potential barrier at the surface enough to permit the quantum-mechanical tunnelling of electrons through the potential barrier and into the vacuum. [43]. An energy band diagram depicting barrier deformation by an electric field is shown in Figure 4.1. The applied electric field is F, the workfunction is ϕ_w, the Fermi energy is E_f, and e is the electron charge. The Fermi energy is the maximum allowable energy level occupied by electrons if all of the lower allowable quantum energy levels are filled. The height of the potential barrier between the surface and the vacuum energy level is ϕ_w, and the "width" of the barrier is given by $\phi_w / (eF)$[1]. In the basic theory, the electrons emitted via field emission originate below the Fermi energy level; these low energy electrons are considered "cold". This stands in contrast to the thermionic and photoemission mechanisms for electron emission, where the electrons in the solid must be given enough energy to go *over* the potential barrier. Electrons produced via these mechanisms have energy considerably

[1] for ϕ_w in units of eV, and F in V/m.

greater than the Fermi energy, and are deemed "thermal".

In 1897, R. W. Wood became the first person to describe the phenomenon of "field emission", which he observed during experiments with a discharge tube [44]. Walter Schottky was the first to provide theoretical insight into the process, proposing that the electrons were emitted over a potential barrier at the metal surface reduced by the presence of an external field [45]. In Schottky's model, the peak in the potential barrier is located at a distance z_0 from the metal surface where the image force, $e^2/4z_0^2$, equals the force of the applied field, eF, where e is the electron charge and F is the field strength. These forces lower the workfunction ϕ_w by $\Delta\phi_w = \frac{e^2}{4z_0} + eFz_0$, which becomes $\Delta\phi_w = e\sqrt{eF}$ by eliminating z_0 ($= \sqrt{e/4F}$). Within the framework of this model, the total reduction of the potential barrier at the surface was assumed to completely describe the mechanism of field emission from cold cathodes, which would require fields on the order of $10^8\, V/cm$ for a workfunction of $4.5\, eV$. However, field emission had already been experimentally observed in metals with fields on the order of $10^6\, V/cm$ [44]. In 1926, R. A. Millikan, C. F. Eyring, and B. S. Gossling observed that temperatures up to 1100 K did not affect field emission currents [46]. In 1928, Millikan and C. C. Lauritsen showed that the observed emission current was exponentially dependent on the applied field [47].

4.1.1 Fowler-Nordheim Theory

Sir Ralph Fowler and Lothar Wolfgang Nordheim obtained the first accurate description of field emission, based on tunneling of electrons through the surface potential barrier, in 1928 [48]. Fowler and Nordheim assumed Fermi-Dirac statistics

for the electron energy distribution in the metal, calculated the number of electrons impinging on the surface from the bulk for each range of energy, and solved the Schrödinger equation to find the fraction of electrons that penetrate the barrier. Upon integrating the product of the number of electrons arriving at the surface from the bulk and the tunneling probability over all energies, they obtained a formula for the current density given by

$$J = \frac{4\sqrt{\mu\phi_w}}{\mu + \phi_w} \frac{e^3 F^2}{8\pi h \phi_w} exp\left(-\frac{8\pi\sqrt{2m}\cdot\phi_w^{\frac{3}{2}}}{3heF}\right), \tag{4.1}$$

where e is the electron charge, h is the Planck constant, μ is the Fermi level relative to the bottom of the conduction band, and ϕ_w is the workfunction. The Fowler-Nordheim theory accurately described the electric field and workfunction dependence of the emission current. Nordheim later refined the theory further to include the potential barrier deformation due to Schottky's image force [49]. This refinement reduced the predicted field strength necessary for the same current density. Furthermore, the prediction of extremely high FE current densities, far greater than those possible with thermionic emission, was one of the significant results of the Fowler-Nordheim theory. This derivation of the current density, accounting for Nordheim's modified potential barrier, is presented in detail in Appendix A.

Much theoretical and experimental work followed the early work of Fowler and Nordheim for one-dimensional planar emission [50, 51, 52, 43, 53, 54]. In more recent years valuable work has been done to clarify discrepancies in field emission theory

stemming primarily from the use of different formalisms [55, 56, 57, 58]. This has provided insight into the complexities associated with accurately understanding the complete physical picture describing what is commonly called electron field emission, and furthering our ability to better understand experimental results by providing less idealized, and consequently more complicated modelling of the cathodes.

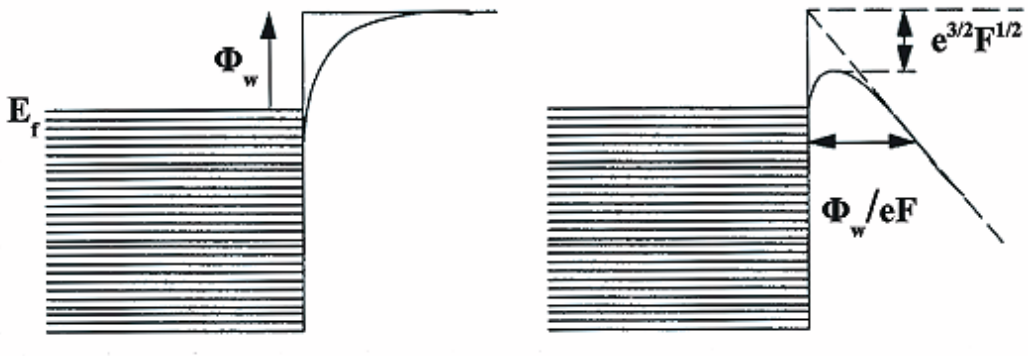

Figure 4.1: Energy diagram for electrons at a metal surface, in the absence of (left) and in the presence of (right) an applied external electric field, F.

A more generalized formalism for the emission current, in terms of the current magnitude [59], is given by

$$I = \lambda A a \phi_w^{-1} F^2 exp\left[-\mu b \phi_w^{3/2}/F\right], \tag{4.2}$$

where ϕ_w is the local workfunction of the emitting surface, F is the external electric field (taken as a positive quantity), λ and μ are generalized correction factors, whose form in a given application depends on the particular assumptions and approximations made about that system. A is the notional area of emission, and a and b are

universal constants given by[2]

$$a \equiv e^3/8\pi h = 1.541434 \times 10^{-6} A \cdot eV \cdot V^{-2}$$

$$b \equiv \frac{8\pi}{3}\left(2m_e\right)^{1/2}/eh = 6.830890 \times 10^9 eV^{-3/2} \cdot V \cdot m^{-1}$$

where e is the elementary positive charge, and m_e is the electron mass.

The 1956 work of Murphy and Good was the first fully satisfactory mathematical analysis of the standard physical assumptions [50], in that it included emission at finite temperatures; prior to then only a zero-temperature approximation had been employed in developing the theory. In their development, they use the correction factors t and v, corresponding to those previously presented as λ and μ respectively (Eqn. 4.2), and introduce the parameter y, such that

$$\lambda \rightarrow t^{-2}(y), \qquad \mu \rightarrow v(y) \tag{4.3}$$

where y, v, and t are as defined in the expanded theoretical derivation in Appendix A. When represented in FN coordinates, Equation 4.2 becomes

$$ln\{I/F^2\} = ln\{\lambda A a \phi_w^{-1}\} - \mu b \phi_w^{3/2}/F, \tag{4.4}$$

and the tangent to this curve is written in terms of F_1 as

$$ln\{I/F_1^2\} = ln\{\lambda_1 A a \phi_w^{-1}\} - \mu_1 b \phi_w^{3/2}/F_1. \tag{4.5}$$

$\lambda_1 (= t^{-2}(y_1))$ and $\mu_1 (= v(y_1))$, the values taken at field F_1, are now equivalently the functions $\lambda (= t^{-2})$ and $\mu (= v)$. The functions $t^{-2}(y)$ and $v(y)$ are called the

[2]In practical field emission contexts only the first two or three significant figures are needed, but the constants in this elementary theory are, in fact, known to an accuracy of about one part in 10^6 [60]. As is evident, these values are in rationalized MKSA units (meaning *M*eters, *K*ilograms, *S*econds, and *A*mperes), which is the system of units this dissertation will endeavor to use.

generalized intercept correction function and the *generalized slope correction function*, respectively, and are sometimes also represented as $r\,(=t^{-2}\,(y))$ and $s\,(=v\,(y))$. In standard FN theory, under typical emission conditions, μ_1 is typically on the order of 1, where λ_1 is typically on the order of 100 [59].

Equation 4.4 provides a functional form which field emission electrons will manifest, establishing the standard for identifying the predominant mechanisms in our electron emission data.

4.1.2 Field Enhancement

The assumption of a planar, or very smooth, surface of the emitter is one of the primary assumptions of the Fowler-Nordheim theory. This assumption is fairly accurate for atomically smooth emitters with a radius of curvature approximately greater than $0.1\,\mu$m, for which the width of the surface potential barrier is much less than the radius of curvature. However, the planar assumption, which reduces the problem to a one-dimensional one, is not valid for field emitters with a radius of curvature around $1-20\,n$m, which approaches the barrier width. Additionally, for the same applied field, the local field at the apex of emitters with small radii of curvature will be larger than that for emitters with larger radii of curvature, consistent with the inverse proportionality of the field to the radius of curvature.

Field Enhancement in electron field emission has been the object of significant recent attention in both theoretical and experimental work, which can be attributed to the important role it plays in the practical implementation of electron field emission. The basic Fowler-Nordheim theory presented earlier is highly idealized from the

perspective of practical application, given its assumption of a uniform electric field F. In practice, the local field at an emission site is extremely difficult to determine, due to field enhancement. In practice, the applied field is a macroscopic field F_M, derived from the applied voltage and the measured distance between the anode and the emitter surface

$$F_M = V/d. \tag{4.6}$$

This macroscopic field, however, can be related to the field at a particular emission site by

$$F = \gamma F_M, \tag{4.7}$$

where γ is a field enhancement factor which is dependent on the geometry at the emission site, and which contributes significantly to the actual emission-igniting field. Incorporating this into Eqs. 4.2 and 4.4, we obtain

$$I = \lambda A a \phi_w^{-1} \gamma^2 F_M^2 exp\left[-\mu b \phi_w^{3/2}/\gamma F_M\right], \tag{4.8}$$

which in Fowler-Nordheim coordinates is then written as

$$ln\left\{I/F_M^2\right\} \;=\; ln\left\{\lambda A a \phi_w^{-1}\gamma^2\right\} - \mu b \phi_w^{3/2}/\gamma F_M \;\equiv\; ln\left\{R_M\right\} + S_M/F_M, \tag{4.9}$$

with Eq. 4.9 defining R_M and S_M as

$$R_M = \frac{\lambda_1 A a \gamma^2}{\phi_w} \quad \text{and} \quad S_M = \frac{-\mu_1 b \phi_w^{3/2}}{\gamma}. \tag{4.10}$$

The quantities $ln\{R_M\}$ and S_M correspond to the intercept and the slope of the tangent to Equation 4.5, taken at the field F_1. The intercept and slope from experimental data, plotted in FN coordinates, provide estimates of R_M and S_M. For intercept interpretation, it is better to use the combination $R_M S_M^2$ and the formula

$$A = \frac{R_M S_M^2}{ab^2\Gamma}, \tag{4.11}$$

where

$$ab^2 = \frac{7.192494 \times 10^{13} A}{m^2 e V^2}, \tag{4.12}$$

and the *emission-area extraction function* Γ is defined by [59]

$$\Gamma = \lambda \mu^2 \phi_w^2. \tag{4.13}$$

These equations introduce the proportionate significance of the applied macroscopic field F_M and the field enhancement factor γ; arguments similar to Equation 4.7 *et seq.* can, in principle, be applied to voltage-based FN plots by defining $F = \beta V$, where β becomes the *local-field-to-voltage-ratio* (LFVR), and by replacing γ, F_M, R_M, S_M in the above equations (Eqns. 4.8 *et seq.*) with β, V, R_V, S_V, respectively [55]. This will yield

$$I = \lambda A a \phi_w^{-1} \beta^2 V^2 exp\left[-\mu b \phi_w^{3/2}/\beta V\right], \tag{4.14}$$

$$ln\left\{I/V^2\right\} \;=\; ln\left\{\lambda A a \phi_w^{-1}\beta^2\right\} - \mu b \phi_w^{3/2}/\beta V \;\equiv\; ln\left\{R_V\right\} + S_V/V, \tag{4.15}$$

$$R_V = \frac{\lambda_1 A a \beta^2}{\phi_w} \quad \text{and} \quad S_V = \frac{-\mu_1 b \phi_w^{3/2}}{\beta}. \tag{4.16}$$

Equations 4.13 *et seq.*, in conjunction with the appropriate physical assumptions, are the most commonly used in the interpretation of empirical $I - V$ data.

4.1.3 Field Emission from Semiconductors

In comparison to that from metals, field emission from semiconductors, is a highly complicated process. The main factor for this is the variability in carrier concentration in the emitter's bulk. Low carrier concentration can lead to penetration of an

external electric field into the semiconductor for a considerable depth, band bending, and strong thermo- and photo-sensitivity. From the viewpoint of reproducibility a semiconductor emitter is a much more insidious situation because even the preparation process (surface cleaning, sharpening, heating) may lead to irreversible property changes and effects that are hard to identify and reproduce. On the other hand, the study of electron field emission from semiconductors is arguably more enticing than that for metals, because of the potential to find new data on surface properties and behavior of solids in electric fields. A semiconductor potentially offers numerous ways of varying the characteristics of the emission process by controlling the carrier concentration in the emitter bulk, making unique electron devices possible. It appears possible, for instance, to have a limited carrier concentration in the near-surface region of a semiconductor and control the FE process by generating or injecting carriers into this region. The obvious potential for new systems in vacuum electronics from the application of semiconductors as field emitters is aided additionally by the fact that for some semiconductor materials, such as Si, the basic technology of micro- and nano-fabricating complex structures has been developed.

Morgulis [61] and Stratton [62, 63] proposed a qualitative theory of the field emission process from semiconductors close to 60 years ago. Known as the Morgulis-Stratton model, it is based again on a zero current approximation, which implies thermodynamic equilibrium of the electron energy distribution. This approximation is acceptable when the emission current is not very strong, and can adequately describe experimental results for FE from some semiconductors for relatively small currents.

Outside of this regime, however, existing experimental data does not agree with the general trend of the current-voltage characteristics predicted by the Morgulis-Stratton model [64]. The theory does however describe the linear increase in the natural logarithm of the current in the small current region with the applied bias. It assumes that the electron gas is degenerate due to penetration of the electric field into the emitter near the surface, increasing the free electron concentration near the surface. The theory also assumes that the tunneling transmission coefficient is small. Calculation of the emission current density would in this case follow the Fowler-Nordheim derivation.

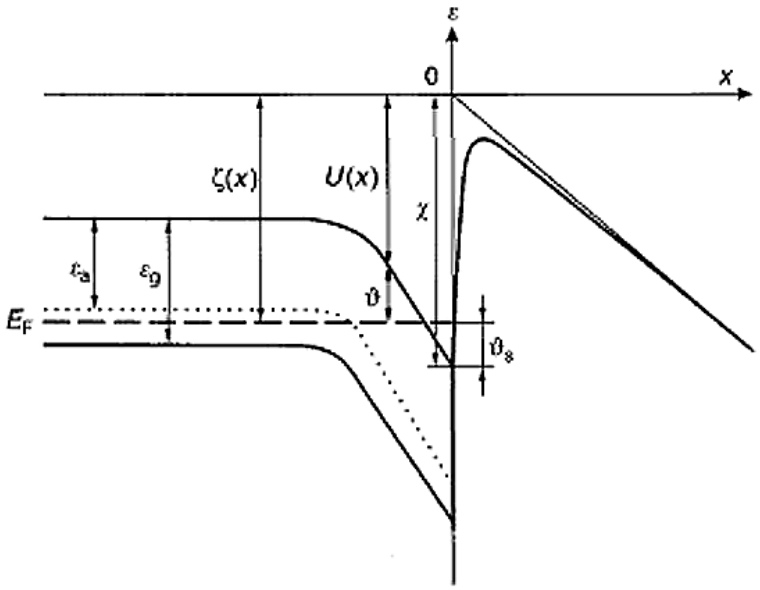

Figure 4.2: Energy Diagram of the near-surface region of a semiconductor in the "weak field" approximation[3]. (ϑ – degeneration parameter; ϑ_s – degeneration parameter near the surface; χ – electron affinity; $U(x)$ – energy at the bottom of the conduction band; ζ – level of electrochemical potential; ε_a – an example mid-band activation energy; ε_g – energy of the band gap. [9])

Contrary to expectations, attempts to account for the effect of the semiconduc-

[3]region 1 of the current-voltage regimes, page 52

tor's energy band structure on the electron emission process, including corrections for the effective mass as well as the surface states, have failed to yield a unified predictive technique for the current-voltage characteristics of field emission from semiconductors [65]. Theorists have predicted, however, that electron field emission from semiconductors of both n- and p-type will generally fall into five regimes of distinguishable current-voltage characteristics, each of which may or may not be manifest in a given semiconductor system:

1. The linear Fowler-Nordheim region, at low applied field
2. A first saturation region, $J \sim \mu_n F_M exp\left(-\varepsilon_t / k_B T\right)$;
3. A second saturation region, $J \sim \mu_n \left(F_M^2 / L\right) exp\left(-\varepsilon_t / k_B T\right)$;
4. A region of rapid current increase;
5. A third saturation region, $J \sim \mu_n \left(F_M^2 / L\right)$

where F_M is the applied electric field at the surface, μ_n is the electron mobility, and ε_t is the activation energy of deep trap states near the surface, and L is the height of the emitter.

Although Morgulis-Stratton theory cannot be applied to field electron emission from semiconductors with low equilibrium concentrations of conduction band electrons in high fields, qualitatively it is in fair agreement with experiment for most semiconductors in low electric fields (region 1 of the current-voltage characteristic), which also most closely follows the Fowler-Nordheim prediction.

4.2 FE Measurement System

4.2.1 Setup Design

Field emission characteristics of grown BN films were determined via emission testing in the 8 inch diameter six-way cross stainless steel ultra-high vacuum (UHV) chamber shown in Figure 4.3. The chamber is capable of achieving a vacuum of 10^{-7} torr in less than 24 hours without the use of heater tapes for bakeout, with base pressures in the high 10^{-9} torr range achievable. An Alcatel^{TM} Turbomolecular Pump backed by an Alcatel^{TM} Roughing Pump were used to establish the vacuum. Any tools that would potentially contact components or samples destined for the UHV environment were subjected to a series of ultrasonic baths (trichloroethylene, acetone, and isopropyl alcohol) to reduce risks of contamination. Samples were handled carefully, and were stored in evacuated dessicators when not under measurement. Emission testing was performed at a variety of pressures, depending on the experiment being run. Vacuum experiments were typically performed at operating pressures in the 10^{-8} torr range. Figure 4.4 shows the emission test sample measurement configuration within the UHV chamber. The BN films were offset from a phosphor-coated Indium Tin Oxide (ITO) collection anode using strands of 25 μm glass fiber optic. The ITO anode was 0.0625 in. $\times$ 1.25 in., centered (with major axes aligned) on a 0.7 in. $\times$ 1.5 in. glass slide. The 0.0625 in. $\times$ 0.4 in. phosphor was also centered co-axially with the ITO and the glass slide. A bare copper lead connected to the ITO anode via an Indium contact, and a bare copper lead attached to the BN thin film substrate, also via an Indium contact, provided the electrical connec-

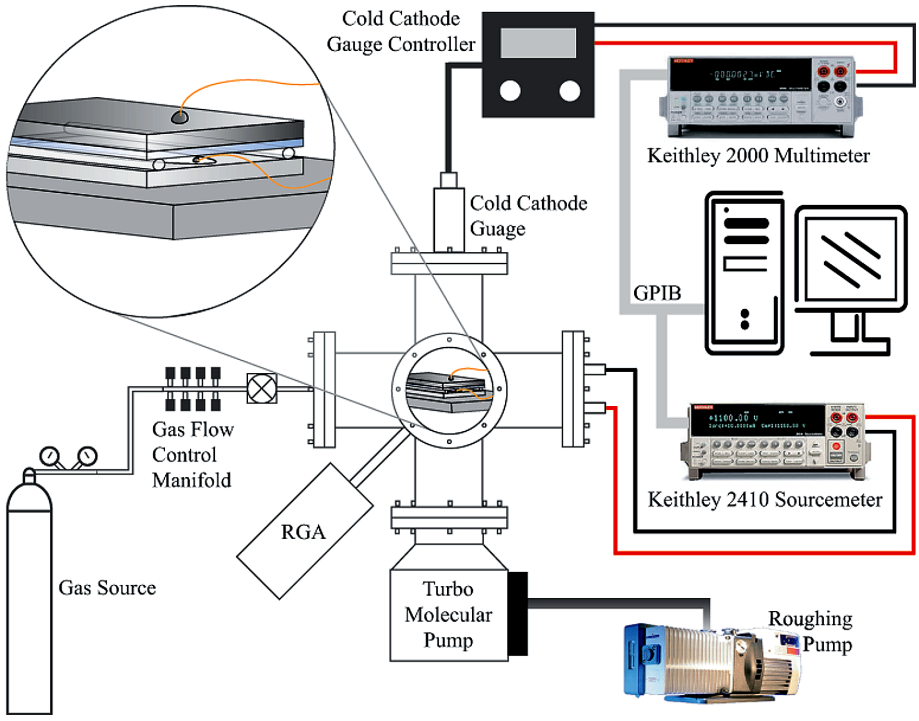

(a)

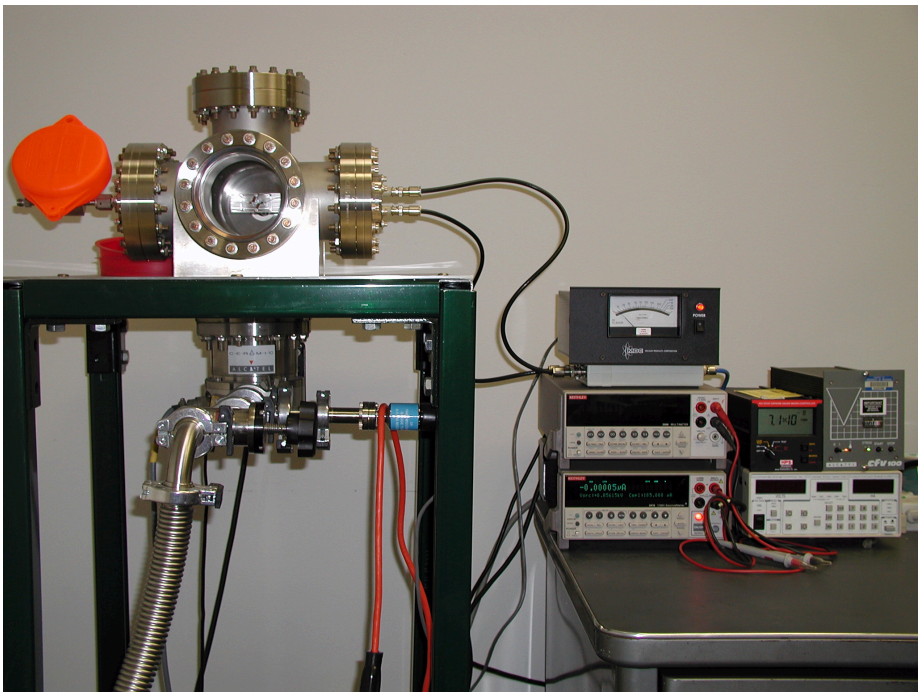

(b)

Figure 4.3: Field Emission Measurement Setup. (a) depicts the configuration of the equipment in the field emission experiment. (b) is a photograph of the equipment in the field emission experiment.

tions for the applied voltage as well as the current readings through a UHV electrical feedthrough to the measurement equipment. 0.5 in. $\times$ 0.125 in. Vespel^{TM} clamps, mounted to the stainless steel anode holder on opposite sides, held the sample/glass spacers/anode assembly in place, and provided a planar alignment (Figure 4.4). A Stanford Research Systems Model RGA200^{TM} Residual Gas Analyzer, also mounted to the UHV chamber, provided data scans of the partial pressures inside the chamber during measurements.

During the various electron emission measurements, the voltage bias between the BN film and the collection anode was deliberately gradually increased, in order to approach the emission threshold as slowly as possible, ostensibly contributing to the length of time required to collect data. The emission current was monitored using a Keithley 2410 SourceMeter®, which both sourced the voltage and read the current. It was connected to the experiment under vacuum through a UHV electrical feedthrough. The copper leads from the sample are connected to the feedthrough terminals internal to the UHV chamber. The field emission measurement was carried out in an electrically isolated (floating) closed loop arrangement, as seen in Figure 4.3(a). A series of voltage sweeps were performed *in vacuo*, in Xenon gas, in Oxygen gas, and in Water Vapor, to measure threshold field and repeatability in environments of particular interest for space applications. The gases were introduced into the chamber via a gas feedthrough, controlled using a custom-made, manually controlled gas manifold. Partial pressures were monitored using the SRS RGA200^{TM}, in conjunction with a cold cathode pressure guage. In addition, measurements over

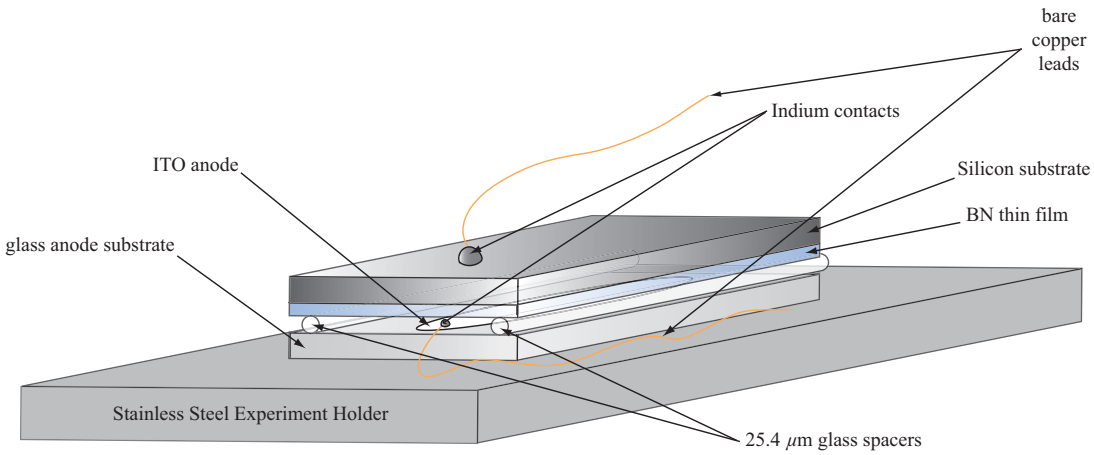

(a)

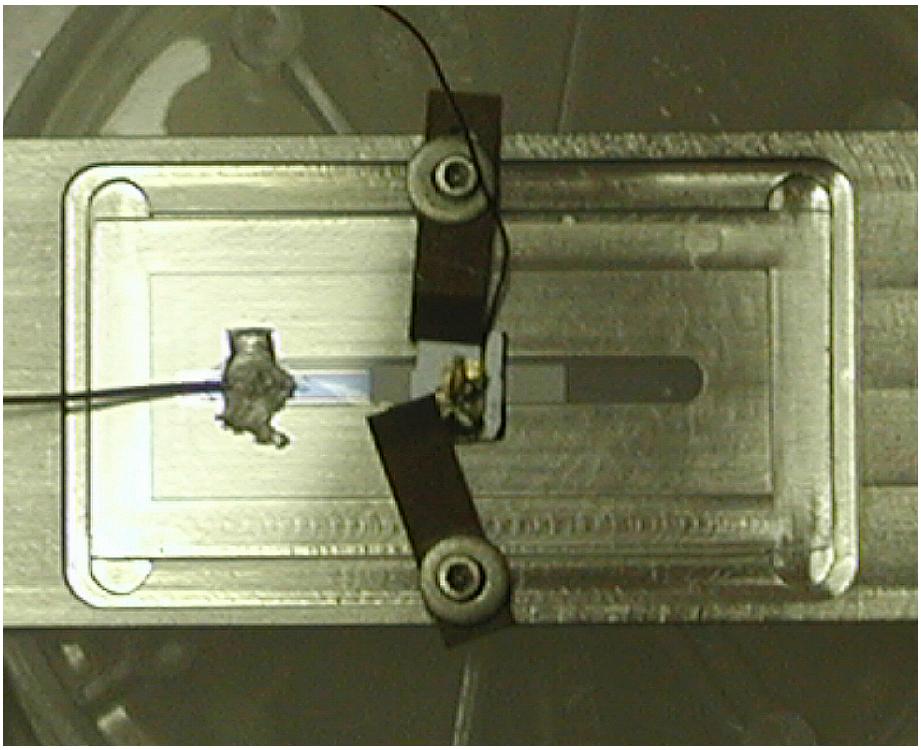

(b)

Figure 4.4: Field emission measurement sample configuration. (a) is a depiction of the configuration of BN sample under measurement in UHV chamber. (b) is a photograph of the configuration of BN sample under measurement in UHV chamber.

time at constant pressures *in vacuo*, in Xenon gas, in Oxygen gas, and in Water Vapor, were also performed to measure emission stability of the films. Pre- and post-exposure effects were measured as well for the Xe and O_2 environments.

4.2.2 LabVIEW™ Data Acquisition

During the course of a measurement, the real-time vacuum pressure data, together with the applied voltage and measured current values, were collected on a computer via a GPIB interface, using National Instruments LabVIEW™ virtual instrumentation software, which also controlled the start and stop of the voltage "source" and current "sense" measurement cycle, voltage range, voltage step increment, and time step in the measurement. I am greatly indebted to Professor B. Gilchrist, Dr. D. Morris, and C. Deline for their invaluable contributions in the creation and modification of LabVIEW™ software necessary for these studies.

4.3 FE Experiments

A series of voltage sweeps were performed *in vacuo*, in Xenon gas environment, in an Oxygen gas environment, and in Water Vapor, to measure threshold field and repeatability. Measurements over time at constant pressure were also performed in these same environments to measure stability. Pre- and post-exposure effects were observed as well for the measurements in Xe and O_2 environments.

The system used for the measurements presented here was the result of some less successful earlier attempts with equipment that did not account for the necessary stability control in the voltage source, nor the need for patience in approaching the

emission threshold in very small increments from below, both in time as well as in voltage. These goals were achieved with the use of the Keithley SourceMeter® Model 2410, which combines a precise, low-noise, highly stable DC power supply with a low-noise, highly repeatable, high-impedance multimeter. It has 0.012% basic accuracy with 5½-digit resolution. At 5½ digits, the SourceMeter® delivers 520 readings/second over the IEEE-488 (GPIB) bus. At 4½ digits, it can read up to 2000 readings/second into its internal buffer. The unit can source voltage from 5 μV to 1100 V, and measure voltage from 1 μV to 1100 V. Likewise, it can source current from 50 pA to 1.05 A, and measure current from 10 pA to 1.055 A. In the 1000 V range setting which was used for our measurements, the unit had a 50 mV source resolution with a source accuracy of 0.02%, and a metering resolution of 10 mV with a measurement accuracy of 0.015%. Current was measured with the SourceMeter® configured to read in the 1.00000 mA range, with a default measurement resolution of 10 nA at a measurement accuracy of 0.027%.

4.3.1 Emission Threshold Measurement

The graph in Figure 4.5 was generated from data on sample SN124, measured *in vacuo* at a pressure of 7×10^{-6} torr. The sourcing and metering was done and recorded manually, without the benefit the virtual instrumentation system. The readings were taken approximately every 5 minutes, giving the digital readout a chance to stabilize at each step, which was measured at voltage increments of 1 V, until ignition at $\sim$2.75 V/μm, after which the step was increased to 10 V. Measurements were taken up through 240 V. Figure 4.6 shows the data graphed in voltage-based Fowler-

Nordheim coordinates (see Eq. 4.15). A least-squares linear fit of the data yields a coefficient of fit determination value of $R^2 = 0.9923$, for an intercept value of $ln\{R_V\} = -13.855$, and a slope of $S_V = -21.543\,V$, which manifests the predicted linear relationship for field emission. The results of a second field emission threshold

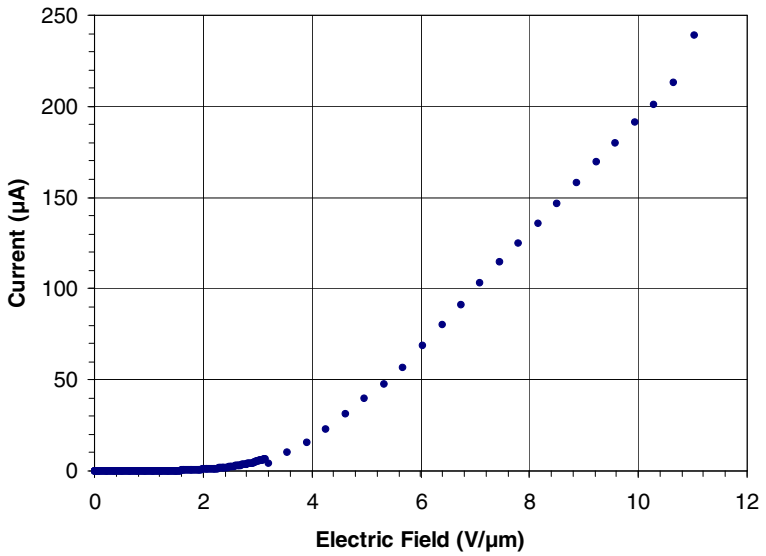

Figure 4.5: Electron emission current vs. electric field measurement of cBN showing emission threshold of $\sim$2.75 V/μm, in 7×10^{-6} torr vacuum [8].

measurement on SN124 (Figure 4.7), again measured manually, revealed a lowering of the threshold to $\sim$0.5 V/μm at a pressure which ranged from slightly above 2×10^{-7} torr to slightly below, over the course of the measurement. Again, the readings were taken approximately every 5 minutes, at voltage increments of 1 V. Ignition occurred unexpectedly, with the current peaking at $\sim$600 μA, at which point we observed the current extinction for the first time in our measurements. A third measurement (Figure 4.8) on SN124 over the same voltage range in increments of 1 V at effectively the same pressure ($\sim1.7\times10^{-7}$ torr) confirmed the extinction of emission at the previous threshold field value. A fourth and final sweep measurement Figure 4.9)

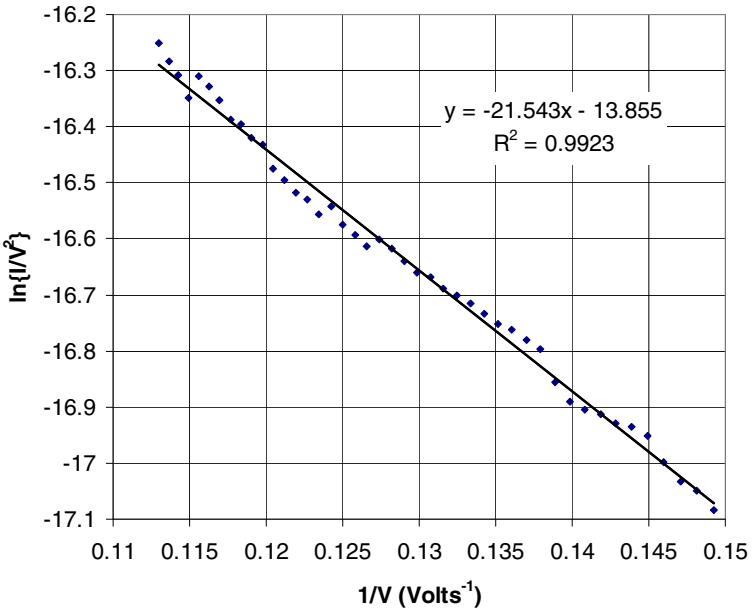

Figure 4.6: Fowler-Nordheim plot of cBN electron emission threshold measurement, with regression fit overlay [8].

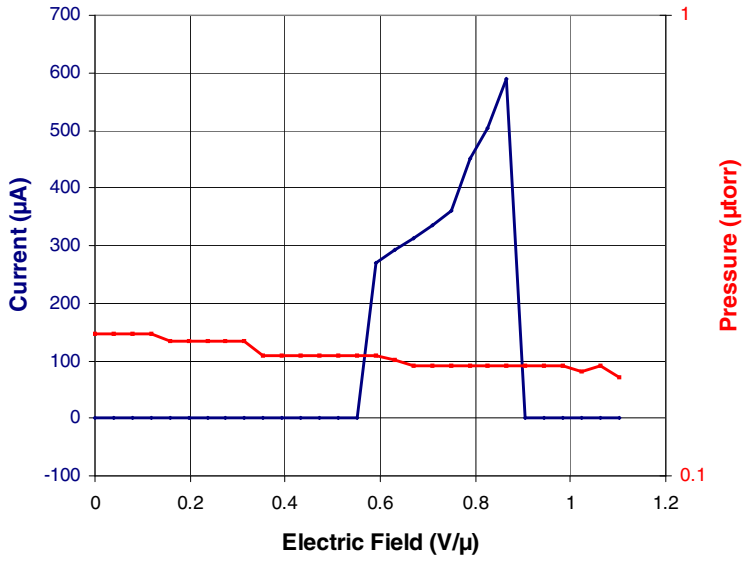

Figure 4.7: Second cBN electron emission threshold measurement on SN124, exhibiting threshold decrease to $\sim$0.5 V/μm before emission extinction

was performed until emission was again detected, albeit at a much lower current value, at an electric field threshold of $\sim$19.7 V/μm, corresponding to an applied

voltage of ∼500 V.

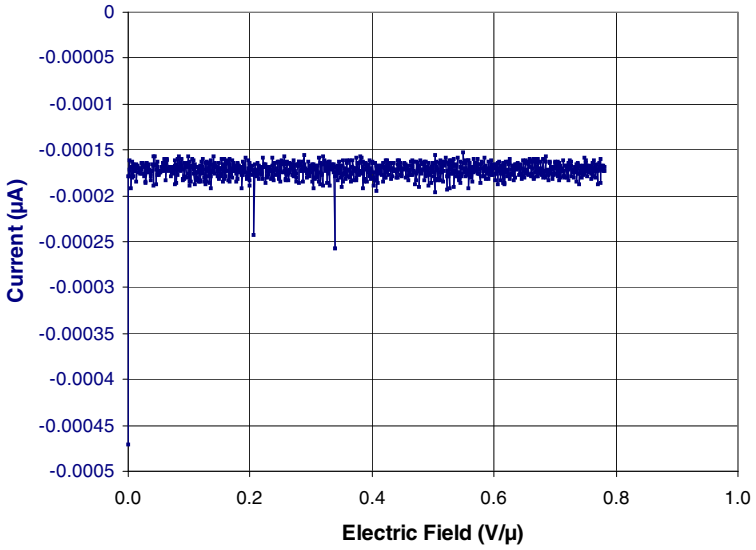

Figure 4.8: Third *c*BN electron emission threshold measurement on SN124 - emission extinction confirmation. The zero-valued current reading is in the noise regime of the instrument.

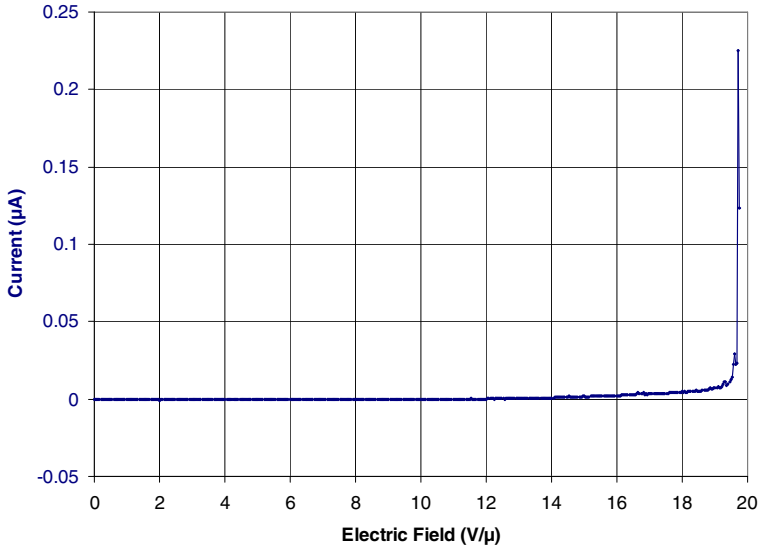

Figure 4.9: Fourth *c*BN electron emission threshold measurement on SN124, showing increase in emission threshold to ∼19.7 V/μm

The demonstrated potential for a low threshold electron emission field, as well

as for the shift and extinction of an emission threshold is indicative of the transient nature of the mechanisms affecting emission. The decision is made at this point to place an upper current limit on subsequent measurements, in efforts to preclude the extinction of emission at a particular threshold in subsequent measurements, where the intent is to study reliability and repeatability of emission.

4.3.2 Sweep Measurements

Subsequent measurements utilized the LabVIEW^{TM} virtual-instrumentation-based experiment control and data collection.

In Vacuo

The graphs in Figure 4.10 are of voltage sweeps on SN124b, a separate sample from the same *as-grown* film. The measurement system was configured to limit the current flow through the closed circuit to a maximum of $10\,\mu$A. The voltage was swept from 0 – 860 V, in increments of 0.25 V, where the source-to-read time interval was 15 seconds. Three sweeps were taken at effectively the same pressure: first, at $\sim 1.15 \times 10^{-2}$ μtorr (green); second, at $\sim 1.25 \times 10^{-2}$ μtorr (blue); thirdly, $\sim 1.52 \times 10^{-2}$ μtorr (red). Although the pressures are of the same order of magnitude, the emission threshold appears to *decrease* with increased time of vacuum exposure, which seems consistent with the decrease of a emission-prohibitive adsorbate on the sample surface with longer exposure to the vacuum. The emission did not extinguish with repeated sweeps, which served to provide a baseline for subsequent similar measurements in different gas environments.

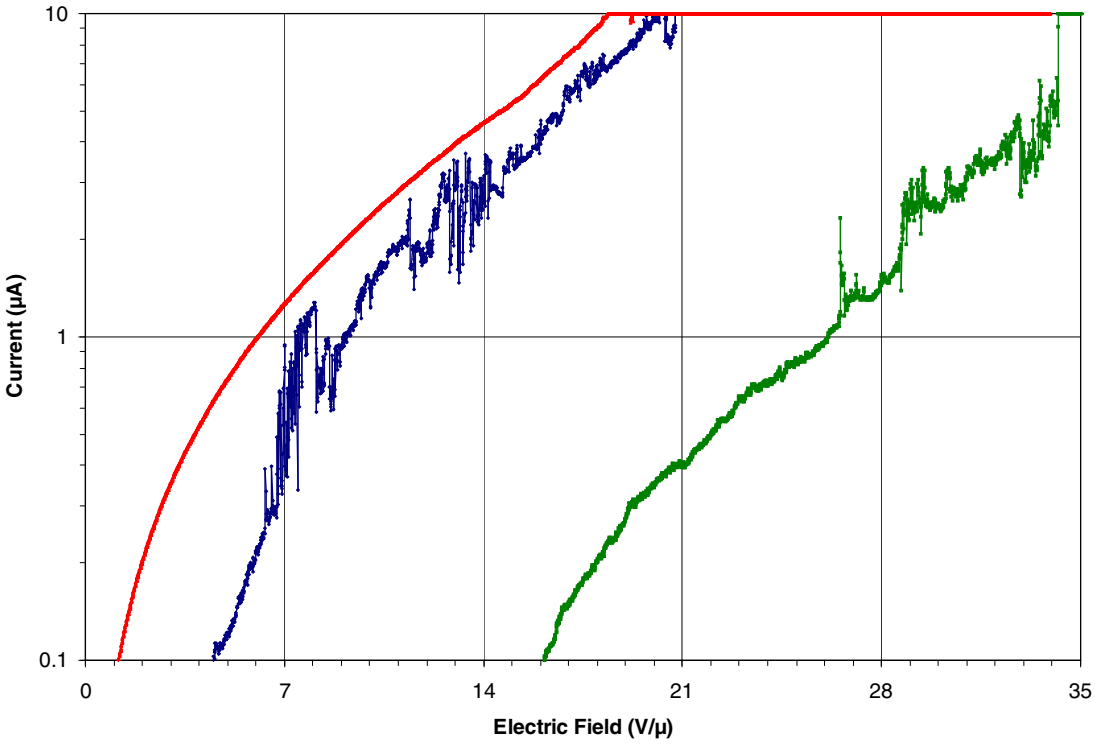

Figure 4.10: cBN electron field emission voltage sweep measurement in UHV at various residual gas pressures: at $\sim 1.15 \times 10^{-2}\,\mu$torr (green), $\sim 1.25 \times 10^{-2}\,\mu$torr (blue), and $\sim 1.52 \times 10^{-2}\,\mu$torr (red)

Oxygen Gas

Voltage sweep measurements were next made on SN124b (Figure 4.11), where now 4-9s purity O_2 gas is introduced into the FE Chamber, the flow rate was stabilized primarily with the gas tank flow regulator, through the custom gas manifold. The partial pressure was monitored via the RGA200, and recorded through the RS-232 serial output, captured through a Keithly Model 2000 Digital Multimeter, and shunted into the LabVIEW^{TM} data acquisition system. Four sweeps were performed (see Figure 4.11), all of the same order of magnitude. Three were at $\sim 1.14\,\mu$torr; first the black curve, then the red, and then the green. The last sweep measurement

is the blue curve, taken at $\sim$1.35 μtorr. Here, the emission thresholds appear to be decreasing with each new sweep. This again supports the observation that the desorption of adsorbates on the emission surface with increasing exposure to the vacuum plays a role in the data observed thus far.

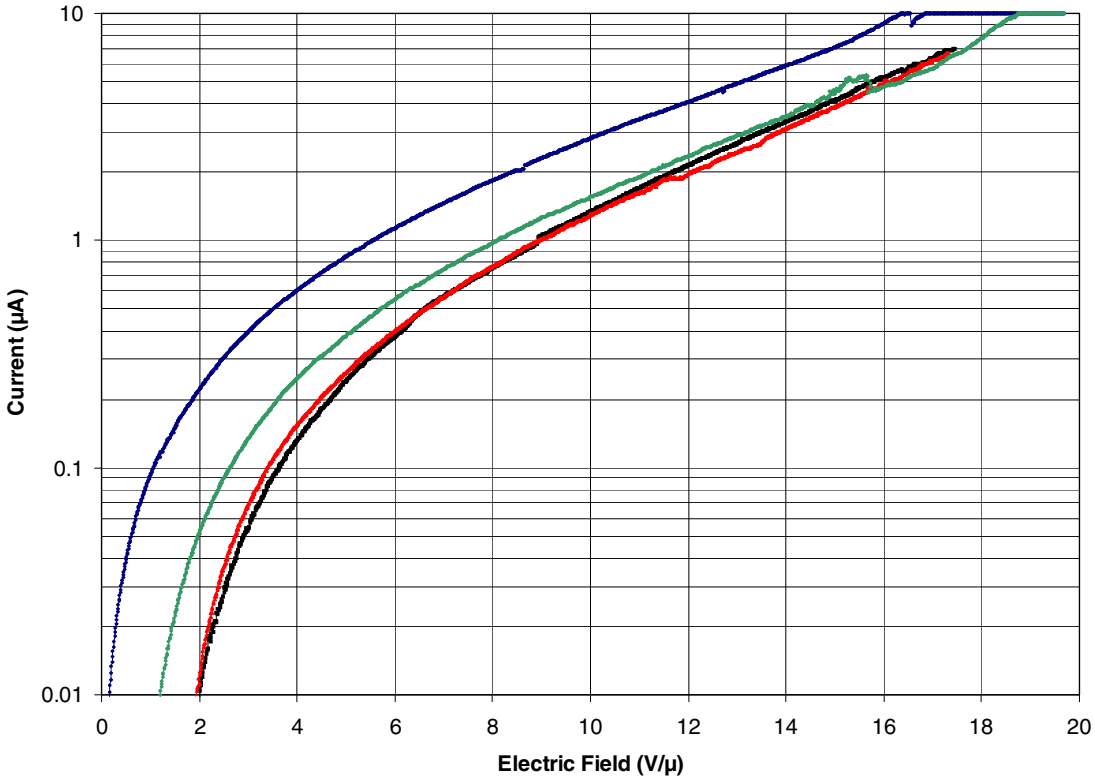

Figure 4.11: cBN electron field emission voltage sweep measurement in O_2 gas at various partial pressures: at $\sim$1.35 μtorr (blue) and $\sim$1.14 μtorr (black, red, and green) [10].

Xenon Gas

One voltage sweep measurement was made of SN134, in a partial pressure of Xenon gas of $\sim$1.3 μtorr, where an emission threshold of $\sim$0.9 V/μm was observed. The noise in the data was also noted.

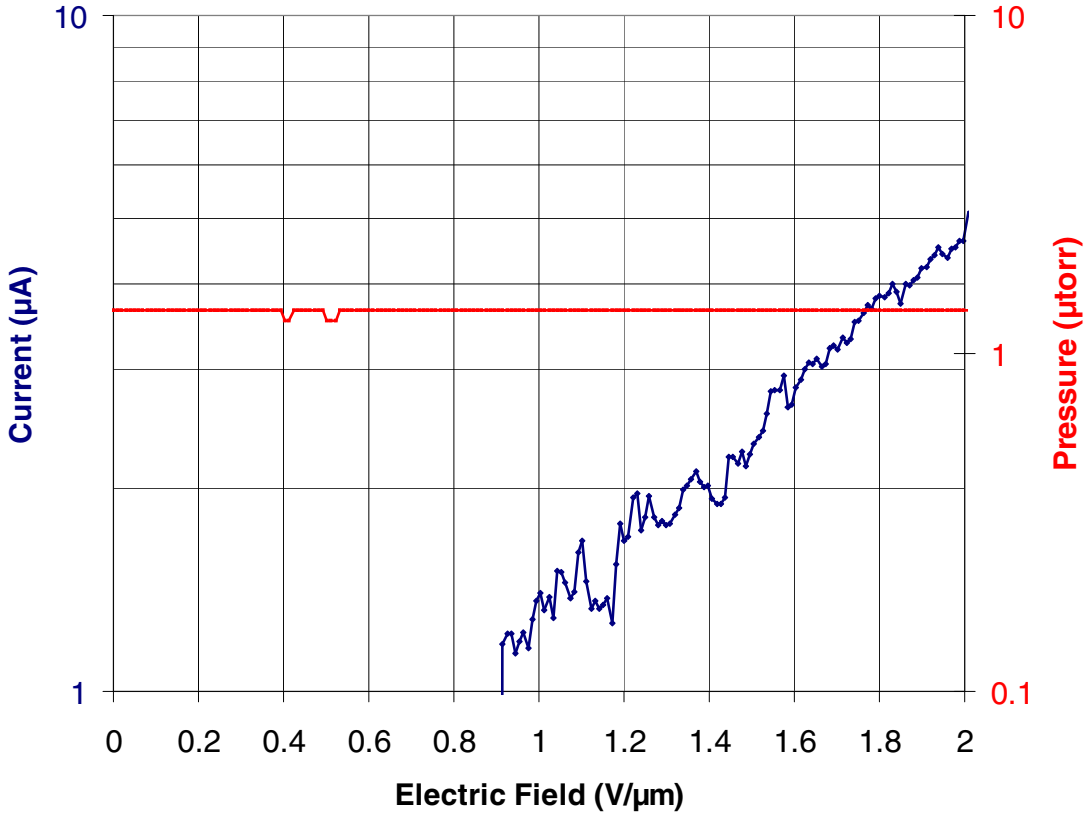

Figure 4.12: cBN electron field emission voltage sweep measurement in Xe gas at a partial pressure of $\sim$1.3 μtorr, exhibiting an emission threshold of $\sim$0.9 V/μm [10].

Water Vapor

A water vapor source was constructed from a glass bottle, which was sanitized, filled with deionized water, and attached to the gas line feedthrough into the FE chamber via the custom manifold. A vapor pressure of $\sim$1.47 μtorr was established and monitored, and allowed to stabilize for 6 hours before measurement began. The results were dramatic (Figure 4.13), in that emission from the film appears to be suppressed completely until a sudden emission drives the current to the system limit. As an environment, water vapor appears to have had the most dramatic effect in

suppressing the ignition of field emission, even at low fields.

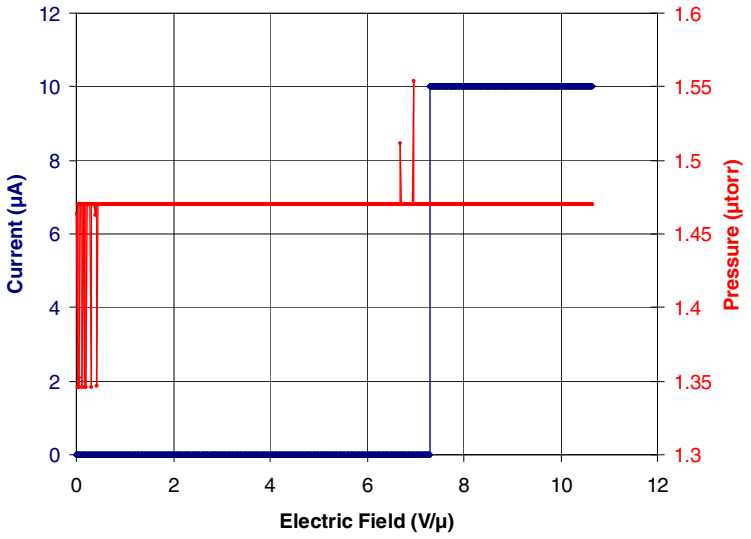

Figure 4.13: cBN electron field emission voltage sweep measurement in water vapor at $\sim$ 1.47 μtorr.

4.3.3 Time Dependence Measurements

Field emission measurements were taken on films, where a fixed macroscopic field was applied, and emission was observed for an extended period of time. In some cases, pressure was also kept constant, to monitor any degradation over time. Other measurements were made where a partial pressure of a gas was applied for a time, then removed, and the emission response was recorded for some time post-exposure.

In Vacuo

Figure 4.14 displays the data from a time measurement of SN134, where the chamber is evacuated to $\sim$0.07 μtorr, and emission is monitored for almost four hours. What is notable is the instability in the chamber pressure. Although the spread is less than 10% – $(0.077 - 0.072)/0.073 \times 100\% \approx 7\,\%$ – the emission appears

to respond to the decrease in pressure, as time lapses. This again gives credence to the concept of impurities such as adsorbates on the emission surfaces needing removal to stabilize the emission current. In this case, the emission eventually stabilizes at $\sim 1.2\,\mu$A.

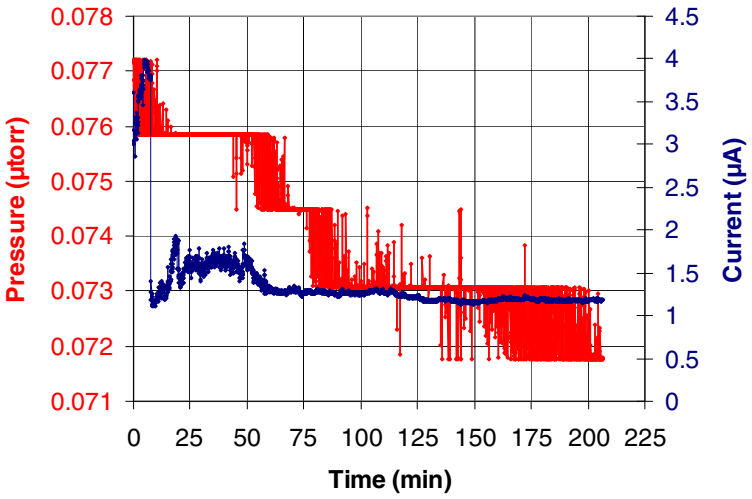

Figure 4.14: *c*BN Electron Field Emission at constant macroscopic field, 2.5 V/μm, and base vacuum, $\sim 0.07\,\mu$torr.

Xe Gas

Two time dependence measurements were performed on SN134 in Xe gas: the first (Figure 4.15) at a constant field of 2.7 V/ μm, and constant pressure of $\sim 1\,\mu$torr, for just over 4 hours. The second (Figure 4.16) is performed at a constant field of 2.5 V/ μm, and exposed to Xe gas at a pressure of $\sim 1\,\mu$torr for a period of ~ 3 hours, after which the chamber is pumped down to a base pressure of $\sim 0.07\,\mu$torr, where it remains for just over 9 hours, for a total 12 hour measurement time.

Figure 4.15 again suggests some sort of adsorbate diffusion mechanism on the emission surface, which impedes emission twice during the four hour period. For the

subsequent longer measurement, the emission appears to remain fairly stable, even through the exposure and evacuation of the Xe gas. Given that both Xe and cBN are inert, it is reasonable to expect a surface unencumbered by adsorbates, would emit in a stable fashion.

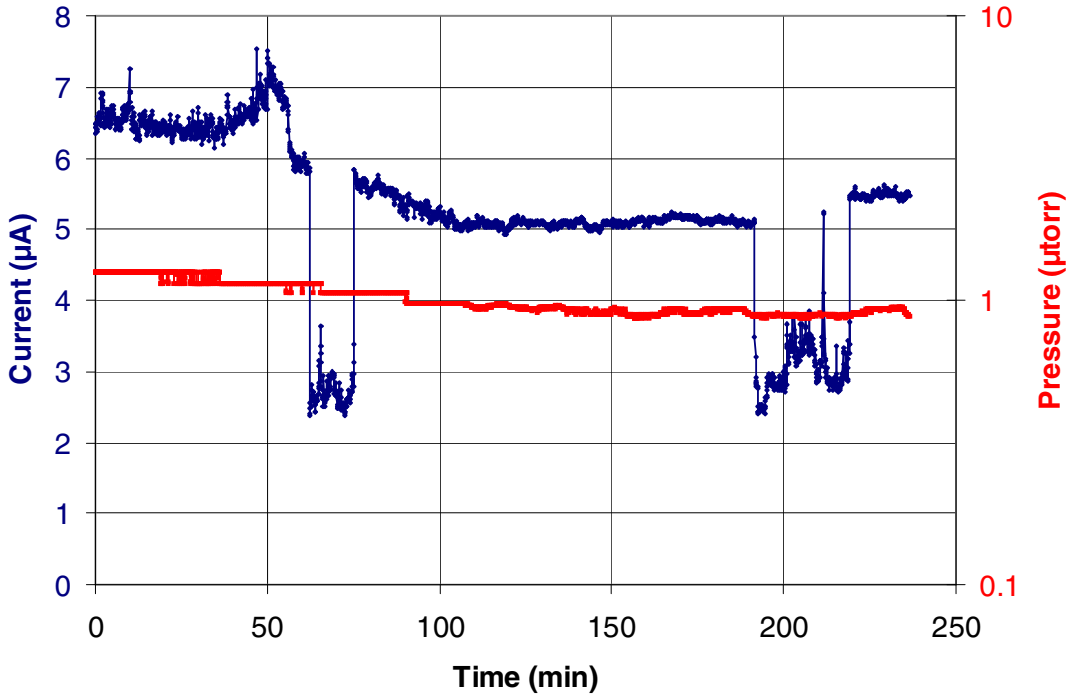

Figure 4.15: *c*BN electron field emission at constant macroscopic field of 2.7 V/ μm and in Xe gas, at a partial pressure of $\sim$ 1.0 μtorr.

Oxygen

The Oxygen gas time measurement is performed in two parts. The graphs in Figures 4.17 and 4.18 show the same results, where Figure 4.18 is the exploded view of Figure 4.17. In this measurement, the constant field is set at 5.22 V/ μm, and the pressure is initially at the base level (here, $\sim$0.0009 μtorr). After $\sim$30 min, the oxygen is adjusted to $\sim$1.0 μtorr, albeit in an unstable fashion, such that it "spikes" twice

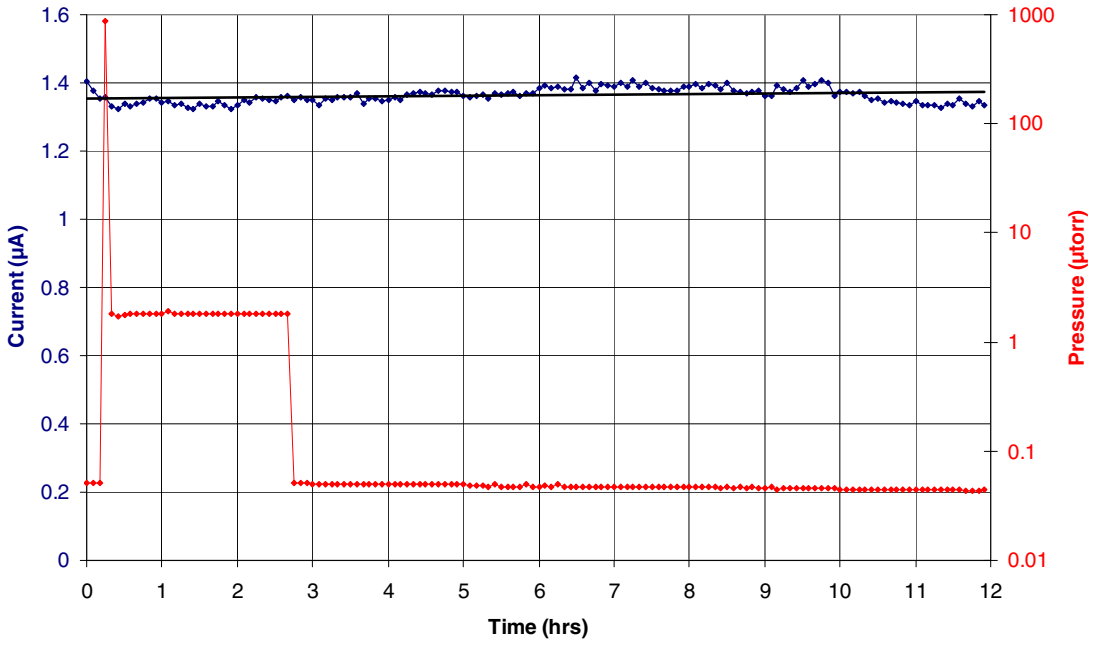

Figure 4.16: cBN electron field emission at constant macroscopic field of 2.5 V/ μm and in Xe gas, at a partial pressure of $\sim$ 1.83 μtorr [10].

during the measurement; one for a period of $\sim$3 min at $\sim$1.0 $m$torr, then back down under $\sim$1 μtorr, then again very briefly (for about 1 minute) to $\sim$0.2 $m$torr before returning finally to the prescribed 1 μtorr level. The exploded view in particular displays the apparent response in suppression of emission current corresponding to the first (unintended) spike in the O_2 gas.

A 16 hour time measurement of emission in O_2 gas (Figure 4.19), where the measurement begins with the O_2 pressure set at $\sim$1.0 μtorr, where it remains for the first 7 hours of the experiment, at which point the O_2 gas is evacuated, taking the chamber back to a base pressure of $\sim$0.01 μtorr. Very clearly, after a period of about 30 minutes from the shut off of the oxygen, the emission increases almost 88%, and eventually stabilized down to about 28% of the emission current value when subject

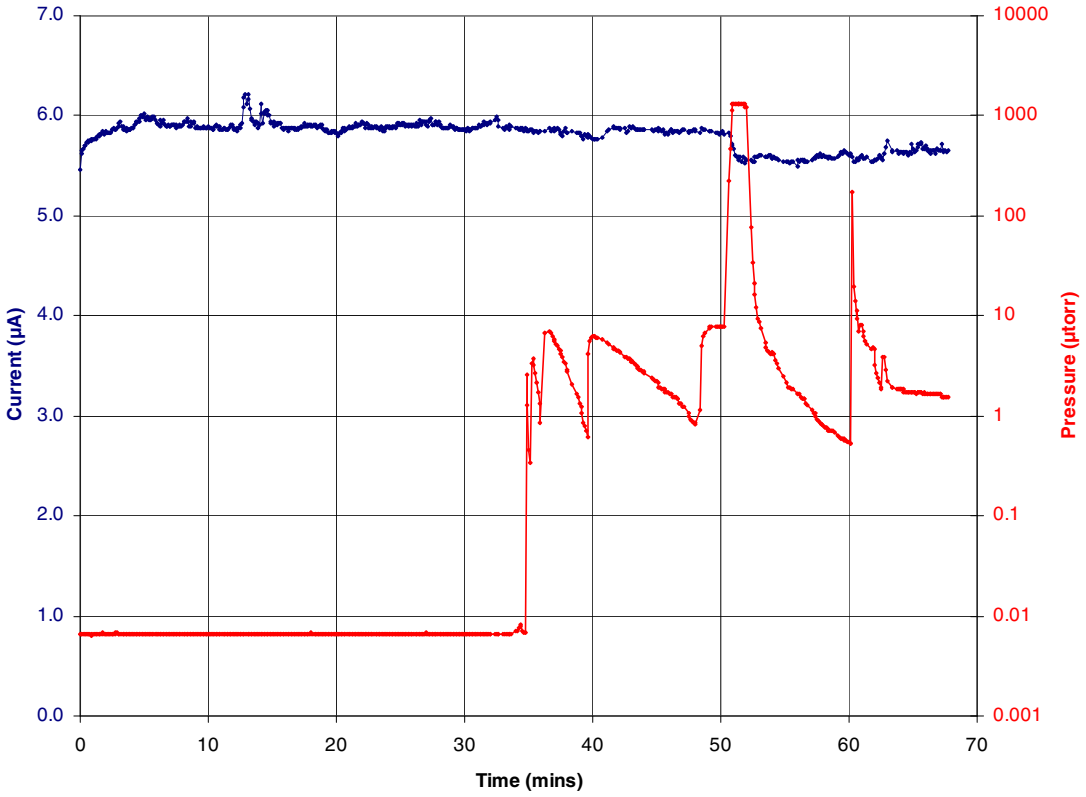

Figure 4.17: cBN electron field emission over time at constant macroscopic field of 5.22 V/μm and in O_2 gas.

to the oxygen environment. This demonstrates the recovery potential of this material after extended exposure to oxygen gas.

The delay in the recovery of emission to pre-oxygen exposure levels may be attributed to the desorption of multiple layers of emission-inhibiting adsorbates. One of the characteristics of the cBN films grown using the technique introduced in Chapter II is the propensity for the deficiency of nitrogen ions during growth, making the films slightly non-stoichiometric and p-type [26]. This condition would make available boron ions for reaction with oxygen, potentially creating a boron oxide adsorbate at the emission surface and inhibiting emission.

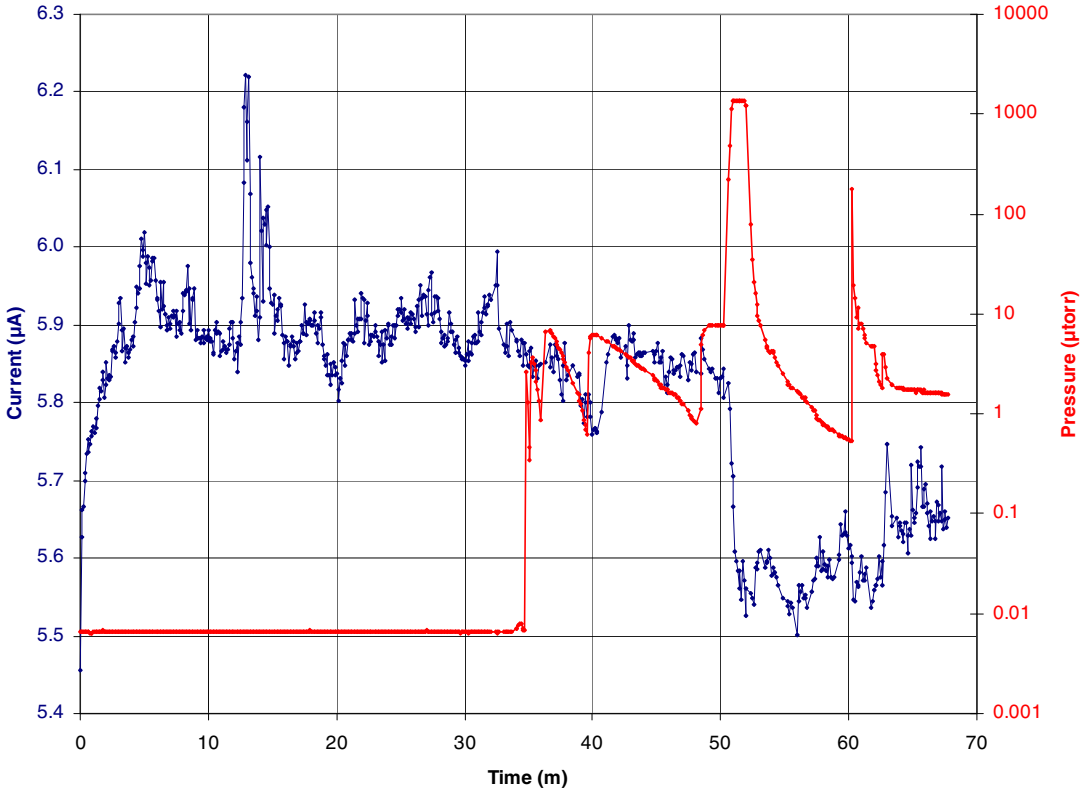

Figure 4.18: cBN electron field emission over time at constant macroscopic field of 5.22 V/μm and in O_2 gas, with an exploded view of the current scale.

Water Vapor

Figures 4.20 and 4.21 represent two measurements of emission from cBN films in a water vapor environment. The vapor pressure for these measurements was by far the most difficult to stabilise. Figure 4.20 presents the result of a 20 hour test, where the film was exposed initially to a pressure of $\sim$4 - 5 μtorr for the first 3.5 hours of the measurement, at which point the chamber is pumped down to base pressure at $\sim$0.08 μtorr. The emission appears to respond with a depression of maybe 10% in the first hour or so of the water vapor exposure. However the exposure continues for

an additional two hours before it is removed, and the level of emission to which the film stabilizes after the first hour basically remains the same after the water vapor is evacuated from the chamber, and for the duration of the experiment, with possibly some very gradual degradation in current over the remainder of the 20 hours of less than 10%.

The final measurement, presented in Figures 4.22 and 4.23, is a best effort to repeat the previous water vapor time measurement, under the identical conditions. In this attempt, the water vapor pressure is raised to $\sim 9\,\mu$torr, but after an hour at base pressure ($\sim 0.02\,\mu$torr). The vapor pressure is maintained at that level for a total of $\sim$3.5 hours before being shut off for the remainder of the 10 hour long measurement. The emission current seems to track the vapor pressure in its rise and fall, but slightly. There appears to be $\sim$5% rise in the current between the initial start of the experiment, and the turning on of the water vapor one hour later. When the vapor is removed, the emission apparently decays $\sim$10% from its value before shut off, which is ultimately $\sim$5.5% below the emission value at $t = 0$.

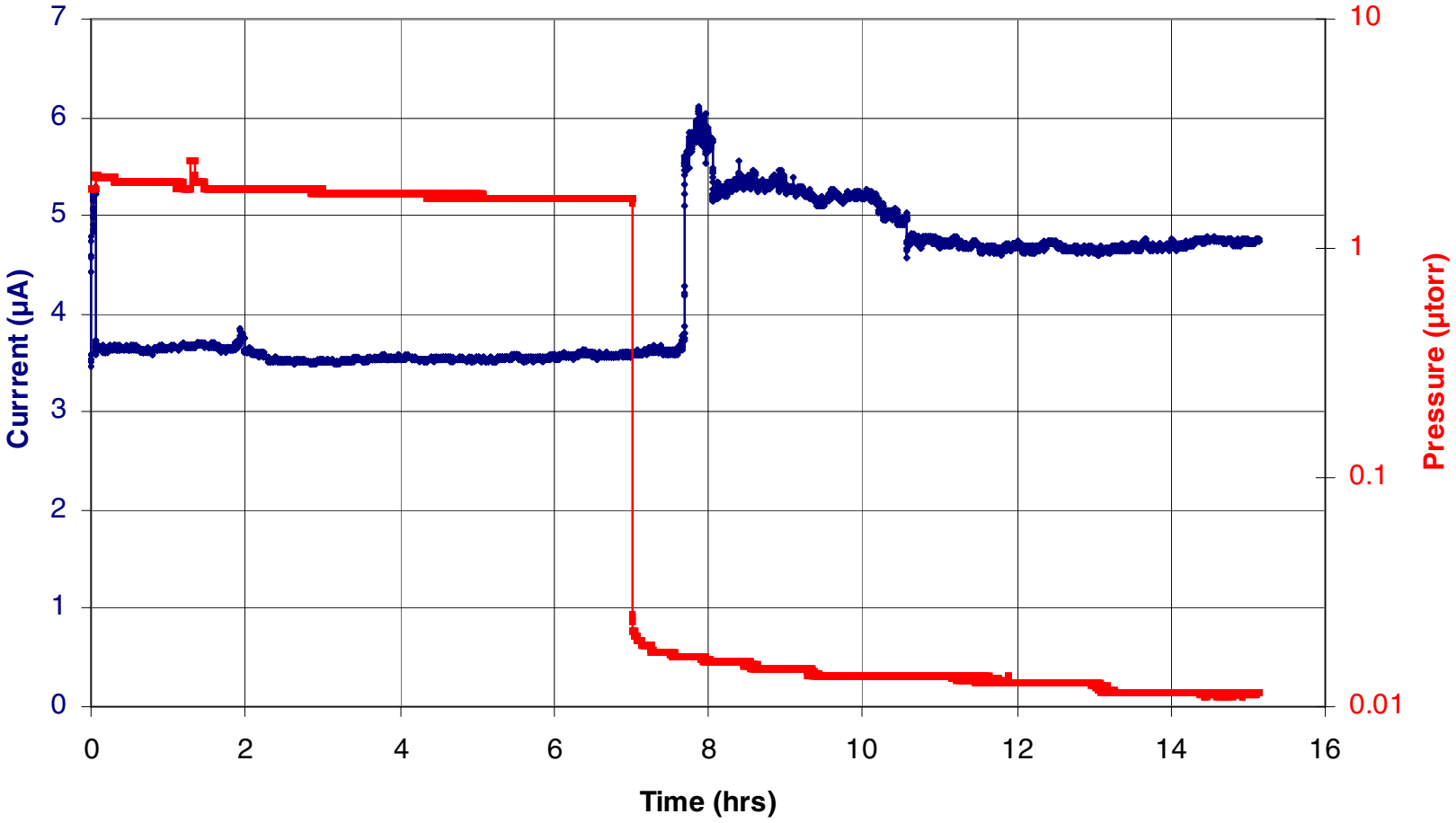

Figure 4.19: cBN electron field emission recovery at constant macroscopic field of 5.22 V/μm in O_2 gas [10].

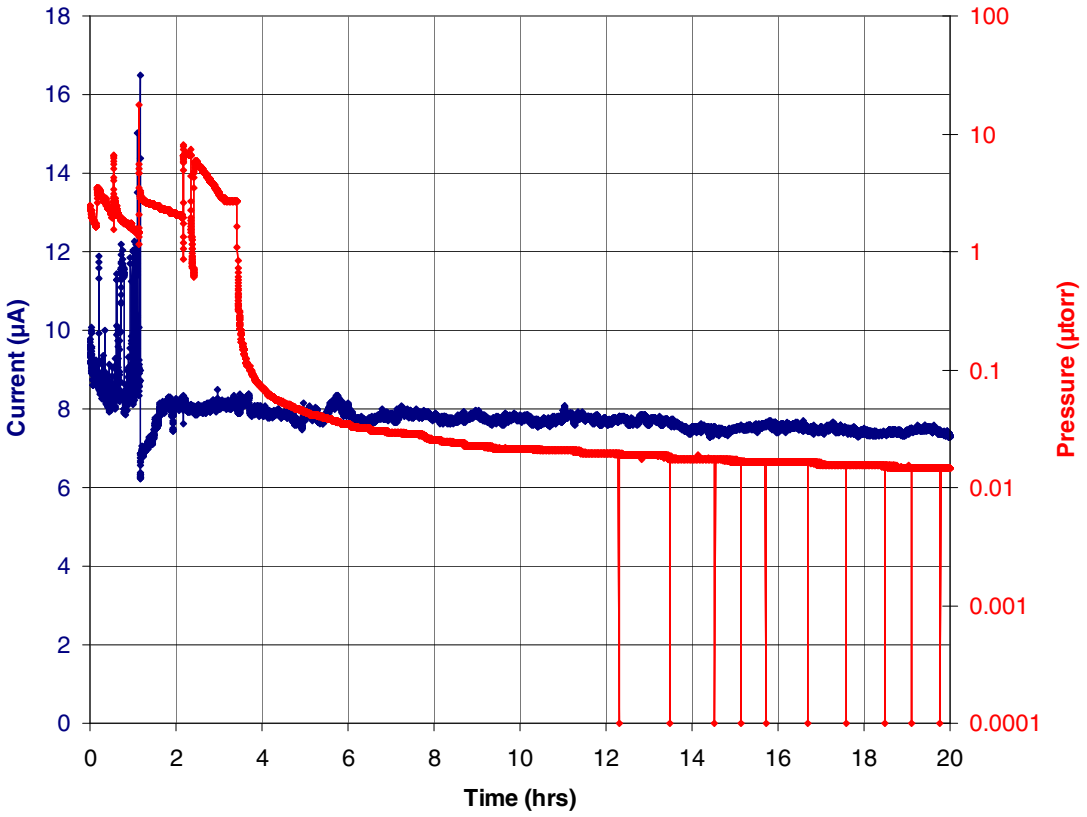

Figure 4.20: cBN electron field emission over time at constant macroscopic field of 5.22 V/μm and in water vapor.

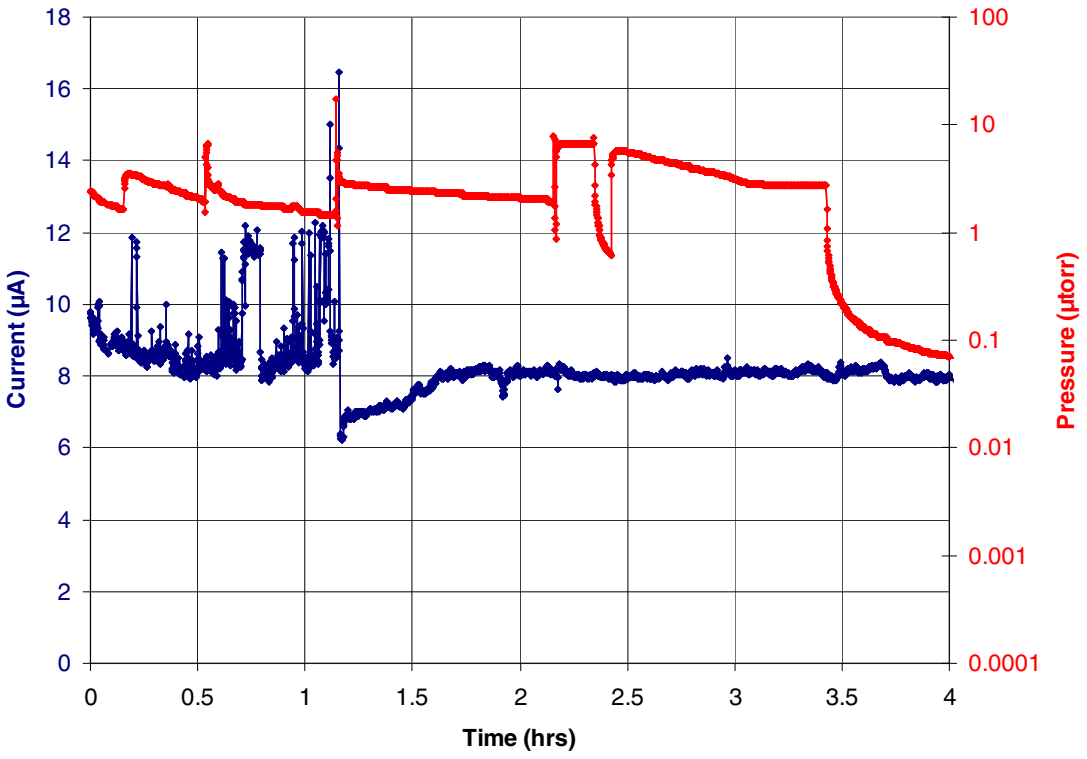

Figure 4.21: cBN electron field emission at over time constant macroscopic field of 5.22 V/μm and in water vapor, focused on the first four hours.

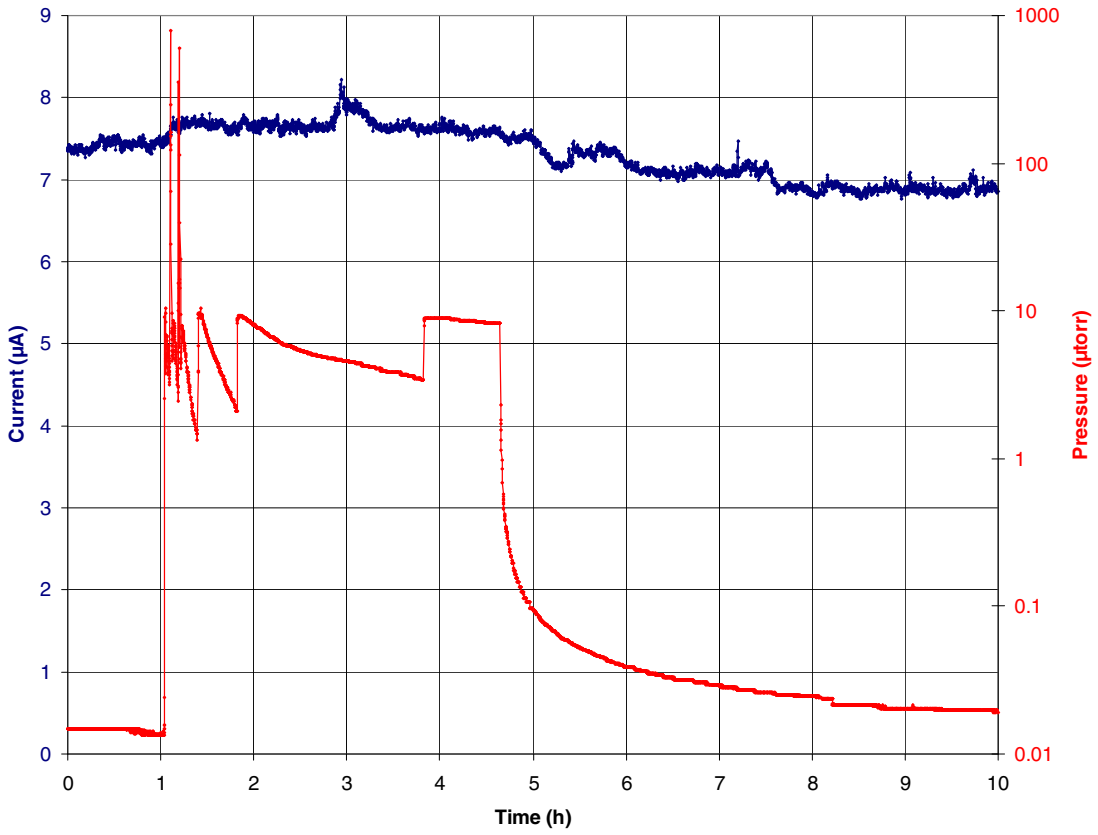

Figure 4.22: cBN Electron Field Emission recovery at constant macroscopic field of 5.22 V/μm and in water vapor [10].

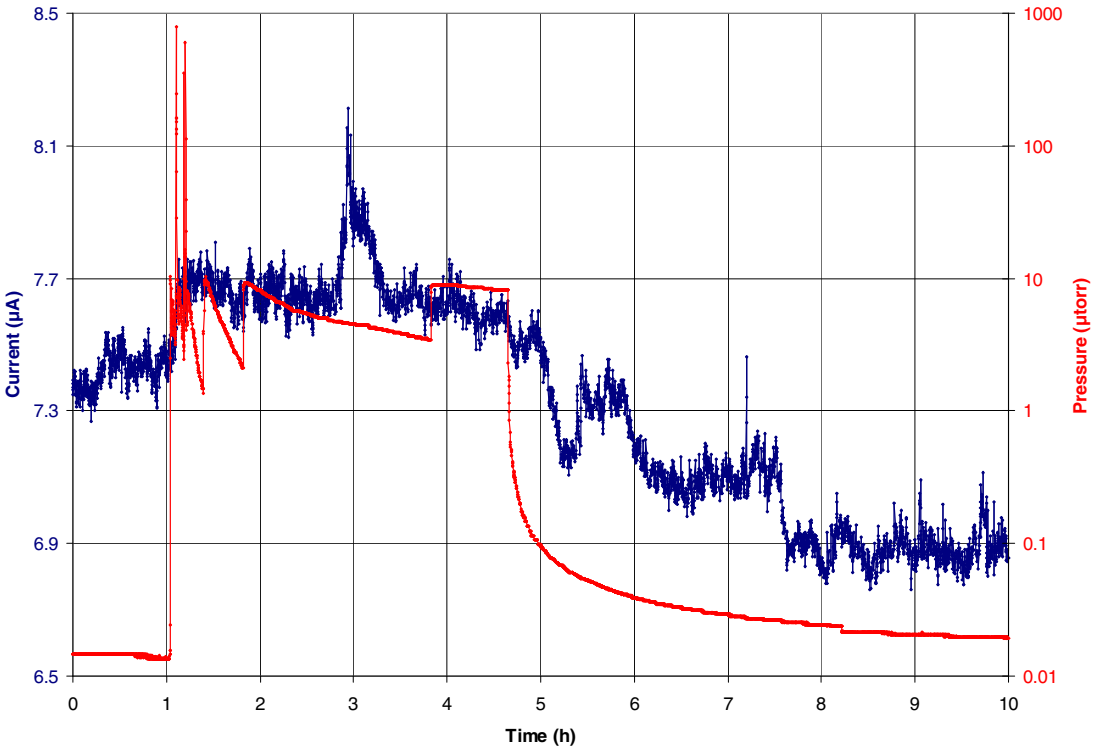

Figure 4.23: cBN Electron Field Emission recovery at constant macroscopic field of 5.22 V/μm and in water vapor (exploded view of the current scale) [10].

4.4 Summary

In this chapter, we have introduced the basic theory of field electron emission, through its historical development to its present day understanding in the generalized Fowler-Nordheim formalism. We also introduced the concept of field enhancement, and its impact on field emission measurement. The current understanding of field emission from semiconductors was also presented, which strengthens our motivation to pursue the study of BN films for their field emission properties.

We subsequently describe the apparatus employed in our field emission measurements, and proceed to present the data for measured films. Electron emission thresholds were measured from under $1\,\mathrm{V}/\mu\mathrm{m}$ up to just under $20\,\mathrm{V}/\mu\mathrm{m}$ in vacuum. Sweep measurements made, once an upper current limit was established on the experiments. A repeatability of emission results was demonstrated, albeit with some indications of threshold shift, possibly due to the desorption of adsorbate impurities on the surface of the film, which are removed with increased exposure to the vacuum environment.

In time dependence measurements over constant extraction field, we demonstrate the stable emission of our *c*BN films in an oxygen environment over periods of extended operation. An interesting feature of emission recovery in oxygen was demonstrated, with an apparent complete recovery $\sim$30 minutes after exposure.

The delay in the recovery of emission to pre-oxygen exposure levels may be attributed to the desorption of multiple layers of emission-inhibiting adsorbates. One of the characteristics of the *c*BN films grown using the technique introduced in Chap-

ter II is the propensity for the deficiency of nitrogen ions during growth, making the films slightly non-stoichiometric and p-type [26]. This condition would make available boron ions for reaction with oxygen, potentially creating a boron oxide adsorbate at the emission surface and inhibiting emission.

A water vapor environment appears to have had the most dramatic effect in suppressing the ignition of field emission from our films, even at low fields. In the time dependence measurements, the emission current seems to track the water vapor pressure in its rise and fall but slightly, on the order of 5%.

Time dependence measurements in xenon suggest adsorbate diffusion mechanism on the emission surface. The measurements reasonably indicate that a cBN film unencumbered by adsorbates would exhibit relatively stable emission in the presence of xenon gas, considering the inert nature of both xenon gas and boron nitride.

CHAPTER V

DATA REDUCTION AND ANALYSIS

5.1 RHEED and FTIR Analysis

As seen in Chapter III, the RHEED results show that the measured films are primarily *c*BN at the surface, with some texture and roughness. FTIR shows that the cross-sectional volume fraction of our films was typically greater than 70% *c*BN. The film growth process, with the requisite phase transitions, ensures that there is always some *h*BN in the data. However, FTIR in combination with RHEED data indicates that the emission surface can be assumed to be *c*BN.

5.2 AFM Analysis - Nanotexture

AFM provides data on the average roughness of our films, which can be taken to represent peak height for the model of the emission surface, described as a distribution of self-assembled protruberances resembling prolate half-ellipsoids of revolution, arranged on a flat surface as described by Kosmahl [66].

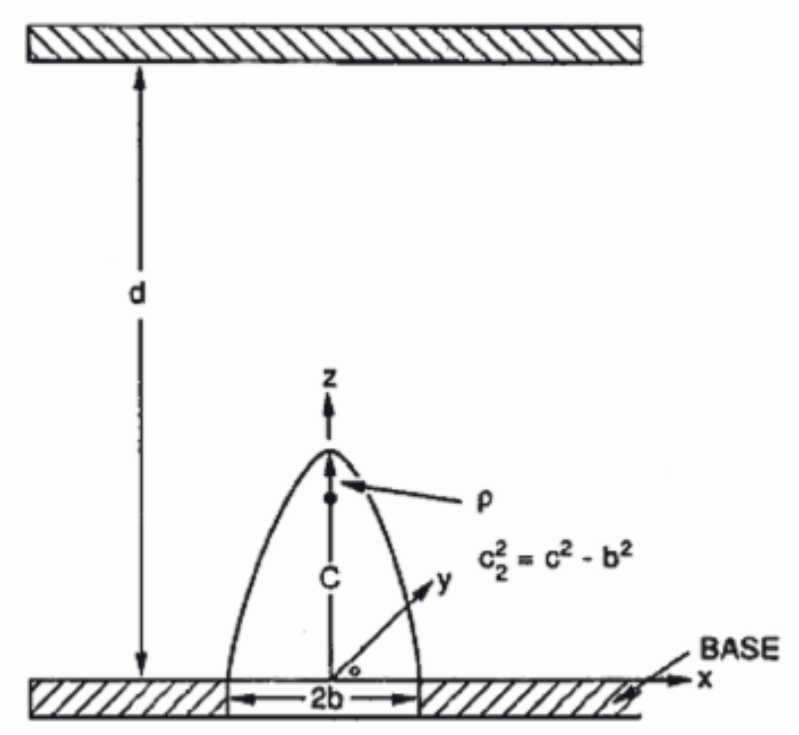

Figure 5.1: Geometry of assumed half ellipsoid of revolution and cross section of an elliptical cylinder.

5.3 Analysis of Field Emission Measurements

A least-squares regression fit of the threshold emission measurement *in vacuo* (Fig.4.6) yielded an intercept value of $ln\{R_V\} = -13.85$, and a slope of $S_V = -21.54\,V$, with a coefficient of fit determination value of $R^2 = 0.99$. Recalling that $R_V = \{\lambda_1 A a \beta^2/\phi_w\}$ and $S_V = \left\{-\mu_1 b \phi_w^{3/2}/\beta\right\}$ per Equation 4.16, we calculate $R_V = 9.61 \times 10^{-7}\,A/V^2$.

We can estimate a nominal area of emission for our FE samples using AFM data from section 3.4.2. Assuming the measured average grain size $\langle gs \rangle$ effectively corresponds to the average cross-sectional area[1] of a typical emission feature $\pi \cdot \langle b \rangle^2$, which we model as a half ellipsoid of revolution, we can use the area of measurement

[1] $\langle b \rangle$ references Figure 5.1, *i.e.* $b \neq \langle b \rangle$

to determine an upper bound for the field emission area:

$$\begin{aligned} \langle \text{gs} \rangle \times number\ of\ grains &= upper\ bound\ on\ emission\ area \\ &= 0.05\ \mu m^2. \end{aligned} \tag{5.1}$$

Based on the area of AFM measurement, we determine the upper bound percentage of the emission area to be

$$\frac{0.05\ \mu m^2}{0.74\ \mu m^2} \times 100\% = 6.76\%\,, \tag{5.2}$$

corresponding to an emission site density of

$$\frac{294\ sites}{0.74\ \mu m^2} = 397.30\ sites/\mu m^2\,. \tag{5.3}$$

Martin et al. [67] derived an estimate for the electric field at the apex of a rotationally symmetric ellipsoidal emitter, in a diode configuration with a planar anode, in the limit as the distance between the anode and the apex is much larger than the radius of the apex ($D \gg a_s$):

$$F_{tip} \approx \frac{2V_0}{a_s \cdot ln\left(\frac{4D}{a_s}\right)}. \tag{5.4}$$

Here F_{tip} and V_0 are provided in units of V/m and V, respectively. Jensen and Forbes [68] have derived an upper bound approximation for the *area factor*, b_{area}, of an ellipsoidal emitter, accounting for the functional dependence of the emission area on the field at the apex of the ellipsoid, and is defined by an integral over the tip surface:

$$b_{\text{area}}\left(F_{tip}\right)\big|_{ellipsoid} \approx 2\pi a_s^2 \left(\frac{eF_{tip}}{b_{FN}^0 + eF_{tip}}\right). \tag{5.5}$$

where b^0_{FN} is one of the Fowler-Nordheim parameters from the derivation of the simple Fowler-Nordheim current with the Schottky image potential, as found in Equation A.10 of Appendix A. b_{FN} ($= c\, in\, Eqn.$ A.10) evaluated at $v(y) = v_0$, where $v_0 \approx 0.94$ in the zero temperature limit [69], and ϕ_w is the effective barrier height for electron field emission [2], is then given by

$$\Rightarrow b^0_{FN} = \frac{8\pi}{3h}\sqrt{2m\phi_w^3}\,(0.94)\,. \tag{5.6}$$

Substituting Equation 5.4 into 5.5 yields:

$$b_{\text{area}}\,(F_{tip})\,\big|_{ellipsoid} \approx \frac{4\pi a_s^2 eV_0}{a_s ln\left(\frac{4D}{a_s}\right) b^0_{FN} + 2eV_0}. \tag{5.7}$$

Putting Equation 5.6 into Equation 5.7, we finally obtain a form for the area factor of an emission site, which will permit us to estimate an effective workfunction:

$$b_{\text{area}} \approx \frac{4\pi a_s^2 eV_0}{\frac{8\pi a_s}{3h}\left(2m\phi_w^3\right)^{1/2}(.93685)\, ln\left(\frac{4D}{a_s}\right) + 2eV_0}. \tag{5.8}$$

Let the notional area of emission A $= b_{\text{area}} \times$ "number of grains", where "number of grains" $=$ 294 from the AFM data in section 3.4.2

$$A = \frac{4\pi a_s^2 eV_0\,(294)}{\frac{8\pi a_s}{3h}\left(2m\phi_w^3\right)^{1/2}(.93685)\, ln\left(\frac{4D}{a_s}\right) + 2eV_0}, \tag{5.9}$$

and combine R_V and S_V from Equation 4.16, eliminating β

$$\begin{aligned} R_V \cdot S_V^2 &= \left(\frac{\lambda_1 A a \beta^2}{\phi_w}\right)\cdot\left(\frac{-\mu_1 b \phi_w^{3/2}}{\beta}\right)^2 \\ &= ab^2 A\lambda_1\mu_1^2\phi^2. \end{aligned} \tag{5.10}$$

[2]Note that this is *not* the same as the workfunction which governs the emission probability in thermionic emission. Here ϕ_w is more formally related to the electron affinity. See Figure 5.2 for a description of how these parameters are related.

Substitute for ab^2 using Equation 4.12 and for A using Equation 5.8. After isolating ϕ_w we arrive at the relation

$$\frac{R_V S_V^2}{(4\pi a_s^2 e V_0)(ab^2)(\lambda_1 \mu_1^2)(294)} = \frac{\phi_w^2}{\left(\frac{8\pi a_s}{3h}\right)(2m\phi_w^3)^{1/2}(.93685)\, ln\left(\frac{4D}{a_s}\right) + 2eV_0}. \tag{5.11}$$

We then calculate the radius of the apex a_s (which corresponds to ρ in Figure 5.1) using $\langle \mathrm{b} \rangle = \sqrt{\langle \mathrm{gs} \rangle / \pi}$, such that $a_s = \frac{\langle \mathrm{b} \rangle^2}{\langle \mathrm{c} \rangle} = \frac{\langle \mathrm{gs} \rangle}{\pi \langle \mathrm{c} \rangle} = 0.62\, n\mathrm{m}$, and $\langle \mathrm{c} \rangle$ is the average feature height from our AFM measurements in section 3.4.2, corresponding to "c" in Figure 5.1 on page 81, and making Equation 5.11 become

$$\frac{\pi \langle \mathrm{c} \rangle^2 R_V S_V^2}{\left(4 \langle \mathrm{gs} \rangle^2 e V_0\right)(ab^2)(\lambda_1 \mu_1^2)(294)} = \frac{\phi_w^2}{\left(\frac{8 \langle \mathrm{gs} \rangle}{3h \langle \mathrm{c} \rangle}\right)(2m\phi_w^3)^{1/2}(.93685)\, ln\left(\frac{4\pi \langle \mathrm{c} \rangle D}{\langle \mathrm{gs} \rangle}\right) + 2eV_0} \tag{5.12}$$

.

Equation 5.12 is an equation of order 2 in ϕ_w, with terms in $\phi_w^{3/2}$. To obtain a solution, a polynomial in integer power was created from Equation 5.12, a *quartic* in ϕ_w, to eliminate fractional powers of ϕ_w. The roots of the quartic are then used to solve Equation 5.12 for ϕ_w; calculations yield a single, real root at $9.3\, \mathrm{m}eV$. To explore the sensitivity of our calculated value to the accuracy of the measured data, we varied the measured value of $\langle \mathrm{gs} \rangle$ and $\langle \mathrm{c} \rangle$ independently by $\pm 10\%$.

(a) A variation in $\langle \mathrm{gs} \rangle$ of $+10\%$ yields $\phi_w = 8.4\, \mathrm{m}eV$, a *decrease* of 9.6%.

(b) A variation in $\langle \mathrm{gs} \rangle$ of -10% yields $\phi_w = 10.0\, \mathrm{m}eV$, an *increase* of 7.5%.

(c) A variation in ⟨c⟩ of + 10% yields $\phi_w = 10.0\,\mathrm{m}eV$, an *increase* of 7.5%.

(d) A variation in ⟨c⟩ of - 10% yields $\phi_w = 8.4\,\mathrm{m}eV$, an *decrease* of 9.6%.

This suggests that the method of derivation used to calculate the experimental value of $9.3\,\mathrm{m}eV$ is relatively stable with respect to its dependence on the measured input data.

Although no other reliable empirical data on the workfunction for *c*BN is currently available, *ab initio* calculated values of $7.75\,eV$ for the bulk *c*BN (110) surface, based on density functional theory, has been published by Ooi, *et al* [70], as well as a value of $12.6\,eV$ for *h*BN, based on the extended Hückel method [71]. Note however that for field emission from a semiconductor, the work function (energy difference between Fermi level and vacuum level) is very much larger than the electron affinity. This is indeed what is observed in the case of cBN. See Figure 5.2 for a comparison of the work function and the electron affinity.

Considering now the low electron affinity value measured for our samples of cBN, we expect that the emission would be influenced strongly by field enhancement at the tips of the individual emitters. The following is an estimate of the strength of such an enhancement as it relates to the specific geometry of the emission surface as measured by AFM. If we relate Equation 5.4 to the relationship between the local field and the applied voltage, which defined β (= LFVR, see page 49), we can estimate $F_{tip} \approx 2\,GV/m$ corresponding to a β value of $267/\mu$m, and a field enhancement factor of $\gamma = \beta \cdot D \approx 6681$. We've previously identified semiconductor properties which affect carrier concentration availability as playing an important role. Imperfections

due to nonuniformities in film growth, which introduce surface roughness as well as localized stoichiometric variations capable of creating defect traps in the material, not to mention the polycrystalline nature of the BN films, play a significant role in determining the ultimate effective barrier height of the material. More transient effects such as contributions from adsorbates on the surface more than likely also play a role.

The differences in surface conditions as well as nonuniformities intrinsic to the *as-grown* material will contribute directly to the surface electronic structure, which as demonstrated in our calculation from experimental parameters is a substantial contributor in the empirical determination of an effective workfuction. These significant factors are not accounted for in the *ab initio* theoretical results, which are the basis for the published values in the literature.

The tunneling barrier potential that we extract from the F-N expression, at $9.3\,\mathrm{m}eV$, is very much smaller than typical values ($\sim$ a few eV) of the workfunction for conventional cold cathode materials such as cesiated GaAs and molybdenum. What then is the physical basis for such a small barrier potential and how is it related to the electronic structure of the BN surface? Some physical insight can be gained by referring to Figure 5.2 which shows the profile of the electronic band structure at the surface of a p-type semiconductor. The choice of p-type doping here is motivated by an earlier observation that BN films on silicon tend to grow deficient in nitrogen such that acceptor impurity levels are formed in the vicinity of the valence band edge [26]. Referring to Fig. 5.2, band bending occurs at the surface

resulting in the formation of a potential barrier through which electrons must tunnel in order to exit the BN surface. The effective barrier height is related to the electron affinity, χ , being the difference between the conduction band minimum and the vacuum level. In common semiconductor such as Si and GaAs the band gap is on the order of 1 to $2\,eV$ with substantial electron barrier/work function values of a few eV, making them unsuitable for cold cathode emission applications. Coating with Cs, which has a relatively low work function ($\sim 1.8\,eV$) can reduce the electron affinity of GaAs surfaces, for example, leading to enhanced field emission. An alternative approach is to use a semiconductor with a wider band gap such that the conduction band approaches more closely to the vacuum level (see Fig. 5.2) thereby reducing the electron affinity.

In extreme cases, where the bandgap is very large (e.g. in diamond, $5.5\,eV$, or in cBN, $6.4\,eV$), the conduction band can even overlap the vacuum energy level, leading to so called "Negative Electron Affinity", or NEA [72]. While this concept (at least the "N") must be treated with some caution, as the surface electronic states are highly sensitive to defects and contamination, it appears that the low value of ϕ_w measured for cBN is a direct consequence of the wide gap nature of the band structure, and is evidence in favor of an NEA-type of emission mechanism in cubic boron nitride.

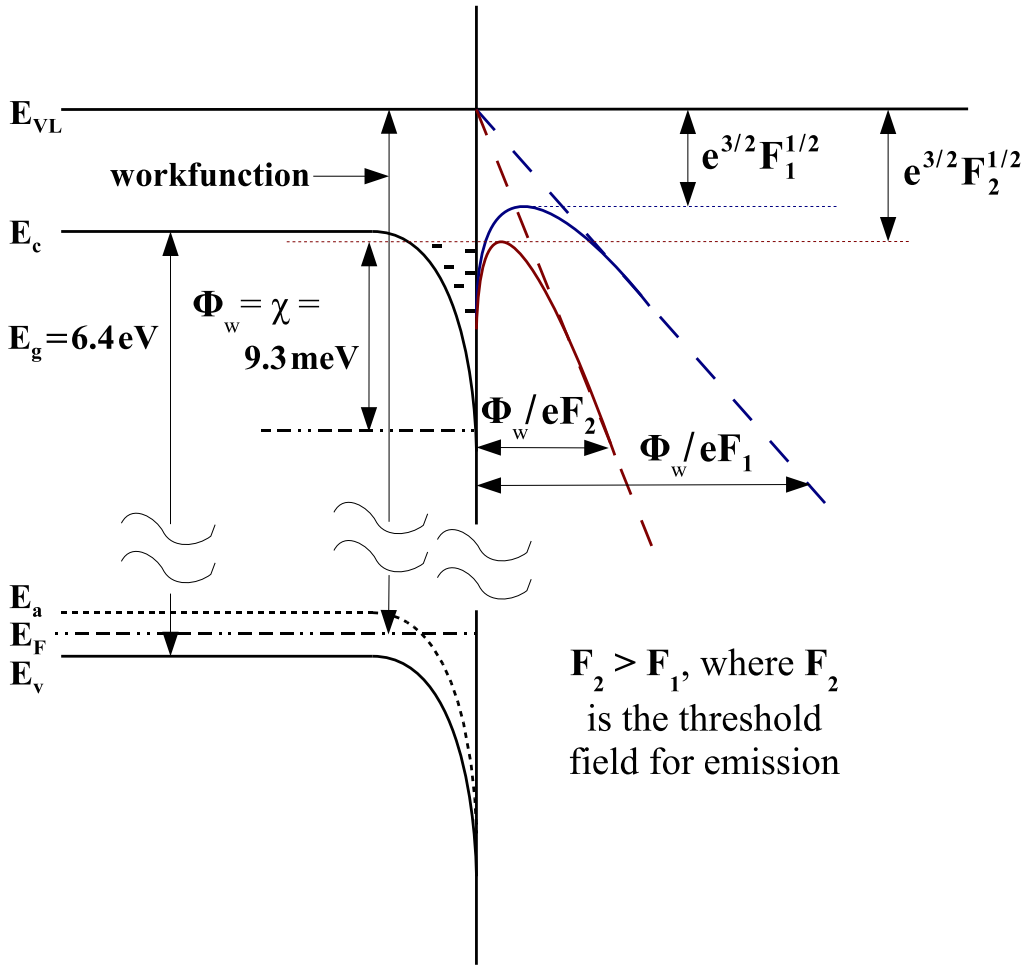

Figure 5.2: Electron energy band diagram for cubic boron nitride thin film (*NOT* to scale), depicting changes in the barrier height and width as a function of an increasing externally applied field. Φ_w is the effective barrier height, which is identical to the electron affinity χ in this p-type semiconductor system.

5.4 Stochastic Considerations

The current from a single emitter is approximated by the product of the $b_{\text{area}}(F_{tip})$ and the apex current density $J(F_{tip})$. The usual approximation $F \approx \beta_g V$ relating the apex field to voltage is seen to be reasonable from the geometric models, but I_{tip} varies approximately as $\Theta V^3 exp(-\Omega/V)$, accounting for a linear increase in active emission area from an emitting tip, as a function of increasing applied voltage. An ensemble of emitters will contain a distribution of emission site radii; this distribution has been modeled as both log-normal [73] and Rayleigh distribution [74], which are similar in appearance. In addition, adsorbates can collect on an emitter surface, causing a variation in the effective workfunction. A model of these effects for an ensemble will then take on the form [57]

$$I_{ensemble}\left(V_g\right) \;=\; N_{tips} \sum_{a} \left(V_g, \mu, \sigma\right) \sum_{\phi} \left(V_g, \Delta\phi_w\right) b_{\text{area}}\left(F_{tip}\right) J\left(F_{tip}\right), \tag{5.13}$$

where all quantities are evaluated based on the mean radius $\langle a_s \rangle$. An adsorbate statistical factor, based on the assumption that the fraction of the surface covered by adsorbates is a pressure dependent, is proposed as

$$\sum_{\phi} \left(P\right) \;=\; \left[P_o \;+\; P exp\left(-\alpha_\phi \Delta\phi_w\right)\right] / \left(P_o \;+\; P\right), \tag{5.14}$$

where P is the vacuum pressure, $\alpha_\phi \;=\; \partial_\phi ln\left[I_{tip}\left(\phi_w\right)\right]$, and the values $\Delta\phi_w \sim 0.5\, eV$ and $P_o = 0.01\, mtorr$ are generically valid. The value for α_ϕ depends on the geometry, the field, and the workfunction through the equation for tip current. The emission

site radius statistical factor $\sum_a$ is given as

$$\sum_a (V_g, \mu, \sigma) = \frac{1}{I_{tip}} \int_0^\infty L(a; \mu, \sigma) I_{tip}(a) da,$$
$$L(a; \mu, \sigma) = \frac{1}{\sqrt{2\pi}\sigma a} exp\left\{ -\frac{1}{2\sigma^2} \left[(ln(a/\mu))^2 \right] \right\}, \quad (5.15)$$

where the log-normal distribution is again reasonable, μ represents the mean emission site radius $\langle a_s \rangle$, and σ is the spread factor. $\sum_a$ is greater than or equal to unity, due to $I_{tip}(\mu)$ being in the denominator (the film is characterized by the *average* radius, not the minimum). Assuming that the product of the statistical factors is linearly proportional with voltage, to lowest order $I_{ensemble}(V) \approx \Theta V^4 exp(-\Omega/V)$. This clearly adds to the difficulties of inferring emission area, workfunction, or field enhancement from an ensemble current using the generalized procedure [75].

The statistical model also gives insight into the emission noise. Time-varying fluctuations manifest themselves as the "flicker noise" in the current measured under constant voltage conditions. Possible causes include:

(a) the adsorption and desorption of contaminants (even at a high vacuum)

(b) sputter damage due to ion impact

(c) grain boundaries and the interplay with contaminants [76]

(d) nanoprotrusions oscillating between metastable configurations or sputtered off [77, 78]

(e) the oscillation of sites characterized by some combination of high geometrical field enhancement and low workfunction [79].

While many of these processes are rapid, the diffusion phenomena in particular can have numerous time scales long enough to effect fluctuations in current in the seconds-to-hours range. Diffusion models developed by Kleint [80] have recently been used to analyze experimental data of the performance of Mo and ZrC/Mo cathodes in oxygen environments [73]. The fluctuations in the data seem to be compatible with these diffusion models. This statistical model for ensemble field emission suggests that at the voltages at which our measurements were taken, a small percentage of emitters dominate the current. The emission will be strongly skewed in Eq. 5.15 to smaller emission sites because apex fields are inversely proportional to the apex radius, an effect exacerbated at lower fields because of the rapid decline in I_{tip}. Consequently, fluctuations in those emitters would be very apparent in field emission measurements, which our measurements reflect.

Jensen *et al.* [73] has also proposed a rough theoretical model for the change of emission from a site with a changing workfunction due to diffusion related mechanisms. Let $I(\phi_w)$ denote the initial current prior to the change in workfunction due to diffusion of admolecules, and $I(\phi_w - \Delta\phi_w)$ the current after. On the apex of the emitter, the emission area changes with field. On a given emitter tip, if a change in workfunction from ϕ_w to $\phi_w - \Delta\phi_w$ occurs over an area πr_o^2, then the fractional current change approximately relates to the fractional change in current density by

$$\frac{\Delta I}{I_{tip}} \approx \frac{\pi r_o^2}{b_{\text{area}}(\phi_w, F_{tip})} \left(\frac{\Delta J}{J}\right). \tag{5.16}$$

Ignoring variations in b_{area}, to leading order

$$\frac{J(\phi_w - \Delta\phi_w) - J(\phi_w)}{J(\phi_w)} = exp\left[\left(\frac{3b_{\text{FN}}}{2F\phi_w} + \frac{1}{\phi_w} + \frac{8\alpha c}{3}\sqrt{\frac{2m}{\phi_w^3}}\right)\Delta\phi_w\right] - 1. \tag{5.17}$$

The first (dominant) term in the exponential was found by Kleint, $\alpha = 1/137.036$ is the fine structure constant, and c is the speed of light. $\Delta\phi_w$ can be several tenths of an electronvolt, which would indicate that $\Delta J/J$ can be substantial. This model is consistent with the diffusion picture.

The field dependence of b_{area} suggests that fluctuations due to diffusion and other flicker noise sources grow larger as F decreases. The magnitude of the fluctuations in the ensemble current can be expected to be larger at lower current levels, given the smaller subset of emitters accounting for the total current. Thus the fluctuations originate with a small number of tips, which dominate the total current, in agreement with the statistical model as well as with what is observed experimentally. Conditioning the films may greatly reduce the apparent fluctuations following the model described by Eq. 5.16.

5.5 Summary

We have derived an effective workfunction for the *as-grown* cBN thin films of this research, based on the application of the generalised Fowler-Nordheim theory to the electron field emission measurements presented in Chapter IV. The value of approximately $9.3\,m$eV is based on a lower bound estimate of the emission area, which takes into account the emission area dependence on the applied electric field. A model of the film surface as an ensemble of self-assembled protruberances in the shape of prolate half ellipsoids of revolution on a flat surface, is representative of the morphology of our cBN films as demonstrated in the results of our characterization in Chapter III, and also factors into the derivation.

We have compared our derived results to the limited number of available values for BN workfunction in the literature, which are based on *ab initio* calculations, and have addressed the differences in terms of various phenomena. Field enhancement and semiconductor properties will affect the availability of carriers for emission. Imperfections due to nonuniformities in film growth, which introduce surface roughness as well as localized stoichiometric variations capable of creating defect traps in the material, not to mention the polycrystalline nature of the BN films, play a significant role in ultimately determining the effective workfunction of a material. More transient effects such as contributions from adsorbates on the surface more than likely also play a role.

The effective barrier height is related to the electron affinity, χ , being the difference between the conduction band minimum and the vacuum level. Where the bandgap is very large (e.g. in diamond, $5.5\,eV$, or in cBN, $6.4\,eV$), the conduction band can even overlap the vacuum energy level, leading to so called "Negative Electron Affinity", or NEA. It appears that the low value of ϕ_w measured for cBN is a direct consequence of the wide gap nature of the band structure, and is evidence in favor of an NEA-type of emission mechanism in cubic boron nitride.

We have also reviewed stochastic considerations from a theoretical perspective, relating the likely distribution of emission site radii among an ensemble of emitters on a given sample, as well as the transient nature of the adsorbates on an emission surface, and the electron field emission from our films. In addition, we have reviewed a proposed diffusion model for the adsorption and desorption of contaminants from

the surface, and its implications for flicker noise in emission measurements from films typefied by the cBN films in this research.

CHAPTER VI

CONCLUSIONS AND FUTURE WORK

6.1 Conclusions

This dissertation presents the results of a systematic study of the electron field emission of boron nitride thin films. The research presented in this work establishes nanostructured thin film Boron Nitride (BN) as a robust and chemically inert material with a low work function capable of sustainable electron emission in a space plasma environment.

In Chapter II we have presented the reduced bias thin film growth technique, used with the ion-assisted RF plasma deposition process, as the method for the fabrication of the *c*BN films that were the subject of the field electron emission research presented in this dissertation. The samples were grown in an Argon/Nitrogen gas environment, at a growth pressure of 5 mtorr on p-type Silicon (100) substrates, of resistivity ρ = 2 - 10 Ω-cm, subject to a substrate bias of ∼100 V for 3 hours, until the cubic phase of boron nitride was achieved. Subsequently, the substrate bias was reduced to ∼-56 V, and growth continued for an additional 8 hours, yielding *c*BN film thicknesses of ∼2000 Å. *As grown* cubic boron nitride films display three distinct

regions in the film structure: a very thin amorphous layer of BN $\sim 4\,nm$ in thickness, a turbostratic hexagonal Boron Nitride layer ($\sim 30\,nm$ thick), above which the cubic phase nucleates.

In Chapter III we describe the morphological characterization of the BN films under study here, which include Reflection High Energy Electron Diffraction (RHEED), Fourier Transform Infrared Spectroscopy (FTIR), and Atomic Force Microscopy (AFM). From the RHEED data of the films under study, we were able to identify the crystal structure at the surface to be qualitatively *c*BN. The data shows the sample to be a polycrystalline film rather than a single crystal, composed of partially oriented crystallites of *c*BN with a distribution of different crystal plane normals oriented relatively parallel to the Si substrate surface normal as indicated by the (111), (220), and (311) crystallographic reflections in the RHEED data. The distribution of *in-plane* relative orientation of these crystallites is evidenced by the azimuthal spread in the RHEED images. The radial spread in the diffraction maxima indicate the out-of-plane variation of the crystallite orientation, contributing to surface roughness. The FTIR data showed our films to be overwhelmingly *c*BN in constitution, with a percent volume fraction greater than 75%. Although this data does not directly determine the phase constitution at the film surface, since it is taken in transmission mode, it reasonably establishes a lower limit of surface *c*BN fraction, independent of data from any of the complementary techniques. The AFM images provide data which is analyzed to give surface roughness and feature size information for the films used in our field emission experiments. We measured $\langle c \rangle =$

79 nm, with a mean RMS roughness of 19 nm. $\langle \mathrm{gs} \rangle = 155\ nm^2$, with $\sigma_{\mathrm{gs}} = 84\ nm^2$, yielding $\langle \mathrm{b} \rangle = \sim 7\ nm$. Results were calculated over an area of 0.74 $\mu\mathrm{m}^2$, containing on average 294 grains.

After the material and morphological characterization of the samples were performed, the samples were subjected to a series of systematic electron field emission measurements, the details of which are laid out in Chapter IV. First, the development of field emission theory is presented, including a discussion on particular aspects of field emission from semiconductors. A description of the field emission measurement system is presented, in which a custom-designed UHV chamber was employed, and a planar diode configuration was utilized for the experiments. Electron emission thresholds were measured from under $1\,\mathrm{V}/\mu\mathrm{m}$ up to just under $20\,\mathrm{V}/\mu\mathrm{m}$ in vacuum. Sweep measurements were made, once a upper current limit was established on the experiments. A repeatability of emission results was demonstrated, albeit with some indications of threshold shift, possibly due to the desorption of adsorbate impurities on the surface of the film, which are removed with increased exposure to the vacuum environment. In time dependence measurements over constant extraction field, we demonstrate the stable emission of our cBN films in an oxygen environment over periods of extended operation. An interesting feature of emission recovery in oxygen was demonstrated, with an apparent complete recovery $\sim$30 minutes after exposure. The delay in the recovery of emission to pre-oxygen exposure levels may be attributed to the desorption of multiple layers of emission-inhibiting adsorbates. One of the characteristics of the cBN films grown using the technique introduced

in Chapter II is the propensity for the deficiency of nitrogen ions during growth, making the films slightly non-stoichiometric and p-type. This condition would make available boron ions for reaction with oxygen, potentially creating a boron oxide adsorbate at the emission surface and inhibiting emission. A water vapor environment appears to have had the most dramatic effect in suppressing the ignition of field emission from our films, even at low fields. In the time dependence measurements, the emission current seems to track the water vapor pressure in its rise and fall but slightly, on the order of 5%. Time dependence measurements in xenon suggest an adsorbate diffusion mechanism on the emission surface. The measurements resonably indicate that a cBN film unencumbered by adsorbates would exhibit relatively stable emission in the presence of xenon gas, considering the inert nature of both xenon gas and boron nitride.

The morphological characterization data of the samples in Chapter III and the field emission measurement data from Chapter IV facilitate the data reduction and analysis of the field emission, developed in Chapter V. Here we have derived an effective workfunction (more accurately, a value for the electron affinity) for the *as-grown* cBN thin films of this research, based on the application of the generalised Fowler-Nordheim theory to the electron field emission measurements presented in Chapter IV. The value of approximately $9.3\,m$eV is based on a lower bound estimate of the emission area, which takes into account the emission area dependence on the applied electric field. A model of the film surface as an ensemble of self-assembled protruberances in the shape of prolate half ellipsoids of revolution on a flat surface,

is representative of the morphology of our cBN films as demonstrated in the results of our characterization in Chapter III, and also factors into the derivation. Field enhancement and semiconductor properties will affect the availability of carriers for emission. Imperfections due to nonuniformities in film growth, which introduce surface roughness as well as localized stoichiometric variations capable of creating defect traps in the material, not to mention the polycrystalline nature of the BN films, play a significant role in determining the ultimate effective workfunction of a material. More transient effects such as contributions from adsorbates on the surface more than likely also play a role. The effective barrier height is related to the electron affinity, χ , being the difference between the conduction band minimum and the vacuum level. Where the bandgap is very large (e.g. in diamond, $5.5\,eV$, or in cBN, $6.4\,eV$), the conduction band can even overlap the vacuum energy level, leading to so called "Negative Electron Affinity", or NEA. It appears that the low value of ϕ_w measured for cBN is a direct consequence of the wide gap nature of the band structure, and is evidence in favor of an NEA-type of emission mechanism in cubic boron nitride.

We have also reviewed stochastic considerations from a theoretical perspective, relating the likely distribution of emission site radii among an ensemble of emitters on a given sample, as well as the transient nature of the adsorbates on an emission surface, and the electron field emission from our films. In addition, we have reviewed a proposed diffusion model for the adsorption and desorption of contaminants from the surface, and its implications for flicker noise in emission measurements from films typefied by the cBN films in this research.

6.2 Future Work

The future work recommended by the author is divided into two main categories. In section 6.2.1, suggestions are proposed for improvements of the boron nitride film samples for future field emission research. Recommendations in section 6.2.2 address the future of the field emission study of boron nitride thin films.

6.2.1 Improvements to the Boron Nitride Growth Chamber

(a) The BN growth facility should be expanded with larger sources and substrate heating capability to achieve greater uniformity over a larger area.

(b) An automated rotation system should also be included to improve film growth uniformity.

(c) The growth process could be optimized with respect to the post-conditioning performance rather than the less stable pre-conditioning performance. This would be predicated on the establishment of a film conditioning protocol

6.2.2 Improvements on Field Emission Measurements

(a) Mass Flow Controllers to provide electronic feedback stabilization of gases for environmental exposure studies.

(b) A study to correlate carrier mobility with field emission

(c) Make field emission measurements using a temperature control mechanism; modify the measurement chamber to include a cold-finger on which the sample is mounted, to measure field emission as a function of temperature and ex-

pand the current knowledge of the current-voltage regimes in a wide bandgap material such as BN

(d) Use experimental field emission data from our films in collaboration with theoretical study to model the variability in the emission tip to anode distance, to enhance the statistical hyperbolic model of electron field emission so that it more accurately represent systems of self-assembled asperities such as BN thin films

(e) Ultraviolet photospectroscopy of our BN films might provide better understanding of the electron energy band structure of our BN films, and its contribution to the electron field emission from BN and other similar wide band gap semiconductors, in particular the effects of surface traps and defects

(f) Research into growing BN films on a substrate such as diamond, which has a closer lattice match to cBN, and would make possible the development of a diode system which could be used for switching control of electron field emission from boron nitride films, by influencing the availability of carriers at the emission surface

(g) Phosphor screen anodes with grid markers would allow ease of isolation of emission points and regions, and facilitate spatial correlation with SEM scans and other post emission measurements that might be made.

(h) Once repeatable emission performance is obtained and the sample growth stabilized, a sample conditioning program should be instituted, and the sample

growth process revisited based on the results of that conditioning. The initial performance of these samples were tested, but there was insufficient reliability for a full conditioning program. Performance may change or degrade slightly as sharp tips are eroded in the conditioning process, but would be balanced by the improvement in stability as the surface morphology becomes more uniform and more emission points are activated. Sample measurements taken over tens of hours under AC bias to fully exercise the sample and to help prevent emission site overheating during initial emission, would yield valuable information about the conditioning and long term stability of the sample.

(i) The growth process could then be optimized in reference to the post-conditioning performance rather than the less stable pre-conditioning performance.

(j) The use of a gate structure in the field emission measurement may allow for a more sophisticated exploration of the surface electronic characteristics of the films, as well as providing a means to circumvent issues associated with non-uniformity in the sample substrate affecting the uniformity of the applied extraction field. For the gate testing portion of the project, while this could be a separate project in and of themselves, testing prototype gates with a variety of field emission materials, such as BN films, Si tips, Mo tips, CNT arrays, would further our understanding and ability to fabricate gates for field emission with a broader applicability, as well as establish a standard against which the measurements from different emissive materials and systems may be referenced.

APPENDIX

APPENDIX A

THEORY OF FIELD EMISSION FROM METALS

Introduction

The Fowler-Nordheim theory is generally used in order to quantitatively describe the FE process for metals, which requires deriving the FE current density as a function of the electric field.

Derivation

Since this process is essentially a tunneling process, the tunneling transition probability for the electron to tunnel through the potential barrier and the number of electrons incident on the potential barrier must be found. For clarity, what follows is developed in *Gaussian*, or *cgs* units (for *c*entimeter, *g*ram, *s*econd. Integrating these over all energy values gives the desired current density. The assumptions of the Fowler-Nordheim theory are [48]:

(a) The metal obeys the free electron model of Sommerfeld with Fermi-Dirac Statistics.

(b) The metal surface is planar, reducing the problem to a one-dimensional one. So long as the potential barrier thickness is several orders of magnitude less than the emitter radius, this assumption is justified.

(c) The potential in the metal, $V_1(z)$, is a constant, $-V_0$. The potential barrier outside the metal is entirely due to the image forces, $V_z = -e^2/4z$; the applied electric field does not affect the electron states in the metal.

(d) The temperature of the system is $T = 0\ K$.

Here the $\hat{z}$-direction is normal to the metal surface, pointing away from the surface. The second phase is a vacuum. The origin of the applied electric field is the metal surface, and the field contribution to the potential energy is $-eFz$ [49]. Thus, the effective potential energy is

$$V(z) = \begin{cases} -V_0, & \text{for } z < 0 \\ -eFz - \frac{e^2}{4z}, & \text{for } z > 0. \end{cases} \tag{A.1}$$

In addition, the model assumes that the electrons in the metal remain at equilibrium, despite the electrons escaping the metal surface. Integrating the product of the flux of electrons incident on the surface potential barrier and the tunneling probability over all electron energies. Define E_z to be the z-component of the electron energy:

$$E_z = E - \frac{p_x^2}{2m} - \frac{p_y^2}{2m} = \frac{p_z^2}{2m} + V(z). \tag{A.2}$$

Let $N(E_z)\,dE_z$ be the number of electrons per unit area per second with the z-component of their energy within dE_z of E_z incident on the surface potential barrier; and let $D(E_z)$ be the tunneling probability, also known as the transmission coefficient. Thus, the product $D(E_z)\,N(E_z)\,dE_z$ gives the number of electrons per unit area per second within dE_z of E_z emitted from the metal surface. Then the current density is

$$J = e\int_{-V_0}^{\infty} D(E_z)\,N(E_z)\;dE_z. \tag{A.3}$$

The electron flux incident on the metal surface is

$$\begin{aligned} N(E_z)\,dE_z &= \frac{2}{h^3}dE_z\int_{-\infty}^{\infty}\int_{-\infty}^{\infty}\frac{dp_x dp_y}{1+exp\left(\frac{E_z-\mu}{k_BT}+\frac{p_x^2+p_y^2}{2mk_BT}\right)} \\ &= \frac{4\pi mk_BT}{h^3}ln\left(1+e^{-(E_z-\mu)/k_BT}\right)dE_z, \end{aligned} \tag{A.4}$$

where h is the Planck constant, $-\mu$ is the work function, k_B is the Boltzmann constant, T is the temperature, and m is the electron mass. Using the JWKB approximation, the transmission coefficient is

$$D(E_z) = exp\left[-\frac{8\pi(2m)^{1/2}}{3he}\frac{|E_z|^{3/2}}{F}v(y)\right], \tag{A.5}$$

where F is the applied electric field. The Nordheim function, $v(y)$, is

$$v(y) = 2^{-1/2}\left[1+\left(1-y^2\right)^{1/2}\right]^{1/2}\cdot\left[E(k)-\left\{1-\left(1-y^2\right)^{1/2}\right\}\right]K(k), \tag{A.6}$$

where $y = \left(e^3F\right)^{1/2}/|E_z|$. The *complete elliptic integrals of the first and second kinds*, $E(k)$ and $K(k)$, are given by

$$\begin{aligned} E(k) &= \int_0^{\pi/2}\left(1-k^2 sin^2\alpha\right)^{-1/2}d\alpha, \qquad and \\ K(k) &= \int_0^{\pi/2}\left(1-k^2 sin^2\alpha\right)^{1/2}d\alpha, \end{aligned} \tag{A.7}$$

where $k^2 = 2\left(1-y^2\right)^{1/2}\Big/\left(1+\left(1-y^2\right)^{1/2}\right)$ [49]. Combining Eqn. A.4 and Eqn. A.5, the number of electrons within dE_z emitted per unit area per second is

$$D(E_z)\,N(E_z)\,dE_z = \frac{4\pi m k_B T}{h^3} exp\left[-\frac{8\pi\left(2m\right)^{1/2}}{3he}\frac{|E_z|^{3/2}}{F}v(y)\right] ln\left(1+e^{-(E_z-\mu)/k_BT}\right)dE_z. \tag{A.8}$$

A few applicable simplifications can be made at this point, based on our assumptions. Since field-emitted electrons have energies near $E_z = \mu$, approximating the exponent in Equation A.8 with the first two terms of a power series expansion at $E_z = \mu$ is valid. In this approximation, the exponent reduces to

$$-\frac{8\pi\left(2m\right)^{1/2}}{3he}\frac{|E_z|^{3/2}}{F}v(y) \approx -c + \frac{E_z-\mu}{d}; \tag{A.9}$$

where

$$\begin{aligned} c &= \frac{8\pi\left(2m\right)^{1/2}}{3he}\frac{\left|E_z\right|^{3/2}}{F}v\left(y\right), \\ d &= \frac{heF}{4\pi\left(2m\phi\right)^{1/2}t\left(\left(e^3F\right)^{1/2}/\phi\right)}, \\ t\left(y\right) &= v\left(y\right)-\frac{2}{3}y\frac{dv\left(y\right)}{dy}, \end{aligned} \tag{A.10}$$

and the work function is $\phi = -\mu$. For sufficiently low temperatures, the temperature dependent part of Equation A.4 reduces as follows:

$$k_BTln\left(1+exp\left(-\left(E_z-\mu\right)/k_BT\right)\right) = \begin{cases} 0, & \text{for } E_z > \mu \\ \mu - E_z, & \text{for } E_z < \mu \end{cases}. \tag{A.11}$$

Upon substituting Equation A.11 into Equation A.8, the following is obtained:

$$D\left(E_z\right)N\left(E_z\right)dE_z = \begin{cases} 0, & \text{for } E_z > \mu \\ \frac{4\pi m}{h^3}exp\left(-c+\frac{E_z-\mu}{d}\right)\left(\mu-E_z\right), & \text{for } E_z < \mu \end{cases}. \tag{A.12}$$

Integration of Equation A.12 will give the current density. Assuming that $-V_0 \ll \mu$, the Fermi energy, the lower limit of the integral can be set to $-\infty$. The current density obtained via these assumptions is

$$\begin{aligned} J &= e\int_{-\infty}^{\mu}\frac{4\pi m}{h^3}\left(\mu - E_z\right)exp\left(-c+\frac{E_z-\mu}{d}\right)dE_z \\ &= \frac{4\pi med^2}{h^3}e^{-c} \\ &= \frac{e^3F^2}{8\pi h\phi t^2\left(\left(e^3F\right)^{1/2}/\phi\right)}exp\left(\frac{4\left(2m\right)^{1/2}\phi^{3/2}}{3heF}v\left(\frac{\left(e^3F\right)^{1/2}}{\phi}\right)\right) \end{aligned} \quad (A.13)$$

.

Extension for Finite Temperatures

For finite, non-zero temperatures, the Fermi-Dirac distribution that applies to electrons indicates that there *will* be electrons in the metal with energies greater than the Fermi level. Since the transmission coefficient increases with the particle's incident energy, these electrons with energies greater than the Fermi level are more likely to tunnel through the potential barrier at the metal surface. The emission current changes only slightly from that at $T = 0\ K$ for small temperatures, but in the high temperature limit, which is *thermionic* emission, the electrons with energies greater than the barrier height constitute the majority of the current.

Using the expansion around the Fermi level in Equation A.9 in Equation A.8 and approximating the natural logarithm term for $E_z > \mu$ yields

$$ln\left(1+exp\left(-\left(E_z-\mu\right)/k_BT\right)\right) \approx exp\left(-\left(E_z-\mu\right)/k_BT\right). \quad (A.14)$$

Substituting Equations A.9 and A.14 in Equation A.8, the expression becomes

$$D\left(E_z\right)N\left(E_z\right)dE_z = \frac{4\pi mk_BT}{h^3}exp\left[-c+\left(E_z-\mu\right)\left(\frac{1}{d}-\frac{1}{k_BT}\right)\right]. \quad (A.15)$$

Integrating Equation A.15 gives the following expression for the current density for small non-zero temperature, valid only for $T \leq 1000\ K$:

$$J(T) = J(0)\,\frac{\pi k_B T/d}{sin\,(\pi k_B T/d)}, \tag{A.16}$$

where $J(0)$ is the current density at zero temperature shown in Equation A.13. Using Equation A.16 for a field of $4.7 \times 10^7\ V/cm$ and a work function of $4.5\ eV$, the current densities at room temperature and at $1000\ K$ are

$$J(300\ K) \approx 1.03J(0) \qquad and \qquad J(1000\ K) \approx 1.5J(0)\,. \tag{A.17}$$

BIBLIOGRAPHY

BIBLIOGRAPHY

[1] C. A. Taylor II, S. W. Brown, V. Subramaniam, S. Kidner, S. C. Rand, and R. Clarke. Observation of near-band-gap luminescence from boron nitride films. *Applied Physics Letters*, 65(10):1251, 1994.

[2] A. I. Lukomskii, V. B. Shipilo, and L. M. Gameza. Luminescence properties of graphite-like boron nitride. *The Journal of Applied Spectroscopy*, 57(1-2):607, 1992.

[3] E. Y. Andrei, A. Katzir, and J. T. Suss. Point defects in hexagonal boron nitride. iii. epr in electron-irradiated bn. *Physical Review B*, 57:2831, 1976.

[4] A. W. Moore and L. S. Singer. Electron spin resonance in carbon-doped boron nitride. *Journal of Physics and Chemistry of Solids*, 33:343, 1972.

[5] V. V. Lopatin and F. V. Konusov. Energetic states in the boron nitride band gap. *Journal of Physics and Chemistry of Solids*, 53:847, 1992.

[6] S. M. Rossnagel. Sputter deposition for semiconductor manufacturing. *IBM Journal of Research and Development*, 43(1):163, 1999.

[7] S. L. M. Kidner. *Ion Assisted Sputter Deposition and Structural Characterization of Cubic Boron Nitride*. PhD thesis, University of Michigan, Ann Arbor, 1994.

[8] P. A. Encarnación, Y. Sheng, and R. Clarke. Field emission studies of reduced-bias ion-assisted rf-sputtered cubic boron nitride thin films. Presented at the Second European Field Emission Workshop (EUROFE2000), Universidad SEK, Segovia, Spain, Sep 2000.

[9] L. M. Baskin, O. I. L'vov, and G. N. Fursey. General features of field emission from semiconductors. *Physica Status Solidi (b)*, 47(1):49 – 62, 1971.

[10] P. A. Encarnación, H. Goldberg, C. Deline, J. Van Noord, B. Gilchrist, and R. Clarke. Field emission of nanostructured boron nitride thin films in the presence of residual gases. Presented at the Seventeenth International Vacuum Nanoelectronics Conference (IVNC2005), Massachusetts Institute of Technology, Cambridge, Massachusetts, USA, July 2004.

[11] B. V. Spitsyn, L. L. Bouilov, and B. V. Derjaguin. Vapor growth of diamond on diamond and other surfaces. *Journal of Crystal Growth*, 52:219, 1981.

[12] S. Matsumoto, Y. Sato, M. Kame, and N. Setaka. Vapor deposition of diamond particles from methane. *Japanese Journal of Applied Physics*, 21(4):L183, 1982.

[13] S. Iijima. Helical microtubules of graphitic carbon. *Nature*, 354(6348):56, 1991.

[14] K. A. Dean and B. R. Chalamala. Current saturation mechanisms in carbon nanotube field emitters. *Applied Physics Letters*, 76(6):375, 2000.

[15] W. Zhu, C. Bower, O. Zhou, G. Kochanski, and S. Jin. Large current density from carbon nanotube field emitters. *Applied Physics Letters*, 75:873, 1999.

[16] B. E. Gilchrist. private communication, 2002.

[17] N. G. Chopra, R. J. Luyken, K. Cherrey, V. H. Crespi, M. L. Cohen, S. G. Louie, and A. Zettl. Boron nitrate [*sic*] nanotubes. *Science*, 269(5226):966, 1995.

[18] L. Bourgeois, Y. Bando, K. Kurashima, and T. Sato. Co-produced carbon and boron nitride helical cones and the nucleation of curved bn sheets. *Philosophical Magazine A*, 80(1):129, 2000.

[19] R. H. Wentorf Jr. Preparation of semiconducting cubic boron nitride. *The Journal of Chemical Physics*, 36(8):1990 – 1991, Apr 1962.

[20] O. Mishima, K. Era, J. Tanaka, and S. Yamaoka. Ultraviolet light-emitting diode of a cubic boron nitride *pn* junction made at high pressure. *Applied Physics Letters*, 53(11):962 – 964, Sep 1988.

[21] C. A. Spindt, I. Brodie, L. Humphrey, and E. R. Westerberg. Physical properties of thin-film field emission cathodes with molybdenum cones. *Journal of Applied Physics*, 47(12):5248 – 5263, Dec 1976.

[22] Q. H. Wang, M. Yan, and R. P. H. Chang. Flat panel display prototype using gated carbon nanotube field emitters. *Applied Physics Letters*, 78(9):1294 – 1296, Feb 2001.

[23] B. R. Chalamala, R. M. Wallace, and B. E. Gnade. Effect of o_2 on the electron emission characteristics of active molybdenum field emission cathode arrays. *Journal of Vacuum Science and Technology B*, 16(5):2859 – 2865, Sep 1998.

[24] D. Temple. Recent progress in field emitter array development for high performance applications. *Materials Science and Engineering: R: Reports*, 24(5):185 – 239, Jan 1999.

[25] M. C. Kelly. *The Earth's Ionosphere. Plasma Physics and electrodynamics.* Academic Press, 1989.

[26] D. Litvinov, C. A. Taylor II, and R. Clarke. Semiconducting cubic boron nitride. *Diamond and Related Materials*, 7:360, 1998.

[27] B. N. Chapman. *Glow Discharge Processes*. John Wiley & Sons, Inc., 1989.

[28] J. Asmussen. Electron cyclotron resonance microwave discharges for etching and thin film deposition. In S. M. Rossnagel, J. J. Cuomo, and W. D. Westwood, editors, *Handbook of Plasma Processing Technology: Fundamentals, Etching, Deposition, and Surface Interactions*, page 285. William Andrew Inc., 1990.

[29] S. Kidner, C. A. Taylor II, and R. Clarke. Low energy kinetic threshold in the growth of cubic boron nitride films. *Applied Physics Letters*, 64(14):1859, 1994.

[30] D. Litvinov. *Growth of Semiconducting Cubic Boron Nitride Thin Films*. PhD thesis, University of Michigan, Ann Arbor, 1999.

[31] T. Sato. Spectral emissivity of silicon. *Japanese Journal of Applied Physics*, 6(3):339, 1967.

[32] A. S. Arrott. Introduction to reflection high energy electron diffraction (RHEED). In J. A. C. Bland and B. Heinrich, editors, *Ultrathin Magnetic Structures I: An Introduction to the Electronic, Magnetic and Structural Properties*, page 177. Springer, 2005.

[33] C. A. Taylor II. *Growth and Optical Studies of Boron Nitride Films on Silicon Substrates*. PhD thesis, University of Michigan, Ann Arbor, 1996.

[34] W. Braun. *Applied RHEED: Reflection High-Energy Electron Diffraction During Crystal Growth*. Springer-Verlag, Berlin, 1999.

[35] P. B. Mirkarimi, K. F. McCarty, and D. L. Medlin. Review of advances in cubic boron nitride film synthesis. *Materials Science and Engineering: R: Reports*, 21:47–100, 1997.

[36] C. N. Banwell. *Fundamentals of molecular spectroscopy*. McGraw-Hill, New York, 1966.

[37] W. S. Lau. *Infrared characterization for microelectronics*. World Scientific, River Edge, N.J., 1999.

[38] R. Geick, C. H. Perry, and G. Rupprecht. Normal modes in hexagonal boron nitride. *Physical Review*, 146(2):543, Jun 1966.

[39] P. J. Gielisse, S. S. Mitra, J. N. Plendl, R. D. Griffis, L. C. Mansur, R. Marshall, and E. A. Pascoe. Lattice infrared spectra of boron nitride and boron monophosphide. *Physical Review*, 155(3):1039, Mar 1967.

[40] S. Fahy. Calculation of the strain-induced shifts in the infrared-absorption peaks of cubic boron nitride. *Physical Review B*, 51(18):12873, May 1995.

[41] D. V. Tsu, G. Lucovsky, M. J. Mantini, and S. S. Chao. Deposition of silicon oxynitrie thin films by remote plasma enhanced chemical vapor deposition. *Journal of Vacuum Science and Technology A*, 5(4):1998, July 1987.

[42] G. Binning, C. F. Quate, and Ch. Gerber. Atomic force microscope. *Physical Review Letters*, 56(9):930, 1986.

[43] R. Gomer. *Field Emission and field Ionization*. Harvard University Press, 1961.

[44] R. W. Wood. A new form of cathode discharge and the production of x-rays, together with some notes on diffraction. preliminary communication. *Physical Review (Series I)*, 5(1):1 – 10, Jul 1897.

[45] W. H. Schottky. Über kalte und warme elektronenentladungen. *Zeitschrift für Physik A Hadrons and Nuclei*, 14(1):63 – 106, Dec 1923.

[46] R. A. Millikan and Carl F. Eyring. Laws governing the pulling of electrons out of metals by intense electrical fields. *Physical Review*, 27(1):51 – 67, Jan 1926.

[47] R. A. Millikan and C. C. Lauritsen. Relations of field-currents to thermionic-currents. *Proceedings of the National Academy of Sciences of the United States of America*, 14(1):45 – 49, Jan 1928.

[48] R. H. Fowler and L. Nordheim. Electron emission in intense electric fields. *Proceedings of the Royal Society of London. Series A, Containing Papers of a Mathematical and Physical Character*, 119(781):173 – 181, 1928.

[49] L. W. Nordheim. The effect of the image force on the emission and reflexion of electrons by metals. *Proceedings of the Royal Society of London. Series A, Containing Papers of a Mathematical and Physical Character*, 121(788):626 – 639, 1928.

[50] E. L. Murphy and R. H. Good Jr. Thermionic emission, field emission, and the transition region. *Physical Review*, 102(6):1464, 1956.

[51] S. G. Christov. General theory of electron emission from metals. *Physica Status Solidi*, 17(11):11, 1966.

[52] J. W. Gadzuk and E. W. Plummer. Field emission energy distribution (FEED). *Reviews of Modern Physics*, 45(3):487, 1973.

[53] A. Modinos. *Field, Thermionic, and Secondary Electron Emission Spectroscopy*. Plenum Press, 1984.

[54] F. Charbonnier. Developing and using the field emitter as a high intensity electron source. *Applied Surface Science*, 94-95:26, 1996.

[55] R. G. Forbes and K. L. Jensen. New results in the theory of fowler-nordheim plots and the modelling of hemi-ellipsoidal emitters. *Ultramicroscopy*, 89:17, 2001.

[56] R. G. Forbes and J. H. B. Deane. Reformulation of the standard theory of fowler-nordheim tunnelling and cold field electron emission. *Proceedings of the Royal Society A: Mathematical, Physical, and Engineering Sciences*, 463(2087):2907 – 2927, 2007.

[57] K. L. Jensen. On the application of quantum transport theory to electron sources. *Ultramicroscopy*, 95:29 – 48, May – Jun 2003.

[58] K. L. Jensen. Electron emission theory and its application: Fowler-nordheim equation and beyond. *Journal of Vacuum Science and Technology B*, 21(4):1528 – 1544, Jul – Aug 2003.

[59] R. G. Forbes. Field emission: New theory for the derivation of emission area from a Fowler−Nordheim plot. *Journal of Vacuum Science and Technology B: Microelectronics and Nanometer Structures*, 17(2):526, 1999.

[60] E. R. Cohen and B. N. Taylor. The 1986 codata recommended values of the fundamental physical constants. *Journal of Research of the National Bureau of Standards*, 92(2):85 – 95, 1987.

[61] N. Morgulis. On electron field emission from semiconductor cathodes. *Zhurnal Tekhnicheskoi Fiziki (Russian)*, 17(1):983 – 986, 1947.

[62] R. Stratton. Field emission from semiconductors. *Proceedings of the Physical Society B*, 68(10):746, 1955.

[63] R. Stratton. Theory of field emission from semiconductors. *Physical Review*, 125(1):67, 1962.

[64] G. Fursey. *Field Emission in Vacuum Microelectronics*, chapter Field Emission from Semiconductors, pages 71 – 104. Kluwer Academic/Plenum Publishers, 2005.

[65] S. G. Christov. Unified theory of thermionic and field emission from semiconductors. *Physica Status Solidi (b)*, 21(1):159 – 173, 1967.

[66] H. G. Kosmahl. Analytical evaluation of field emission enhancement factors for ellipsoidal cones and elliptic cross-section wedges. *IEEE Transactions on Electron Devices*, 38(6):1534 – 1537, 1991.

[67] E. E. Martin, F. M. Charbonnier, W. W. Dolan, W. P. Dyke, H. W. Pitman, and J. K. Trolan. Research on field emission cathodes. Technical report 59-20, Wright Air Development Division, Jan 1960.

[68] W. Zhu, editor. *Vacuum Microelectronics*, chapter 3. John Wiley & Sons, Inc., 2001.

[69] K. L. Jensen. Exchange-correlation, dipole, and image charge potentials for electron sources: Temperature and field variation of the barrier height. *Journal of Applied Physics*, 85(5):2667 – 2680, Mar 1999.

[70] N. Ooi and J. B. Adams. Ab initio studies of the cubic boron nitride (110) surface. *Surface Science*, 574(2):269 – 286, Oct 2005.

[71] A. Sunger. A molecular calculation of electronic properties of layered crystals: I. truncated crystal approach for hexagonal boron nitride. *Journal of Physics C: Solid State Physics*, 7(1):76 – 95, 1974.

[72] C. Bandis and B. B. Pate. Photoelectric emission from negative-electron-affinity diamond (111) surfaces: Exciton breakup versus conduction-band emission. *Phys. Rev. B*, 52(16):12056–12071, Oct 1995.

[73] K. L. Jensen and C. M. Marrese-Reading. Emission statistics and the characterization of array current. *Journal of Vacuum Science and Technology B*, 21(1):412 – 417, Jan – Feb 2003.

[74] J. D. Zuber, K. L. Jensen, and T. E. Sullivan. An analytical solution for microtip field emission current and effective emission area. *Journal of Applied Physics*, 91(11):9379 – 9384, Jun 2002.

[75] K. L. Jensen. An analytical model of an emission-gated twystrode using a field emitter array. *Journal of Applied Physics*, 83(12):7982 – 7992, Jun 1998.

[76] W. D. Goodhue, P. M. Nitishin, C. T. Harris, C. O. Bozler, D. D. Rathman, G. D. Johnson, and M. A. Hollis. Bright-field analysis of field emission cones using high resolution transmission electron microscopy and the effect of structural properties on current stability. *Journal of Vacuum Science and Technology B*, 12(2):693 – 696, Mar 1994.

[77] V. T. Binh, S. T. Purcell, N. Garcia, and J. Doglioni. Field emission electron spectroscopy of single atom tips. *Physical Review Letters*, 69(17):2527 – 2530, Oct 1992.

[78] C. Py and R. Baptist. Stability of the emission of a microtip. *Journal of Vacuum Science and Technology B*, 12(2):685 – 688, Mar 1994.

[79] P. R. Schwoebel, C. A. Spindt, C. E. Holland, and J. A. Panitz. Field emission current cleaning and annealing of microfabricated cold cathodes. *Journal of Vacuum Science and Technology B*, 19(3):980 – 987, May 2001.

[80] C. Kleint. Surface diffusion model of adsorption-induced field emission flicker noise. *Surface Science*, 25(2):394 – 434, Apr 1971.